UNIVERSITÀ DI PARMA

Università degli Studi di Parma

Dottorato di ricerca in
Scienza e Tecnologia dei Materiali
Ciclo XXXIII

Correction of X- and γ-ray spectra acquired by CZT-based detectors

Coordinatore:
Chiar.mo Prof. Enrico Dalcanale
Tutore:
Chiar.mo Dott. Andrea Zappettini

Dottorando: Nicola Sarzi Amadè

Anni Accademici 2017/2018 – 2019/2020

To my family

The additive process is merely a cultivation of memory, which becomes mechanical.
Learning is never cumulative; it is a movement of knowing that has no beginning and no end.

Bruce lee, *Bruce Lee: Artist of Life*

Acknowledgements

First of all, I would like to thank Xnext s.r.l. for the financial support and, especially, for giving me the opportunity to get an insight into a real industrial context.

I would like to express my grateful thanks to my research group: my supervisor Andrea Zappettini, who has always shown great faith in me, and Manuele Bettelli, whose patience and versatility still impresses me.

A special thanks goes to my Ph.D. "buddies" Filippo Vurro and Antonino Buttacavoli. I am truly happy that I met such like-minded people with whom I shared experiences, thoughts and doubts during these years.

I would also like to thank Nicola Zambelli, Silvia Zanettini and Giacomo Benassi for their willingness and support. Surely, they had a major role in my educational path.

Thanks to the rest of the old "SIGNAL" group and to all the people of IMEM and other institutes who helped me in my research activity, the list is indeed long.

A special mention goes to my lunch companions (Bronz and Dedè especially) with whom I had the most interesting and stimulating debates on whatever topic of the human knowledge, I will really miss those moments.

Finally, thanks to my family and all the special people in my life for their wholehearted support.

Parma,
December 31, 2020

Nicola Sarzi Amadè

Contents

List of Tables

List of Figures

Chapter 1

Introduction

Room Temperature Semiconductor Detectors (RTSD) based on CdZnTe (hereinafter CZT) have been widely used in X- and γ-ray spectroscopy in the energy range 10^1–10^4 keV owing to their compactness, high energy resolution and high stopping power. These detectors do not require any cooling which enables their applicability in various fields such as medical imaging, environmental monitoring, astrophysics, decommissioning, nuclear power plants monitoring and homeland security. The related advancements in material science (crystal growth and processing, contact deposition) and technology (low-noise pre-amplifier, signal processing) are undoubtedly consolidated. Nonetheless, the measurements obtained with such devices are still affected by spectral distortions, which are mainly related to partial transfer of the photon energy, incomplete charge collection and excessive noise. Therefore, a straightforward interpretation of experimental data is not always possible. The development of powerful data analysis methods has always accompanied experimental science, and hence also this sector. Nowadays, the extensive knowledge of the physical mechanisms underlying the functioning of CZT-based RTSD can be combined with the tremendous progresses of the last decade in data science to push further the performances of these devices.

This thesis is focused on the development of algorithms and techniques to correct spectral distortions affecting CZT-based devices and to extract reliable information from measurements. The thesis is structured as follows.

The first part of the thesis regards the fundamentals of X- and γ-ray semiconductor detectors. More specifically, Chapter 2 is devoted to the description of the mechanisms of interaction of high energy photons with semiconductor materials and the related secondary effects. The aim is to explain the physical origin of the features present in measured spectra. The actual operation of RTSD and the signal generation process is described in Chapter 3. The role of the properties of the semiconductor materials are outlined as well as how CZT fits in this field of application.

The second part concerns the main results achieved during my Ph.D. at the IMEM-CNR. Chapter 4 describes a method to exploit the knowledge of the response function of a CZT-based RTSD to unfold γ-spectra. Spectral unfolding allows us to overcome

instrumental limits and to extract an accurate approximation of the true energy distribution of the incident radiation. This is particularly useful in devices with low or average energy resolution, characterised by broad and overlapped peaks. In Chapter 5 I present a novel algorithm based on convolutional neural networks to perform radioisotope recognition on raw γ-spectra. This method was conceived to be applied on spectra where the relevant features cannot be extracted with other approaches owing to limited performances of the detection system or poor statistics. In Chapter 6 I gathered the results deriving from the measurement session performed at Diamond Light Source Synchrotron (Didcot, UK) regarding the local response of pixelated detectors. Measurements at high photon fluxes were also performed, which I used to build a model to simulate flux-dependent distortions.

The results achieved in these three years are summarised in the last chapter, along with future perspectives on the role of algorithms in the field of X- and γ-ray spectroscopy.

Part I

Fundamentals of CZT-based X- and γ-ray detectors

Chapter 2

Interaction of radiation with matter

This chapter is devoted to the description of the mechanisms of interaction of X- and γ-radiation with matter. The detection of high energy photons in RTSDs is indeed possible through their partial or complete absorption within the semiconductor volume where the energy carried by the incoming photon is transferred to the crystal through multiple sequential collisions. The purpose is giving the reader the necessary elements to understand the origin of features which appear in actual measurements of radioactive sources.

In the first part, the principles of radioactive decays and radioactivity are briefly mentioned. Then, the types of interaction of high energy photons with the absorbing medium and the related secondary processes are described. For a fine and detailed explanation of the physics on this topics, the interested reader is referred to specific textbooks [1, 2, 3]

2.1 Radioactive decay

A radioactive process consists in a spontaneous transformation of an unstable atomic nucleus P (referred to as parent) to one or more nuclei D (referred to as daughters) with a different number of nucleons (mass number A) and/or protons (atomic number Z), depending on the disintegration mode. In the process, the nuclide releases energy in the form of radiation. The main decay modes are reported in Table 2.1.

Table 2.1: List of the main disintegration modes which lead to the emission of radiation. The "*" superscript denotes an excited state.

Mode	**Decay**	**Products**
α-decay	${}^{A}_{Z}\mathrm{P} \rightarrow [{}^{A-4}_{Z-2}\mathrm{D}]^{2-} + \alpha$	• α particle
β-decay:		
• β^--decay	${}^{A}_{Z}\mathrm{P} \rightarrow [{}_{Z+1}{}^{A}\mathrm{D}]^{+} + \beta^- + \bar{\nu}_e$	• electron • anti-neutrino
◦ β^+-decay	${}^{A}_{Z}\mathrm{P} \rightarrow [{}_{Z-1}{}^{A}\mathrm{D}]^{-} + \beta^+ + \nu_e$	◦ positron ◦ neutrino
Electron capture	${}^{A}_{Z}\mathrm{P} \rightarrow {}_{Z-1}{}^{A}\mathrm{D}^* + \nu_e$	• neutrino
Proton emission	${}^{A}_{Z}\mathrm{P} \rightarrow [{}^{A-1}_{Z-1}\mathrm{D}^*]^{-} + \mathrm{p}$	• proton
Spontaneous fission	$\mathrm{P} \rightarrow \mathrm{D}_1 + \mathrm{D}_2 + d_1 + d_2 + ...$	• fragment nuclei • nuclear particles
β delayed processes:		
• neutron emission (β^-n)	${}^{A}_{Z}\mathrm{P}^* \rightarrow {}^{A-1}_{Z}\mathrm{D} + \mathrm{n}$	• neutron
◦ proton emission (β^+p)	${}^{A}_{Z}\mathrm{P}^* \rightarrow {}^{A-1}_{Z-1}\mathrm{D} + \mathrm{p}$	◦ proton
◇ α emission ($\beta^-\alpha$)	${}^{A}_{Z}\mathrm{P}^* \rightarrow {}^{A-4}_{Z-2}\mathrm{D} + \alpha$	◇ α particle

The daughter nucleus can form in an excited nuclear state which relaxes through the emission of one or more γ-photons. This decay is defined as isomeric transition since the mass and atomic numbers remain unchanged (Figure 2.1):

$$[{}^{A}_{Z}\mathrm{D}]^* \rightarrow {}^{A}_{Z}\mathrm{D} + \gamma \tag{2.1}$$

Depending on the energy of the excited state, the atomic number and the multipolarity (i.e., the classification of the transition based on the total angular momenta of the initial and final states), the average lifetime may vary from $\sim 10^{-14}$ s to several years. Above 10^{-9} s, the nuclide is considered metastable (conventionally denoted by the superscript ${}^{\mathrm{m}}$). The energy of the γ-ray corresponds to the difference between the initial and final energy levels minus the recoil energy of the nucleus which is usually negligible:

$$E_\gamma = (E_i - E_f) - E_r = E^* - E_r \tag{2.2}$$

The de-excitation does not always lead to the emission of a γ-photon. Even if with a low probability ($\propto Z^3/E^*$), the energy may be transferred to an electron of the X-shell

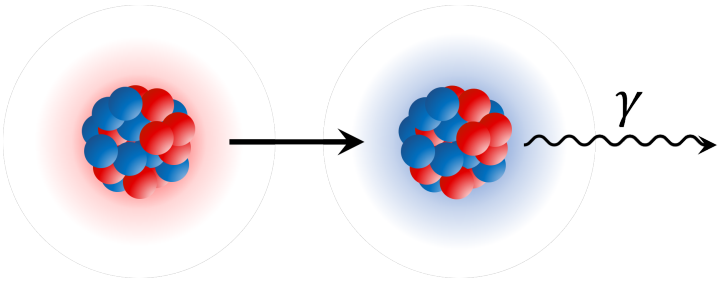

Figure 2.1: Schematic representation of an isomeric transition.

(where $X = K, L, M, \dots$) which is then ejected (internal conversion):

$$ {}^{\mathrm{A}}_{\mathrm{Z}}\mathrm{D} \rightarrow [{}^{\mathrm{A}}_{\mathrm{Z}}\mathrm{D}]^{*} + e^{-} \tag{2.3} $$

The conversion electron carries an energy defined as:

$$ E_{ce} = E_{\gamma} - E_{b} \quad \text{with} \quad E_{\gamma} > E_{b} \tag{2.4} $$

where E_b is the binding energy of the orbital electron. Internal conversion occurs mainly in the decay of low-lying excited states of heavy nuclei and with electrons of the inner shells since they have the highest probability of being within the nucleus (e.g., ^{241}Am). Another possible process, which gets significant at high energies, is the creation of an electron-positron pair (internal pair creation) whose kinetic energy T is

$$ T(e^{\pm}) = E_{\gamma} - 2m_{e}c^{2} \quad \text{with} \quad E_{\gamma} > 2m_{e}c^{2} \simeq 1022 \quad \text{keV} \tag{2.5} $$

where m_e is the electron rest mass and c is the speed of light in vacuum. The subsequent annihilation of the positron leads to a further emission of two 511 keV photons referred to as "annihilation radiation" (e.g., ^{22}Na, ^{40}K).

2.2 X- and γ-radiation

Since photons penetrating matter are absorbed or scattered in a single event, if we consider a collimated beam of γ-rays that incides on a detector, the removed number of photon (ΔN) is proportional to the thickness of the traversed absorbing medium (Δx) and to the number of incident photons (N):

$$\Delta N = -\mu N \Delta x \quad \longrightarrow \quad N(x) = N_0 e^{-\mu x} \tag{2.6}$$

The integration leads to an exponential behaviour where the proportionality constant μ represents the linear attenuation coefficient expressed as cm^{-1}. The mechanisms of interaction in the energy region of interest of RTSD, which spans from few keV up to few MeV, are basically three[*]: photoelectric absorption, Compton scattering and pair production (see Table 2.2).

Table 2.2: List of the predominant interaction mechanisms of γ-rays in matter in the energy range 10^1–10^4 keV.

Process	**Interaction with**	**Effects**	**Products**
Photoelectric	Atomic electrons	Complete absorption	• Photoelectron • Ionized atom
Compton	Atomic electrons	Incoherent scattering	• Deflected photon • Ejected electron • Ionized atom
Rayleigh	Atomic electrons	Coherent scattering	• Deflected photon
Pair production	Coulomb field of charged particles	Complete absorption	• Electron • Positron

For completeness, Rayleigh scattering is also reported, although this process is significant only at low energy in case of heavy elements but it can be neglected in the evaluation of μ since the average deflection angle is small. Since these mechanisms are independent, μ consists in the sum of the attenuation coefficients for each process:

$$\mu = (\tau + \sigma + \kappa)N \quad \mathrm{cm}^{-1} \tag{2.7}$$

where τ, σ and κ are the cross sections for the photoelectric, Compton and pair production effects in cm^2/atom, respectively, $N = \rho_m N_A / M$ is the atom density per cm^3, N_A is the Avogadro constant in atom/mol, M is the molar mass in g/mol and ρ_m is the mass density in $\mathrm{g/cm}^3$. The mass attenuation coefficient, defined as μ/ρ_m, is also largely used since it is independent from the material density and physical state. In the following sections, I will describe the physical concepts which are necessary for the evaluation of τ, σ and κ.

[*]For a complete list the interested reader is referred to [1], Ch. 23, pg. 672

2.2.1 Photoelectric absorption

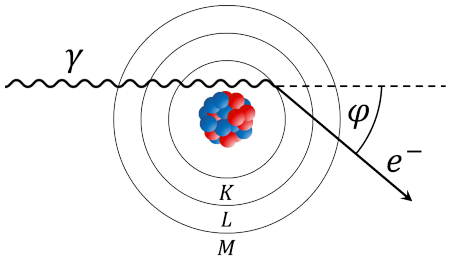

Figure 2.2: Schematic representation of the photoelectric process. The incident photon is completely absorbed and a photoelectron is ejected with an angle φ in respect to the photon direction.

Photoelectric effect occurs only with atomic (i.e., bound) electrons because a third particle is necessary to conserve momentum and the interaction may occur with electrons of any atomic shells. However, the photoelectron is most probably ejected from the K- and L-shells (provided that the photon exceeds the binding energy) since the probability increases rapidly with E_b. The energy of the photoelectron is given by

$$T = E_\gamma - E_b \quad \text{with} \quad E_\gamma > E_b \tag{2.8}$$

Depending on E_γ and E_b, the photoelectric cross section assumes different analytic expressions. If $E_\gamma \gg E_b$, the Born approximation holds and the absorption coefficient for the K-shell of an atom with Z electrons can be calculated using non-relativistic quantum mechanics and hydrogen-like wave functions for the atomic electrons:

$$\tau_K = \phi_0 Z^5 \alpha^4 2^{\frac{5}{2}} \left(\frac{m_e c^2}{E_\gamma}\right)^{\frac{7}{2}} \quad \text{cm}^2/\text{atom} \tag{2.9}$$

where $\phi_0 = 8\pi r_0^2/3$ is the cross section for Thomson scattering, $r_0 = \hbar\alpha/m_e c$ is the classical electron radius, $\alpha = e^2/4\pi\epsilon_0\hbar c$ is the fine-structure constant, $\hbar$ is the reduced Planck constant and ϵ_0 is the vacuum permittivity. If $E_\gamma \approx E_b$, τ_K can still be calculated under the dipole transition approximation:

$$\tau_K = \phi_0 \frac{(Z-0.3)^8}{Z^2} \alpha^5 2^3 \pi \left(\frac{m_e c^2}{E_\gamma}\right)^4 \frac{\exp(-4\xi \cot^{-1}\xi)}{1-\exp(-2\pi\xi)} \quad \text{cm}^2/\text{atom} \tag{2.10}$$

where in the numerator Z is reduced by the $1s$ screening constant which is equal for all Z and $\xi = (E_b/T)^{\frac{1}{2}}$. The absorption coefficient for the outer shells can be calculated using the same assumptions and in these cases the dependence from the Z and E_γ is different. The total cross section τ is obtained by adding the contribution of each shell ($\tau_{L,M,\ldots}$). Based on experimental data, at high energies τ is usually obtained by multiplying τ_K by a constant:

$$\tau = \tau_K + \tau_L + \tau_M \simeq \frac{5}{4}\tau_K \tag{2.11}$$

On the other hand, at low energies the cross section is discontinuous (absorption edges) in correspondence of the electronic transitions when $E_\gamma = E_X$ where E_X is the electron binding energy and $X = K, L, M, \ldots$. Empirically, τ is roughly approximated to

$$\tau \simeq constant \cdot \frac{Z^{n_1}}{E_\gamma^{n_2}} \quad \text{where} \quad \begin{cases} 4 < n_1 < 5 \\ n_2 \sim 7/2 \end{cases} \tag{2.12}$$

where both exponents n_1 and n_2 depend on E_γ. Overall, it is evident that high Z materials are preferred to enhance photoelectric absorption.

The photoelectric absorption is always accompanied by the electron rearrangement of the ionized atom (Section 2.3) and the ejection of a photoelectron (Section 2.4).

2.2.2 Compton scattering

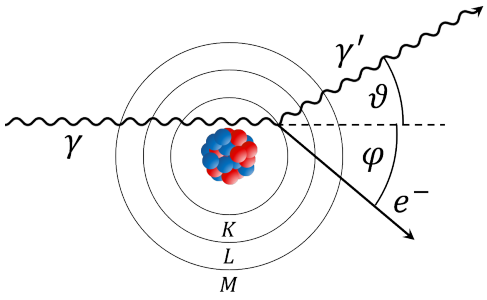

Figure 2.3: Schematic representation of Compton effect in the scattering plane. The incident photon is deflected with an angle ϑ whereas the electron is ejected with an angle φ in respect to the photon direction.

The theory of the scattering of γ-rays by electrons can be derived by solving the equations expressing the conservation of energy and momentum. Usually, the struck electron can be considered to be unbound since $E_\gamma \gg E_b$. Moreover, the relativistic expression for mass and energy must be adopted because E_γ is not negligible in respect to $m_e c^2$ (it is useful to introduce the adimensional parameter $\zeta = E_\gamma / m_e c^2$ in the following formulas). Thus, by equating the energies and momenta before and after the collision between the incoming photon and the electron at rest we obtain

$$\begin{cases} E_\gamma = E'_\gamma + T = E'_\gamma + m_e c^2 \left[\left(1 - \beta^2\right)^{-\frac{1}{2}} - 1 \right] \\ \dfrac{E_\gamma}{c} = m_e c \beta \left(1 - \beta^2\right)^{-\frac{1}{2}} \cos\varphi + \dfrac{E'_\gamma}{c} \cos\vartheta \\ 0 = m_e c \beta \left(1 - \beta^2\right)^{-\frac{1}{2}} \sin\varphi - \dfrac{E'_\gamma}{c} \sin\vartheta \end{cases} \tag{2.13}$$

where $\beta = v/c$ is the electron velocity expressed in units of the speed of light, T is the kinetic energy of the struck electron, E'_γ is the energy of the scattered photon and ϑ and φ represent the angles of the scattered photon and the recoil electron, respectively, as shown in Figure 2.3. E'_γ and T are the quantities of interest since they have a fundamental role in defining the measured spectral shape, as explained in Chapter 4.2. They can be obtained by solving the system of conservation equations (Equation 2.13):

$$E'_\gamma = \frac{E_\gamma}{1+\zeta(1-\cos\vartheta)} \qquad T = E_\gamma - E'_\gamma = E_\gamma\left[1 - \frac{1}{1+\zeta(1-\cos\vartheta)}\right] \tag{2.14}$$

The differential scattering cross section per electron, also called Klein-Nishina formula, can be obtained by solving the Dirac equation for the electron which, for unpolarized incident radiation, gives:

$$\begin{aligned} \frac{d\sigma}{d\Omega} &= \frac{r_0^2}{2}\left(\frac{E'_\gamma}{E_\gamma}\right)^2\left(\frac{E_\gamma}{E'_\gamma} + \frac{E'_\gamma}{E_\gamma} - \sin^2\vartheta\right) = \\ &= \frac{r_0^2}{2}\left\{\frac{1}{\left[1+\zeta(1-\cos\vartheta)\right]^2}\left[1+\cos^2\vartheta + \frac{\zeta^2(1-\cos\vartheta)^2}{1+\zeta(1-\cos\vartheta)}\right]\right\} \end{aligned} \tag{2.15}$$

Equation 2.15 reduces to the classical Thomson cross section at low energies (i.e., $\zeta \ll 1$). The angular dependence of $d\sigma/d\Omega$ at different energies is reported in Figure 2.4: by increasing E_γ, the photon is mainly deflected along the primary direction.

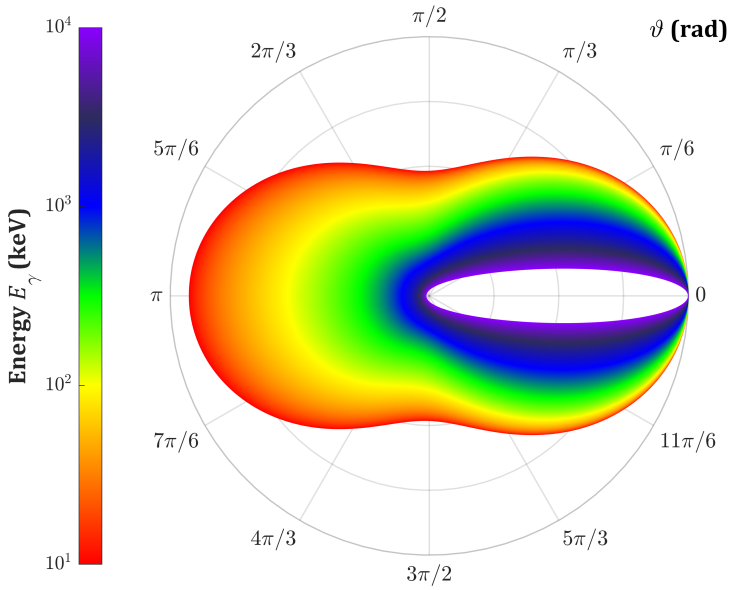

Figure 2.4: Differential scattering cross section per electron as a function of the scattering angle ϑ at different energies (Equation 2.15).

By integrating Equation 2.15 over the solid angle and by multiplying for the number of electrons in an atom, we finally obtain the total Compton cross section:

$$\sigma = 2\pi r_0^2 Z \left\{ \frac{1+\zeta}{\zeta^2} \left[\frac{2(1+\zeta)}{1+2\zeta} - \frac{1}{\zeta} \ln(1+2\zeta) \right] + \right. \\ \left. + \frac{1}{2\zeta} \ln(1+2\zeta) - \frac{1+3\zeta}{(1+2\zeta)} \right\} \quad \text{cm}^2/\text{atom} \tag{2.16}$$

At low energies ($E_\gamma \approx E_b$) strong approximations must be adopted to describe the motions, distributions and binding energies of atomic electrons. Consequently, theoretical calculations do not yield accurate values of σ for all Z and T.

Analogously to photoelectric effect, an ionized atom and an ejected electron result from Compton scattering but, in addition, the incoming photon is deflected with a lower energy. As already mentioned, we are interested in the recoil energy of the electron because, if the deflected photon escapes from the crystal volume, it represents the only energy actually deposited in the RTSD, forming the so-called Compton edge. Hence, it is useful defining the differential cross section for giving an electron a recoil energy in the interval between T and $T + dT$ (Figure 2.5):

$$\frac{d\sigma}{dT} = \frac{2\pi m_e c^2}{E_\gamma'^2} \frac{d\sigma}{d\Omega} = \\ = \frac{\pi r_0^2 m_e c^2}{(E_\gamma - T)^2} \left\{ \left(\frac{m_e c^2 T}{E_\gamma^2} \right)^2 + 2 \left(\frac{E_\gamma - T}{E_\gamma} \right)^2 + \frac{T(E_\gamma - T)}{E_\gamma^3} \left(T - 2 m_e c^2 \right) \right\} \tag{2.17}$$

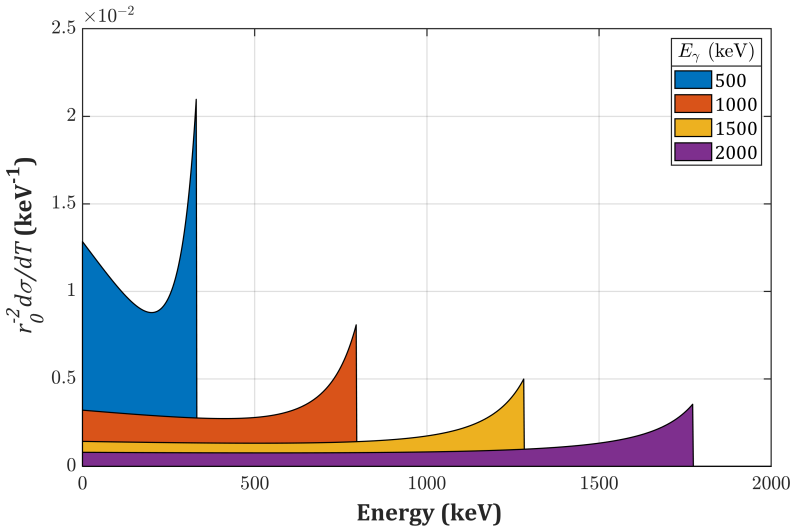

Figure 2.5: Differential scattering cross section per electron recoil at different energies (Equation 2.17).

2.2.3 Pair production

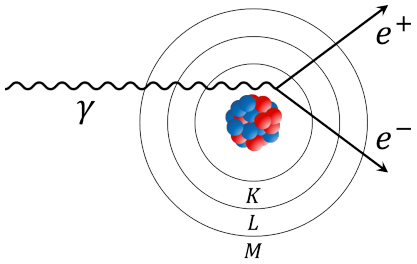

Figure 2.6: Schematic representation of the pair production process. The incident photon is completely absorbed and a positron-electron pair is created.

Pair production process consists in the complete absorption of a photon which is replaced by an electron-positron pair whose total energy is equal to the γ-ray energy. This interaction occurs only in the Coulomb field of charged particles and if E_γ is above a certain threshold. In the region of interest of RTSDs, this process takes place mainly in the nuclear field when E_γ exceeds twice the rest-mass energy of an electron.

$$E_\gamma = T_- + T_+ + 2m_e c^2 \quad \text{with} \quad E_\gamma \geq 2m_e c^2 = 1.022 \text{ MeV} \tag{2.18}$$

The solution to this physical problem can be obtained assuming a negligible interaction between the electron/positron and the nucleus, that is when $Z\alpha/\beta \ll 1$ for both particles (Born approximation). As a consequence, the energy distribution of electrons and positrons are symmetric since they are not subjected to the Coulomb repulsion and attraction. Moreover, for $E_\gamma \lesssim 20$ MeV, the process is more likely to occur at a distance from the nucleus that is smaller than the radius of K-shell, thus the screening due to atomic electrons can be neglected. The differential cross section for the creation of a positron of kinetic energy between T_+ and $T_+ + dT_+$ in the field of a nucleus of charge Ze is found to be

$$\frac{d\kappa}{dT_+} = \frac{\alpha r_o^2 Z^2 P(E_\gamma, Z)}{E_\gamma - 2m_e c^2} \tag{2.19}$$

where P is a complicated function which varies between 0 (for $E_\gamma \leq 2m_e c^2$) and ≈ 20 (for $E_\gamma = \infty$). The analytical integration of P is possible only in the extremely relativistic case. More generally, we can write

$$\kappa = \alpha r_0^2 Z^2 \int_0^1 P d\frac{T_+}{E_\gamma - 2m_e c^2} = \alpha r_0^2 Z^2 \bar{P} \quad \text{cm}^2/\text{nucleus} \tag{2.20}$$

where $\bar{P}$ increases approximately logarithmically with E_γ. For low energy (slightly above the $2m_e c^2$ threshold), Eq. 2.20 underestimates the cross section, especially for high Z elements, because the Born approximation does not hold. In this case, κ has a stronger dependence than Z^2. In summary, pair production is predominant in heavy elements and at high photon energy ($E_\gamma \sim$ several MeV).

2.2.4 Total attenuation coefficient

The overall trend of μ and the relative importance of τ, σ and κ are reported in Figure 2.7a in the case of CZT (XCOM: Photon Cross Sections Database). In general, photoelectric predominates at low energies whereas pair production predominates at high energies. Compton scattering prevails in the intermediate region whose extent decreases with increasing Z. The total attenuation coefficient ultimately determines the efficiency of the detector and the crystal thickness must be selected according to the energy range of interest for the application (Figure 2.7b). However, μ is only related to the probability that a photon interacts with a material of a given composition, density and thickness. As shown in Table 2.2, these processes always produce particles (photoelectrons, electron-positron pairs) and/or electromagnetic radiations (deflected photons, annihilation radiation) which in turn may, or may not, interact with the crystal. Furthermore, the relaxation of the medium (i.e., the de-excitation of ionized atoms) leads to the emission of additional radiation and fast electrons (fluorescence photons, Auger electrons). Therefore, the energy actually deposited in the RTSD depends on all the succeeding collisions and events which accompany the primary interactions which will be explained in the next sections.

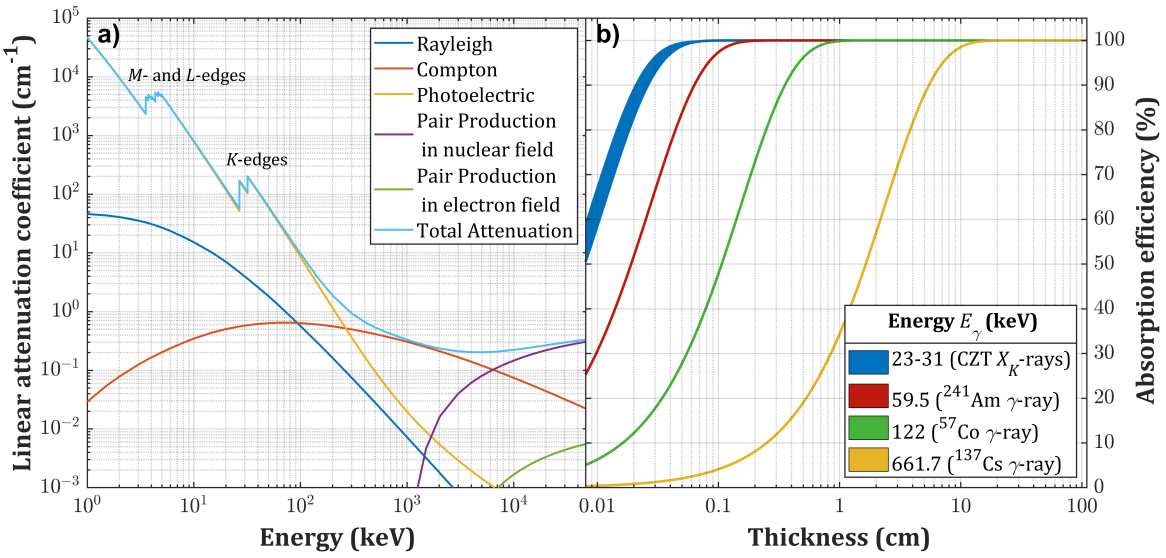

Figure 2.7: a) Photon absorption cross sections for CZT for all interaction mechanisms in the 10^0–5×10^4 keV energy range. **b)** Absorption efficiency of CZT as a function of crystal thickness at various photon energies (corresponding to the Cd and Te K-fluorescences and the characteristic γ-rays of the most commonly used radionuclides).

2.3 Electron rearrangement

Atoms ionized by γ-radiation present vacancies in the inner shells (usually in the K-shell) which are quickly refilled by electrons from less bound shells. Consequently, new vacancies are created and are progressively transferred in the most outer shells by a cascade process. This relaxation results either in the emission of fluorescence photons or in the ejection of Auger electrons.

2.3.1 Fluorescence

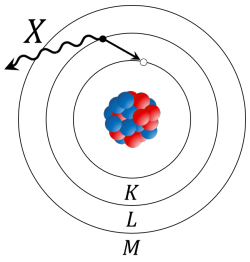

Figure 2.8: Schematic representation of fluorescence.

Fluorescence occurs between specific energy levels according to the selection rules

$$\begin{aligned} \Delta l &= \pm 1 \\ \Delta j &= 0, \pm 1 \end{aligned} \tag{2.21}$$

where l and j are the orbital and total angular momentum quantum numbers, respectively. The energy of the fluorescence photon is equal to the difference of the binding energies of the involved energy levels

$$E_{X_K} = E_K - E_X \quad \text{where} \quad X = L, M, N, O, \ldots \tag{2.22}$$

and the emitted X_K-ray is labelled consequently:

$$K\alpha \begin{cases} K\alpha_2 & K\text{-}L_2 \\ K\alpha_1 & K\text{-}L_3 \end{cases} \quad K'\beta_1 \begin{cases} K\beta_3 & K\text{-}M_2 \\ K\beta_1 & K\text{-}M_3 \\ K\beta_5'' & K\text{-}M_4 \\ K\beta_5' & K\text{-}M_5 \end{cases} \quad K'\beta_2 \ldots \tag{2.23}$$

The occurrence probability of this process, referred to as fluorescence yield ω_X where $X = K, L, M, \ldots$, is related to the dipole interaction between the electron that fills the vacancy and the vacancy itself ($\propto Z^4$). The typical energies of the emitted X_K-rays are of the order of tens of keV for high Z elements. Thus, the attenuation length for this kind of radiation may not be negligible compared to the dimensions of the crystal or of the electrodes. As reported in Figure 2.7a, few hundreds of μm are required to

completely stop the $K\alpha_1$, $K\alpha_2$ and $K\beta_1$ emissions of CZT. If the primary interaction occurs in the proximity of the crystal surfaces and the secondary X-radiation is not re-absorbed, the total energy deposited is equal to the initial energy of the primary γ-ray minus the characteristic energies of the X-ray. Analogously, when fluorescence photons interact far from the primary interaction in devices with more than one read-out electrode, the deposited energy can be collected by different electrodes of which one measures the characteristic energy of the X_K-ray and the other the remaining energy. The distortions produced by these effects will be explained in Chapter 3.

2.3.2 Auger effect

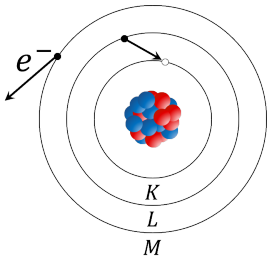

Figure 2.9: Schematic representation of the Auger effect.

This non-radiative process consists in a redistribution of the atomic electrons where the available energy is transferred to another less bound electron which is then ejected:

$$E_{AK} = E_K - E_X - E_Y - \Delta E \quad (E_Y \leq E_X) \tag{2.24}$$

where E_Y is the binding energy of the second electron. The corrective term ΔE is necessary since the binding energies for an excited atom are greater. Also in this case, the labeling depends on the shells (or subshells) of the two electrons involved:

$$KLL \begin{cases} KL_1L_1 \\ KL_1L_2 \\ KL_1L_3 \\ KL_2L_2 \\ KL_2L_3 \\ KL_3L_3 \end{cases} \quad KLX\ (X = M, N, ...) \begin{cases} KL_1M_1 \\ KL_1M_2 \\ KL_1M_3 \\ KL_1M_{4,5} \\ KL_2M_1 \\ ... \end{cases} \quad KXY... \tag{2.25}$$

The same analysis applies for vacancies in the L-shell. Unlike X-ray, the ejected electron quickly slows down in the material, as described in Section 2.4.

The occurrence probability of Auger effect (Auger yield $a_X = 1 - \omega_X$ where $X = K, L, M, \dots$) depends on the overlap of the shells (Coulomb interaction). As shown in Figure 2.10, fluorescence is the preferential relaxation process in the case of CZT for $X = K$ whereas it is negligible for less bound electrons [4, 5].

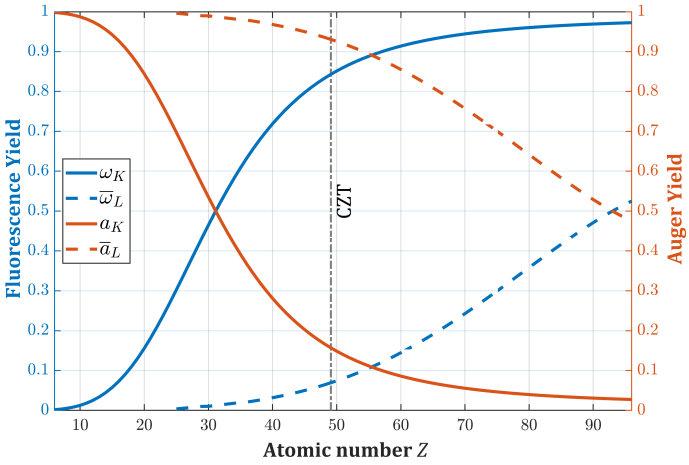

Figure 2.10: K-shell and average L-shell fluorescence and Auger yields as a function of the atomic number. The dashed vertical line represents the average atomic number of CZT.

2.4 Fast electrons

The term "fast electrons" (10^1–10^4 keV) is usually referred to β-radiation which results from the transformation of a nucleus proton to a neutron or vice versa. Nevertheless, the purpose of this section is not related to the detection of β particles. Actually, all the interaction mechanisms described in Section 2.2 result in the generation of secondary fast electrons into the semiconductor volume (also called δ-rays). In contrast to photons, charged particles lose energy gradually through multiple ionizing and radiative collisions with a large number of atoms which finally results in a cloud of free carriers in the conduction and valence bands of the semiconductor. The predominant interaction mechanisms in the 10^1-10^4 keV energy range will be described in this section and are summarized in Table 2.3. Positrons follow nearly the same energy loss processes as electrons with the difference that they eventually bind to electrons forming positronium. This hydrogen-like atom undergoes successive radiative transitions until it reaches the ground state with zero orbital angular momentum and finally annihilates, emitting two photons of energy $m_e c^2$ isotropically with respect to the primary direction. If one or both of these photons escape from the semiconductor volume, the measured energy is inferior giving rise to the annihilation peaks, analogously to the escape peaks.

Table 2.3: List of the predominant interaction mechanisms of fast electrons in matter in the energy range 10^1–10^4 keV.

Process	**Interaction with**	**Effects**	**Products**
Elastic scattering	Atomic nuclei	Coherent scattering	• Deflected electron
Inelastic scattering	Atomic electrons	Incoherent scattering	• Deflected electron • Ionized atom
Bremsstrahlung	Atomic nuclei	Incoherent scattering	• Deflected electron • Braking radiation

2.4.1 Elastic scattering

The only effect of coherent scattering is the deflection of the incoming electron by the Coulomb field of an atomic nucleus. The differential cross section for nuclear scattering without shielding (negligible for $T \lesssim 15$ MeV) can be calculated by applying the relativistic Dirac theory using the Born approximation:

$$\frac{d\sigma}{d\Omega} = \frac{Z^2 r_0^2}{4\sin^4(\theta/2)} \left(\frac{1-\beta^2}{\beta^4}\right) R(\beta, Z, \theta) = \left(\frac{d\sigma}{d\Omega}\right)_{Ruth} R(\beta, Z, \theta) \tag{2.26}$$

where $(d\sigma/d\Omega)_{Ruth}$ is the relativistic scattering law of Rutherford and the factor R is a quantum-mechanical correction related to the spin-orbit interaction. R cannot be expressed in analytic form but can be expanded in powers of $Z\alpha$ and approximated to

$$R(\beta, Z, \theta) \simeq 1 - \beta^2 \sin^2 \frac{\theta}{2} + \pi\beta Z\alpha \left(1 - \sin \frac{\theta}{2}\right) \sin \frac{\theta}{2} \tag{2.27}$$

The cross section for positrons can be obtained by substituting Z with $-Z$ in Equation 2.27 and is always smaller. Equation 2.26 does not consider the probability that the deflected electron radiates because of the Born approximation. This effect is known as Bremsstrahlung and is of the order of α in respect to elastic collisions (see Section 2.4.3).

2.4.2 Inelastic scattering

The energy loss is almost entirely due to interactions with atomic electrons resulting in the excitation and ionization of the atoms. Since the former process is more probable than the latter even for high energy electrons, the energy transferred per collision is usually small (the average kinetic energy of secondary electrons is generally of few eV). Therefore, it is evident that a large number of interactions is required to stop a fast electron. Contrary to γ-rays, it is only possible to define the most probable energy loss. The theory developed by Bohr, Bethe and Block defines the mean energy loss per cm path due to collisions:

$$\begin{aligned} -\left(\frac{\overline{dE}}{dx}\right)_c = & \frac{4\pi e^4 NZ}{m_0 c^2 \beta^2} \left[\ln\left(\frac{m_0 c^2 \beta^2 T}{2I^2(1-\beta^2)}\right) - \ln 2 \left(2\sqrt{1-\beta^2} - 1 + \beta^2\right) + \right. \\ & \left. + 1 - \beta^2 + \frac{1}{8}\left(1 - \sqrt{1-\beta^2}\right)^2 - \Delta_{pol}\right] \end{aligned} \tag{2.28}$$

where I is the mean excitation energy of the atomic electrons which depends from Z. Δ_{pol} is a corrective term, negligible in low density materials, which considers the polarizability by the Coulomb field of the incident electron. Since nuclear scattering (i.e., coherent scattering) predominates in high Z material, the true electron path length differs from the traversed material thickness. The cumulative effect of small deflections (due to both elastic and inelastic collisions) leads to large curvature in respect to the primary track and to tortuous paths whose total length divided by maximum distance reached in the initial direction is proportional to Z.

2.4.3 Bremsstrahlung

The theory of Bremsstrahlung (literally, "braking radiation") is formally equivalent to the pair production effect (Section 2.2) in which, on the contrary, the photon is absorbed rather than emitted. It consists in the deflection of the electron by the Coulomb field of nuclei which results in the emission of a photon. Instead of a quantum of light with a well defined energy, here the electron can radiate any amount of energy up to its total kinetic energy T, hence resulting in continuous X-ray spectra. The mean energy loss per cm path is given by

$$-\left(\frac{\overline{dE}}{dx}\right)_B = Nr_0^2 Z^2 \alpha (T + m_e c^2) \left[4 \ln \frac{2(T + m_e c^2)}{m_e c^2} - \frac{4}{3}\right] \tag{2.29}$$

The approximate ratio between ionization/excitation and radiative energy losses (Equations 2.28 and 2.29, respectively) shows that Bremsstrahlung is significant only in heavy elements at high energy:

$$\frac{(\overline{dE}/dx)_B}{(\overline{dE}/dx)_c} \simeq \frac{ZT}{1400 m_e c^2} \tag{2.30}$$

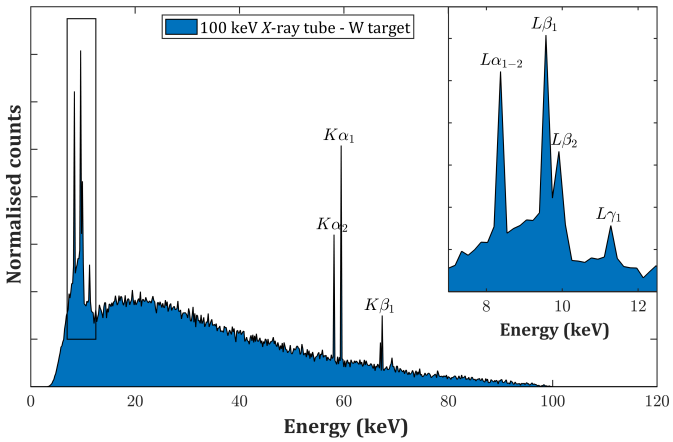

Figure 2.11: Simulated spectrum (GEANT4) of a X-ray tube for an accelerating voltage of 100 keV and a tungsten target. The peaks represent the characteristic K- and L-fluorescence lines of the metal target. Inset: zoomed portion of the L-fluorescence lines.

This physical process underlies the operation of X-ray tubes where electrons are accelerated in vacuum by an electric field and subsequently collide with a metal target. The X-rays resulting from both Bremmsstrahlung and the relaxation of ionized atoms of the target (Section 2.3) constitute the spectrum emitted by the tube. Different energy distributions can be obtained by varying the accelerating voltage, the target and the filters (an example is reported in Figure 2.11).

2.4.4 Free carrier generation in a semiconductor

The mean free path of fast electrons in matter is small compared to the typical crystal dimensions of RTSDs, hence the total kinetic energy is eventually released within the crystal volume. Impact ionizations and excitations induce transitions from the valence band to the conduction band and create a non-equilibrium distribution of "hot" carriers. This process is coupled to the emission of optical phonons and the residual kinetic energy of the created pair is converted into lattice vibrations through thermalization

losses. This leads to an average electron-hole pair creation energy ($E_{e\text{-}h}$) which is larger than the semiconductor energy gap (E_G) and is given by the semi-empirical law [6, 7]

$$E_{e\text{-}h} = E_G + \langle E_R \rangle + \langle E_K \rangle \simeq \frac{14}{5} E_G + r(\hbar\omega_R) \tag{2.31}$$

$\langle E_R \rangle$ is assumed to be proportional to the average number of emitted Raman quanta ($\hbar\omega_R$) per generated pair and falls in the $0.55 < r(\hbar\omega_R) < 1$ eV energy range. $\langle E_K \rangle$ represents the thermalization losses and, in the case of a simple two band configuration in direct band gap materials with equal electron and hole effective masses, is equal to $9/5E_G$. The number of photogenerated electron-hole pairs can be finally calculated as

$$N_{e\text{-}h} = \frac{E_\gamma}{E_{e\text{-}h}} \tag{2.32}$$

Estimating the initial shape and dimension of the charge cloud as a function of E_γ in a given material is arduous, both theoretically and experimentally, because of all the branching processes involved in the absorption of the primary radiation. Nevertheless, this can be achieved by Monte Carlo simulations where it is possible to track all the secondary particles and the energy released in each point of the crystal (Figure 2.12) [8]. The charge density per unit volume can be roughly approximated to an isotropic 3D-gaussian:

$$\rho_{ch} = \frac{Q_0}{\sigma_0^3 (2\pi)^{3/2}} \exp\left(-\frac{||\vec{x} - \vec{x}_b||^2}{2\sigma_0^2} \right) \tag{2.33}$$

where $Q_0 = eN_{e\text{-}h}$, $\vec{x}_b$ is the barycentre of the charge cloud and σ_0 is the initial variance.

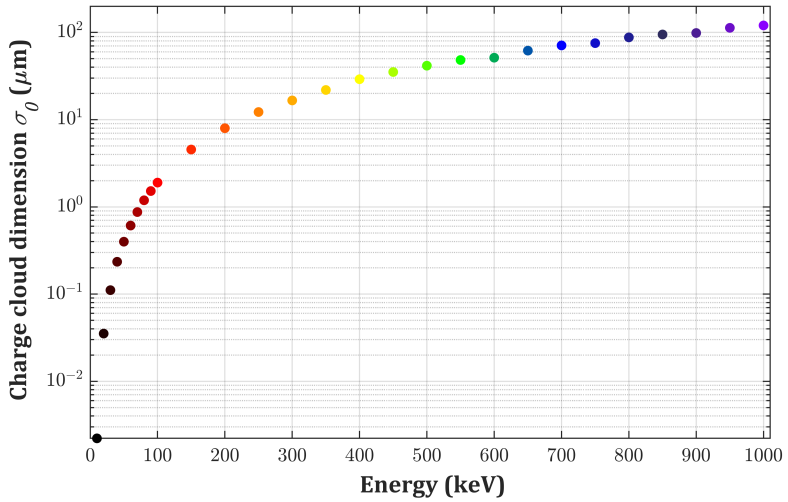

Figure 2.12: Energy dependence of the initial dimension of the charge cloud as a function of E_γ in the 10^1-10^3 keV energy range obtained with Geant4 calculations.

Chapter 3

Spectroscopic room temperature semiconductor detectors

Since their introduction in the 1960's, semiconductors detectors have represented a breakthrough in nuclear spectroscopy. The efficient and direct conversion of ionizing radiation to electric signal allowed us to realize sensitive and compact devices with incomparable performances in respect to previous technologies. Initially, group IV elements (silicon and germanium) were the only materials used for this purpose but the operability at cryogenic temperatures represented a strong limit which prevented their diffusion in fields where costs and convenience were of concern.

In the early 1970's, wide band gap semiconductor compounds (CdTe and HgI_2) started appearing in this context since they required minimal or no cooling. Nevertheless, at the time the actual crystals properties were different from the promising ones predicted by theory. Only after two decades of overall improvements the major problems related to crystal growth, surface processing and contact deposition were partially solved, thus opening the possibility of large-scale production shortly after [9].

Nowadays, CdTe and CZT dominate the panorama of RTSD owing to their portability, high energy resolution (every year closer and closer to Si-based systems), large atomic number and high density [10, 11]. In this chapter, I will briefly describe the mechanisms underlying the functioning of semiconductor radiation detectors and which role CZT has in this context.

3.1 Working principles

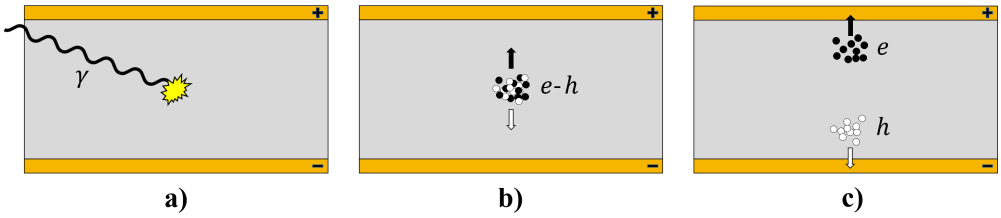

Figure 3.1: Schematic representation of the signal generation in a semiconductor-based radiation detector: **a)** interaction of the γ-ray with the crystal; **b)** electron-hole pairs production; **c)** Charge drifting and collection.

Single-photon counting semiconductor detectors act as solid state ionization chambers where the absorbed radiation produces a cloud of negative (electrons) and positive (holes) free charges according to the interaction mechanisms described in Chapter 2 (Figure 3.1a). The biased metal contacts deposited on the surfaces of the crystal generate an electric field within its volume which separates and drift the carriers (Figure 3.1b). The motion and the eventual collection of these charges induce a transient current on the read-out electrode which is then amplified and analyzed by proper electronics (Figure 3.1c). This technology present several strengths:

- Extremely compact and portable devices can be realized thanks to the higher stopping power in respect to gaseous or liquid detectors.
- The electric properties of the semiconductor can be finely tuned and optimized to obtain the desired attributes.
- The energy deposited by the photon is directly converted into electric charge, providing higher signals in respect to indirect conversion processes like scintillators.
- Spectroscopic information can be obtained by processing the signal produced by each photon, in contrast to devices which integrate the photogenerated current over all the exposure time.
- The contribution of dark current (i.e., the current which flows in the device in absence of radiation) can be neglected by setting a proper threshold and only the signals which exceed it are processed, thus providing a higher signal-to-noise ratio in respect to device which operates in integrating mode.
- Locating the interaction position is possible with a proper electrode patterning (e.g., pixelated detectors for X-ray imaging, 3D drift strips spectrometers).

3.1.1 Charge transport and collection

The photogenerated electrons and holes drift towards the anode and the cathode, respectively, with a velocity given by

$$\vec{v} = \mu\vec{E} \quad \text{with} \quad \mu = \frac{e}{m^*}\bar{\tau} \quad \text{and} \quad \frac{1}{m^*} = \frac{1}{\hbar^2}\frac{\partial^2 E}{\partial k^2} \tag{3.1}$$

where μ is the carrier mobility, $\bar{\tau}$ is the average scattering time with the lattice, impurities or defects and m^* is the effective mass which is given by the curvature of the electronic band in k-space. The linear relation between velocity and electric field holds below saturation which occurs at fields higher than the typical ones used in actual devices (≈ 15000 V·cm^{-1} at room temperature (RT) for CdTe [12]); hence, the mobility is assumed to be constant. The electric field within the crystal volume depends from several factors such as applied bias voltage, geometrical configuration of the electrodes, crystal dimensions, presence of spatial charge and defects and, finally, the metal contacts. Theoretically, calculating the field profile in each point of the crystal is arduous and usually experimental techniques are employed (Pockel effect, Laser Induced Transient Current Technique). In the case of isotropic band dispersion, the trajectory of a point charge can be simply calculated as

$$\vec{x}(t) = \vec{x}_0 + \int_0^t \vec{v}(t')dt' = \vec{x}_0 + \mu\int_0^t \vec{E}(\vec{x}(t'))dt' \tag{3.2}$$

where $\vec{x}$ and $\vec{v}$ are the instantaneous position and velocity and $\vec{x}_0$ is the initial position. Since the photogenerated charge cloud is not point-like, the equation of motion should be solved for the whole charge distribution by considering also the diffusion and Coulomb repulsion of the carriers. However, if we neglect self-shielding effects and we consider a nearly constant electric field in the volume region of the cloud, the broadening of the cloud can be decoupled from its trajectory. If we consider a gaussian initial charge distribution (Equation 2.33), the barycentre $\vec{x}_b$ follows Equation 3.2 whereas the time evolution of the variance is given by [8]

$$\sigma^2(t) = \sigma_0^2 + 2Dt + \frac{\mu N e}{2\sqrt{5}\epsilon}\int_0^t \frac{dt'}{\sqrt{\sigma^2(t')}} \tag{3.3}$$

where σ_0 is the initial variance, $D = \mu k_B T/e$ is the diffusion coefficient, k_B is the boltzmann constant, T is the temperature, N is the number of charges and ϵ is the electric permittivity of the semiconductor. In multi-electrode devices these assumptions do not hold in the proximity of contacts since the cloud can split and be collected by multiple electrodes, giving rise to the "charge sharing" effect [13, 14, 15]. Usually, this effect is relevant in pixelated detectors when the cloud dimension is not negligible in respect to the pixel size. During my PhD, I participated in a synchrotron session with the purpose of investigating this kind of distortion as described in Chapter 6. Figure 3.2 reports the time evolution of the cloud dimension for different energies of the primary photon [8].

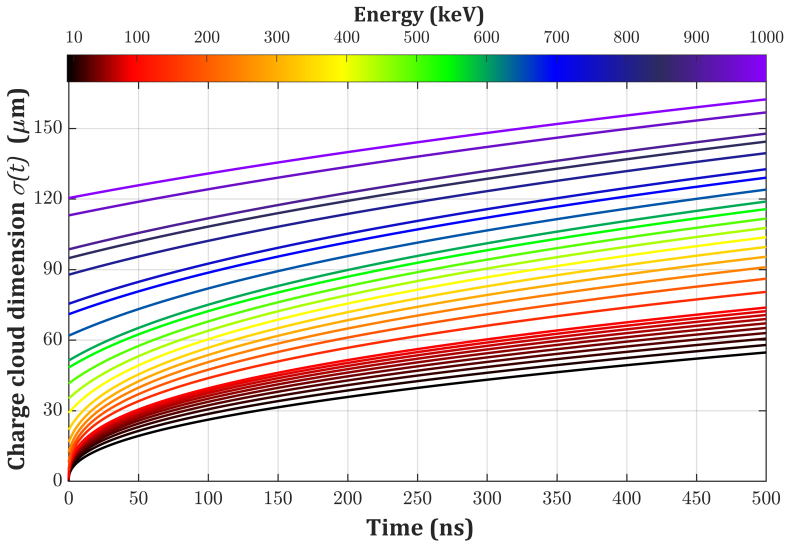

Figure 3.2: Time evolution of the charge cloud dimension due to diffusion and Coulomb repulsion in the 10^1–10^3 keV energy range.

The presence of defects in real semiconductors (e.g., vacancies, dislocations, grain boundaries) may produce energy levels inside the forbidden energy gap of which act as traps or recombination centres for electrons and holes. Thus, free carriers are characterised by a finite lifetime τ and an initial charge Q_0 decays in time according to:

$$Q(t) = \frac{\tau}{\tau + \delta} Q_0 + \frac{\delta}{\tau + \delta} Q_0 \mathrm{e}^{-\frac{t}{\tau} - \frac{t}{\delta}} \tag{3.4}$$

where the effect of de-trapping (defined by the characteristic time δ) has also been indicated. Usually, δ is longer than the transit time and its effect can be neglected, hence resulting in an exponential decay. The overall quality of the semiconductor is represented by the $\mu\tau$ product from which, assuming a constant electric field, the mean drift length can be calculated as $\lambda = \mu\tau|\vec{E}|$. If τ is comparable to the transit time or, analogously, if λ is comparable to the detector thickness, incomplete charge collection occurs. If there are large differences in the transport properties of electrons and holes, it is possible to neglect the contribution of the worse carrier by choosing a proper electrode configuration and to realize single polarity charge sensing devices (see Section 3.1.2).

3.1.2 Signal induction

The induction on the read-out electrode by the photogenerated carriers (i.e., the actual output signal of the RTSD) is described by the Ramo-Shockley theorem [16, 17]. It states that the induced charge and the corresponding induced current by a moving point charge Q at the time t are given by

$$Q_{ind}(t) = -Q\phi_W(\vec{x}(t))$$
$$I_{ind}(t) = \frac{dQ_{ind}(t)}{dt} \cdot \frac{d\vec{x}}{d\vec{x}} = -Q\frac{d\vec{x}}{dt} \cdot \frac{d\phi_W(\vec{x}(t))}{d\vec{x}} = Q\vec{v}(t) \cdot \vec{E}_W(\vec{x}(t)) \tag{3.5}$$

The weighting potential ϕ_W and the weighting field $\vec{E}_W = -\nabla\phi_W$ uniquely depend on the geometrical configuration of the electrodes and they can be calculated by solving the Laplace equation with Dirichlet boundary conditions in which all electrodes of the device are grounded except the considered one which is at unit potential. The complete description of the signal induction process can be achieved by substituting in Equation 3.5 the charge density and the relation between the velocity and the electric field (Equations 2.33 and 3.1, respectively) and by considering the time evolution of the charge cloud (Equations 3.2, 3.3 and 3.4):

$$I_{ind}(t) = \mu \iiint_V \rho_{ch}\left(Q(t), \vec{x}_b(t), \sigma(t)\right) \vec{E}(\vec{x}(t)) \cdot \vec{E}_W(\vec{x}(t))dV \tag{3.6}$$

It should be noted that electrons and holes possess different properties (m^*, μ, etc.) and the equations reported in Sections 3.1.1 and 3.1.2 must be solved for both carriers. Finally, by integrating $I_{ind}(t)$ over the carriers transit time (t_e and t_h for electrons and holes, respectively), the total collected charge Q_{coll} can be obtained as well as the Charge Collection Efficiency (CCE):

$$Q_{coll} = \int_0^{t_e} I_e(t)dt + \int_0^{t_h} I_h(t)dt \quad \longrightarrow \quad CCE = \frac{Q_{coll}}{Q_0} \tag{3.7}$$

CCE is the most important parameter which determines the overall performance of the device. Experimentally, the integration is performed by a Charge Sensitive Preamplifier (CSP) which produces a voltage output signal that is proportional to the collected charge. The preamplified pulses are then processed by the subsequent stages of the analog or digital read-out chain and are finally converted to an energy-resolved spectrum. The time required to process each event is limited by the counting rate and is usually short compared to the charge collection times. Depending on the interaction position, charge pulses may not reach the full height before being shaped, resulting in a ballistic deficit which degrades the spectra. The profile of ϕ_W can be optimized in order to sense only the charges that travel in the proximity of the read-out contact. Therefore, only the type of carrier which reaches the read-out electrode induces a signal. Single polarity charge sensing can be achieved by reducing one or both contacts dimensions (narrow strips or small pixels, from which the name "small pixel" effect) but other configurations exist (virtual Frisch grid [18, 19], coplanar grid [20, 21], drift strip [22, 23] quasi-hemispherical [24]). The qualitative trend of the electric and weighting field for these geometries is reported in [8].

3.1.3 Energy resolution

The energy resolution of the detector for a mono-energetic incident radiation is expressed as the Full Width at Half Maximum ($FWHM$) of the measured full energy peak (or photopeak) divided by its centroid, usually indicated in percentage:

$$R(E) = 100 \cdot \frac{FWHM}{E} \quad (\%) \tag{3.8}$$

The photopeak is the measured counts distribution in the case of a full energy deposition, either via a single photoelectric interaction or any combination of all the mechanisms (see Figure 3.4). Several noise sources contribute to broaden the photopeak and, in general, $FWHM$ is given by the sum in quadrature of all the fluctuations involved in the generation and processing of the signal [3, 25]:

$$FWHM^2 = FWHM^2_{noise} + FWHM^2_{Fano} + FWHM^2_{trap} + FWHM^2_{dark} + ... \tag{3.9}$$

$FWHM_{noise}$ is related to the noise of the read-out system and is usually the dominant term. $FWHM_{Fano}$ is related to the statistical fluctuations in the generation of the e-h pairs (Fano noise) and it represents the lower bound of $FWHM$ since it depends only from the semiconductor properties (electron-hole pair creation energy $E_{e\text{-}h}$). The term $FWHM_{trap}$ is related to charge transport and collection: depending on the interaction position, carriers incur in different trapping processes along their paths and poor transport properties lead to incomplete charge collection and asymmetric photopeaks ("tailing effect"). $FWHM_{dark}$ is related to the fluctuations of the dark current whose extent depends from the semiconductor properties, the quality of surfaces, the metal contacts and the applied bias voltage. In fact, in intrinsic semiconductors in thermal equilibrium, the free carrier density per unit volume in the conduction and valence bands is calculated according to the formula [26]:

$$n = p = n_i \propto T^{3/2} \exp\left(-E_G/2k_BT\right) \tag{3.10}$$

where n_i is the intrinsic carrier concentration, n and p are the electrons and holes density, respectively, T is the temperature and k_B is the Boltzmann constant. n and p in turn determine the conductivity (σ) and resistivity ($\rho = 1/\sigma$) and, hence, the drift current density $\vec{J}_{drift}$ if an electric field is present within the semiconductor:

$$\sigma = e(n\mu_e + p\mu_h) \quad \rightarrow \quad \vec{J}_{drift} = \sigma\vec{E} = \frac{\vec{E}}{\rho} \tag{3.11}$$

where σ is a scalar in isotropic semiconductors. This is the crux of Room Temperature (RT) operability and the reason why the research moved to wide band gap compensated semiconductors. Correspondingly, low $E_{e\text{-}h}$ as well as low thermal excitation of carriers (described by Equations 2.31 and 3.10, respectively) are the key features behind the excellent signal-to-noise ratio of cooled Si- and Ge-based detectors. In most semiconductors, the presence of defects on the surfaces of the crystal create electronic

states in the energy gap, resulting in local doping and leading to higher conductivity with respect to the bulk. The surfaces contribute can be reduced by passivation (oxidation of the superficial states) or even neglected by surrounding the read-out electrodes with a grounded guard-ring contact which collects the surface current. Moreover, an important role is played by the metal-semiconductor junction: depending on the metal, different types of band alignment may occur, resulting in blocking (Schottky) or ohmic contacts according to the work functions of the two materials and the nature of the superficial states. The former are characterised by an energy barrier which prevents the injection of carriers from the metal to the semiconductors, thus reducing the leakage current (diode-like behaviour). On the other hand, they may produce charge accumulation at the interface (usually at high radiation flux) which distorts the electric field and degrades the charge collection. In this case, the latter type of contact is usually preferred. The behaviour of Schottky barrier diodes can be modeled according to the interfacial layer-thermoionic-diffusion theory [27]. The measurement of the current/voltage (I/V) characteristics is always mandatory to determine the optimal applied voltage in operating conditions which is always a matter of compromise since higher biases ensure better charge collection but increase the dark current as well.

The measured spectrum is the result of all the effects described in Chapters 2 and 3. An example of ^{137}Cs spectrum measured with a CZT detector is reported in Figure 3.3. The physical explanation of the features present in the measurement and of other possible distortions is reported in Figure 3.4 where the effect of the surrounding is also highlighted (image courtesy of [28]).

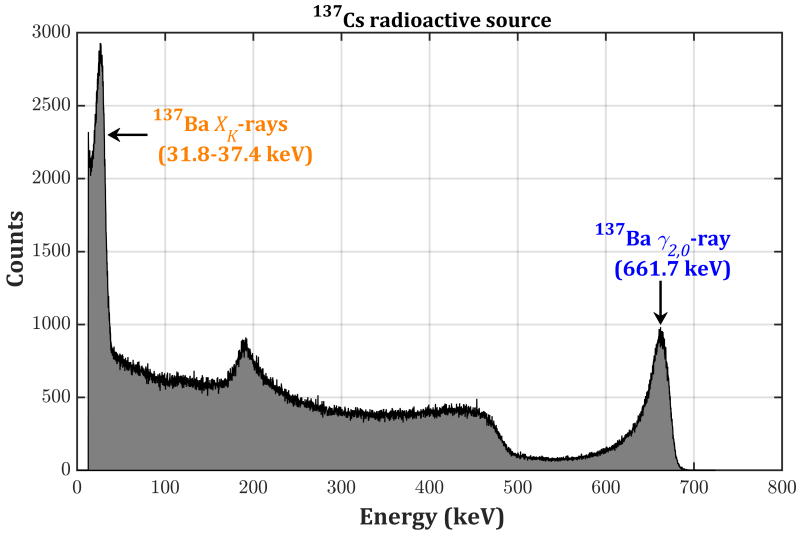

Figure 3.3: Experimental spectrum of a ^{137}Cs radioactive source measured with a CZT-based detector. ^{137}Cs decays by β^--emission to the excited state of ^{137}Ba; the subsequent isomeric transition and electron rearrangement produce the radiation indicated in the figure.

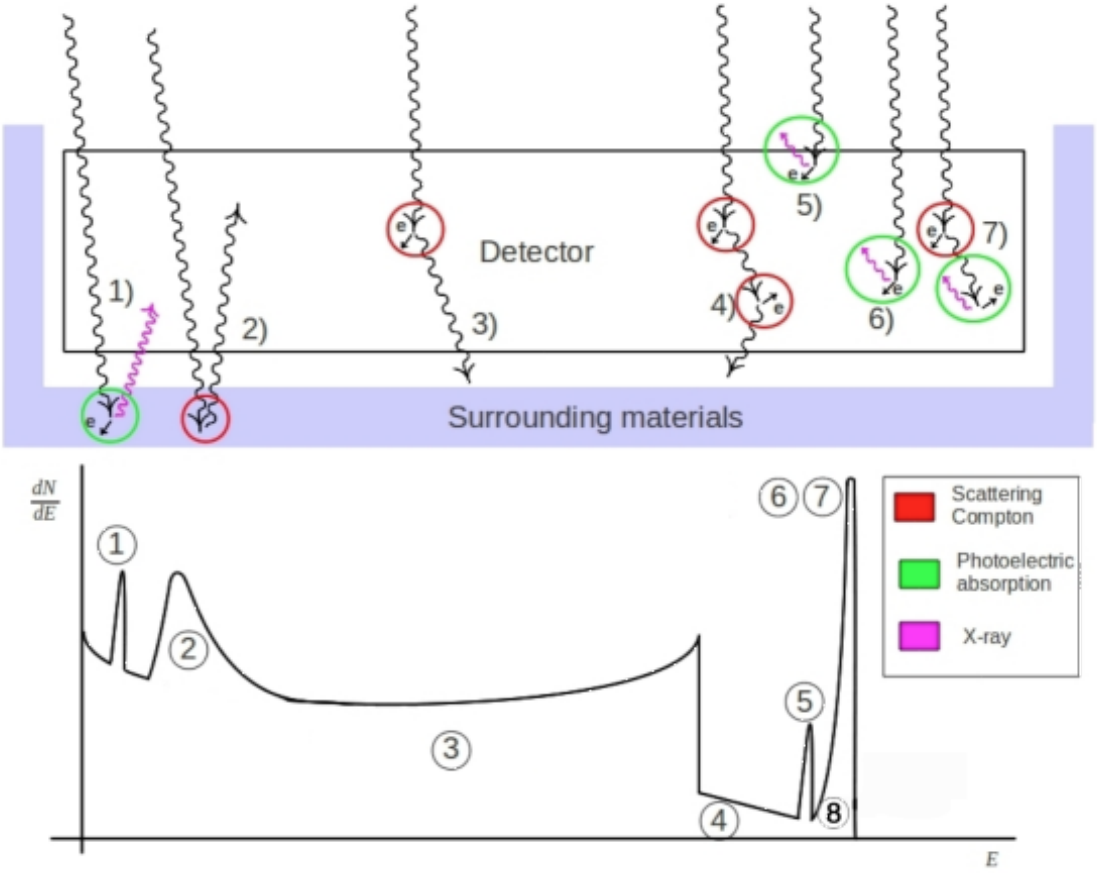

Figure 3.4: Schematic representation of photoelectric and Compton interaction and subsequent mechanisms in a semiconductor detector and objects in its surroundings (top) and corresponding energy spectrum (bottom). 1) Fluorescence peak; 2) backscatter peak; 3) Compton edge; 4) double Compton events; 5) escape peak; 6-7) photopeak (full energy deposition); 8) tailing effect.

3.2 Cadmium Zinc Telluride

Commercially, only Ge-, Si-, CdTe- and CZT-based detectors are available but several other compounds emerged during the decades. The choice of the material for realizing a semiconductor radiation detector is strongly dependent on the final application. Since an extensive comparison is beyond the scope of this thesis, I will restrict myself in describing the strengths and weaknesses of CZT in the context of spectroscopic γ-ray detectors.

3.2.1 Material properties

Cadmium Zinc Telluride ($Cd_{1-x}Zn_xTe$ or CZT) is a ternary alloy of CdTe where Zn atoms are randomly substituted to Cd ones. As many II-VI semiconductors, CdTe and ZnTe are completely miscible and CZT inherits both the crystallographic and electronic band structures of the parents binary compounds. CZT has a cubic zinc blende structure (space group $F\bar{4}3m$) whose lattice parameter ($\boldsymbol{d}^{CZT}$) is given approximately by the weighted mean of the lattice parameters of CdTe and ZnTe at the same temperature, according to the Vegard's law for solid solution [29]:

$$\begin{aligned} \boldsymbol{d}^{CZT}(x) &= (1-x)\boldsymbol{d}^{CdTe} + x\boldsymbol{d}^{ZnTe} = \\ &= 6.4810(1-x) + 6.1026x \quad \text{Å} \end{aligned} \tag{3.12}$$

The band structure presents a direct bandgap whose energy gap can be calculated in a similar way but in this case a corrective term must be added to consider the effect of the short range disorder which breaks the translational symmetry [29]:

$$\begin{aligned} E_G^{CZT}(x) &= (1-x)E_G^{CdTe} + xE_G^{ZnTe} - x(1-x)b = \\ &= 1.51 + 0.591x + 0.158x^2 \quad \text{eV} \end{aligned} \tag{3.13}$$

where $b = 0.158$ is the bowing parameter. The substitution with Zn has several consequences on the material properties of CZT. The primary consequence of the increased band gap is a higher bulk resistivity ($10^{10} \div 10^{11}$ Ω·cm vs 10^9 Ω·cm of CdTe). However, by increasing the Zn fraction the hole transport properties worsen whereas the electron ones remain nearly the same (see Table 3.1). For these reasons, x is usually in the $0.1 \div 0.2$ range for radiation detector applications. Poor hole lifetime is one of the main downsides of CZT and, in the case of thick crystals (> 5 mm), electron sensitive detectors must be realised [18, 19, 20, 21, 22, 23, 24].

Additionally, CZT is affected to a much lesser extent than CdTe by the polarization effect for which space charge builds up in the crystal when the bias voltage is applied. This gradually alters the electric field profile and compromises the charge collection efficiency by forming a dead layer even in absence of radiation. The origin of polarisation is still debated and increases with the bias voltage and thickness. As a matter of fact, CdTe-based RTSDs are usually not thicker than 2 mm whereas in the case of CZT the limit is given by the transport properties and crystal homogeneity. Nowadays, typical

thicknesses are generally lower than 1.5 cm even if detectors up to 5 cm thick have been successfully realised [30].

Large CZT ingots can be grown up to several centimeters in thickness with different techniques. Commercial CZT (Redlen, Kromek, Imdetek, Imarad) is mainly grown with the traveling heater method and Bridgman techniques in all its variations (low and high pressure). At the IMEM-CNR institute, CZT growth is performed with the Boron encapsulated vertical Bridgman technique [31, 32]. The liquid B_2O_3 layer which surrounds the melt during the growth prevents element losses (mainly Cd due to the non-congruent evaporation at the melting point) and, at the same time, prevents oxygen contamination due to the interaction with the quartz crucible. Usually, group III elements (Indium in the case of IMEM-CNR) are employed as dopant to produce compensated ingots. Crystal growth is still one of the most challenging aspects of CZT due to poor thermal conductivity of the solid which leads to inhomogeneous heat distribution within the growing crystal and, consequently, inhomogeneous crystal quality. Furthermore, CdTe and CZT ingots are characterised by Te-inclusions which form at the liquid-solid interface and are incorporated in the crystal matrix [33]. The Te-rich melt, growth rate and temperature gradients are responsible for the generation of such defects whose diameter spans from few to few tens of μm. The dimensions and concentration of Te-inclusions represent a strong limit since they act as recombination centres and lower the overall transport properties of the compounds [34, 35]. Other types of defects are frequent such as dislocations (due to the low critical resolved shear stress), twins (whose formation energy is low in CZT), grain boundaries (common in unseeded growth techniques) and even cracks (caused by thermal and mechanical stress during the cooling of the ingot) [36].

3.2.2 CZT as radiation detector

Table 3.1 compares the relevant properties of some semiconductors used for radiation detectors [37]. The primary virtues of CZT are definitely the high atomic number and density which guarantee an efficient stopping power in the region of interest of hard X- and soft γ-ray. Furthermore, photoelectric effect is the main interaction mechanism up to $\approx$ 200 keV. Figure 3.5 compares the attenuation coefficient in the 10^1–10^4 keV energy range for the semiconductors compounds listed in Table 3.1.

Secondly, the energy gap of CZT is the best compromise between sensitivity and RT operability: as already explained, the amplitude of the signal is inversely proportional to E_G; by contrast, small E_G leads to high dark current (i.e., noise). CZT also presents a relatively high $\mu_e\tau_e$ among the high Z semiconductors, hence ensuring a good collection efficiency even for thick detectors provided that the contribution of hole is neglected.

CZT-based detectors can be reproducibly realised with a good yield both in industries and in research laboratories. Nonetheless, the fabrication process is less consolidated than the one of its binary parent (CdTe) and it is far from being problem-free. Cutting, lapping and polishing are delicate procedures owing to the brittleness of CZT and obtaining sharp edges is difficult. Contact deposition, on par with crystal growth,

Table 3.1: Properties of semiconductors used for radiation detectors at 25 °C (reference in the text).

Material	**Si**	**Ge**	**GaAs**	**CdTe**	**CZT**[a]	**TlBr**	**HgI_2**	**SiC**
Average Z	14	32	32	50	49.1	58	62	10
ρ_m (g/cm^3)	2.33	5.33	5.32	6.2	5.78	7.56	6.4	3.2
E_G (eV)	1.12	0.67	1.43	1.44	1.57	2.68	2.13	2.2
$E_{e\text{-}h}$ (eV)	3.62	2.96	4.2	4.43	4.6	6.5	4.2	9.0
ρ (Ω·cm)	up to 10^4	50	10^7	10^9	$10^{10\div11}$	10^{12}	10^{13}	
$\mu_e\tau_e$ (cm^2/V)	>1	>1	8×10^{-5}	3.3×10^{-3}	2×10^{-3}	1.6×10^{-5}	10^{-4}	
$\mu_h\tau_h$ (cm^2/V)	≈1	>1	4×10^{-6}	2×10^{-4}	10^{-5}	1.5×10^{-6}	4×10^{-5}	

[a] $Cd_{0.9}Zn_{0.1}Te$

represents the major obstacle. Moreover, some works reports the instability of CZT above 150-200 °C which prevents the use of high temperature deposition techniques and annealing treatment, commonly used to improve the mechanical adhesion of metal on semiconductors [38, 39]. Therefore, the realisation of homogeneous, thick and stable contacts (both mechanically and over time) is still a hot research topic. Only few metals can be deposited on CZT; the most common ones are Au and Pt which are deposited through electroless, sputtering or evaporation techniques [40, 41, 42]. Finally, depending on the metal, electrode patterning can be challenging and pixels smaller than 40 μm are arduously realised.

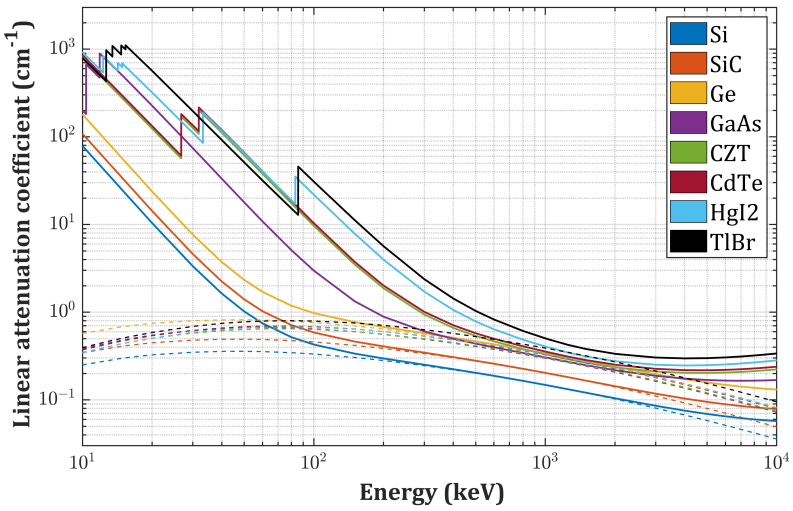

Figure 3.5: Total (full curves) and Compton (dashed curves) linear attenuation coefficient for some semiconductors used for γ-ray detectors in the 10^1–10^4 keV energy range.

Part II

Results

Chapter 4

Unfolding of γ-spectra with genetic algorithm

Inverting the instrumental response function in order to extract the ground truth behind a measurement has been a goal pursued for a long time by experimental scientists, especially in fields where the relevant information may be concealed or distorted owing to instrumental non-idealities. RTSDs represent a clear example where partial energy deposition of the radiation within the semiconductor, incomplete charge collection and instrumental noise conceal the true spectral shape and prevent a straightforward data analysis. Although accurately simulating the spectral response of the device is possible, using it to reverse the process, referred to as spectral unfolding or deconvolution, is arduous due to the instability of the problem. Its mathematical complexity encouraged the scientific community to develop innovative and more robust methods to unfold experimental spectra. Recently, thanks to the increasing popularity of machine learning, to which genetic algorithm belongs, alternative approaches have been proposed, allowing to face the problem in a new way.

In the first part of this chapter the theory of spectral unfolding and the main methods are briefly described. In the second part, the proposed unfolding method based on a genetic algorithm, which I developed during my Ph.D., is presented as well as the simulation toolkit used to reproduce the response function of the detector. In the last part, the method is validated on experimental measurements of four radionuclides acquired with two different detectors.

4.1 Concepts of spectral unfolding

The final goal of analysing γ-spectra is the identification of radioisotopes. This is a typical pattern recognition problem which can be addressed with various approaches (e.g., peak search and match, template matching) [43] and it could be difficult for devices with low or average energy resolution where relevant features are hidden or masked. Spectral unfolding consists in restoring the energy distribution of the incident radiation by inverting the transfer function of the device and, in the case of γ-spectra, it should extract δ-like peaks corresponding to the characteristic emissions of radioactive sources. Mathematically, this consists in inverting the Fredholm integral equation of the first kind which describes the response of the instrument at low radiation flux [44, 45]:

$$\mathrm{M}(E) = nS(E) = n_0 \int_0^\infty R(E, E')D(E')\Phi(E')dE' \tag{4.1}$$

where $\mathrm{M}(E)$ is the measured spectrum, n is the total number of detected counts, $S(E)$ is the Probability Density Function (PDF) of the energy distribution of $M(E)$, n_0 is the number of incident photons, $\Phi(E')$ is the PDF of the energy distribution of the incident radiation, $D(E')$ is the detector absorption efficiency and $R(E, E')$ is the spectral response function of the detector. For the sake of clarity, $D(E')$ defines the probability that a photon of energy E' interacts at least once with the crystal regardless of whether a full energy deposition occurs (Rayleigh scattering is excluded since no energy is released). The meaning of $R(E, E')$ is straightforward if we consider a monochromatic incident radiation ($\Phi(E') = \delta(E' - E'_0)$) and a complete efficiency ($D(E'_0) = 1$):

$$S(E) = \int_0^\infty R(E, E')D(E')\delta(E' - E'_0)dE' = R(E, E'_0) \tag{4.2}$$

By way of explanation, $R(E, E')$ represents the PDF that an incoming photon of energy E' produces a pulse height signal E. Both $\Phi(E')$ and $S(E)$ are continuous distributions but, experimentally, the detection occurs in a finite energy range divided in N channels with constant width ΔE. The number of counts in the i-th channel is given by

$$n_i = nS_i = n \int_{E_{i-1}}^{E_i} S(E)dE \quad \text{with} \quad E_i = E_{i-1} + \Delta E \quad \text{and} \quad i = 1, \ldots, N \tag{4.3}$$

Consequently, the knowledge of $\Phi(E')$ is primarily limited by the instrumental discretisation which prevents us from obtaining information with a finer energy resolution ($\Delta E' = \Delta E$). Therefore, Equation 4.1 is discretized as follows:

$$\vec{S} = \mathbf{R} \cdot \vec{D} \circ \vec{\Phi} \quad \text{or} \quad S_i = \sum_{j=1}^{M} R_{ij} D_j \Phi_j \quad \text{with} \quad i = 1, \ldots, N \tag{4.4}$$

where $N \geq M$ (linear overdetermined system) (scale factors n and n_0 are dropped). Now, the j-th column of $\mathbf{R}$ represents the ideal measured spectrum for a monoenergetic

radiation of energy between E'_{j-1} and E'_j. As already explained in the previous chapters and exemplified in Figure 3.4, $\mathbf{R}$ can have a complex structure and is typically quasi-singular, especially at high energies where photoelectric interaction is less probable. Moreover, the measurement can be contaminated by photons whose energy falls outside the upper and lower thresholds of the observed spectrum. Finally, the problem is further complicated by the presence of experimental noise, defined as the deviation from the expected value, which modifies Equation 4.4 into

$$\vec{S} = \mathbf{R} \cdot \vec{D} \circ \vec{\Phi} + \vec{\epsilon} \quad \text{or} \quad S_i = \sum_{j=1}^{M} R_{ij} D_j \Phi_j + \epsilon_i \quad \text{with} \quad i = 1, \ldots, N \tag{4.5}$$

If solutions $\vec{s}$ satisfying $\mathbf{R} \cdot \vec{s} = 0$ or $\mathbf{R} \cdot \vec{s} = \vec{f}$ (with $f_i \ll \epsilon_i$) exist, they can be added to the true solution $\vec{\Phi}$ without invalidating Equation 4.5 but, since the problem is unstable to small fluctuations, these additional terms may dominate in respect to $\vec{\Phi}$, thus making the number of potential solutions infinite within error bounds. Consequently, if we just apply $\mathbf{R}^{-1}$ to an observed spectrum, small variations can produce unphysical features in the unfolded spectrum such as enormous oscillations and negative values (Figure 4.1). Therefore, the problem is ill-conditioned and ill-posed. This is the reason why least-squares methods usually fail and deconvolution methods, which are more stable with respect to uncertainties, are employed. Several approaches have been proposed in various context (least-squares [46, 47], Monte Carlo [48, 49], iterative [50, 51, 52, 53, 54], Bayesian [55, 56, 57], neural networks [58, 59, 60], genetic algorithm [61, 62]).

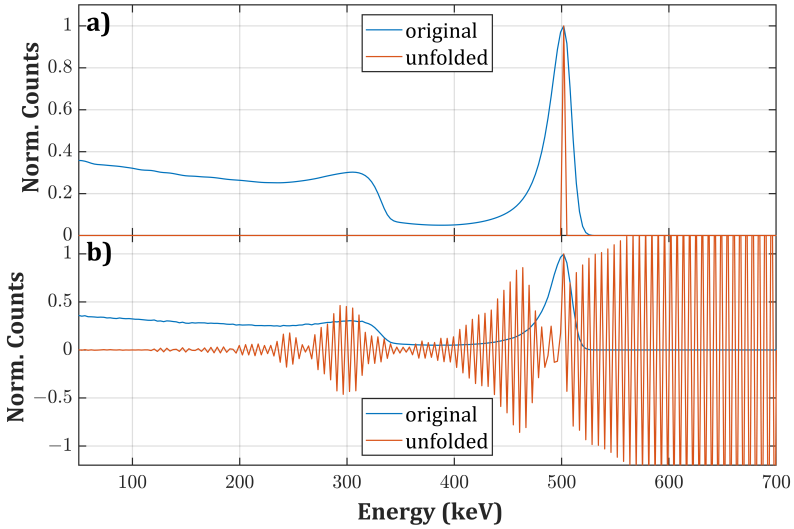

Figure 4.1: a) Ideal synthetic spectrum (i.e., a column of $\mathbf{R}$) for a monoenergetic radiation of 500 keV (blue curve) and its deconvolution after applying $\mathbf{R}^{-1}$ (orange curve). **b)** Same spectrum after adding a negligible gaussian noise (blue curve) and its deconvolution after applying $\mathbf{R}^{-1}$ (orange curve).

4.2 Calculation of the detector response function

Although the robustness and effectiveness of the unfolding method are of primary importance, an accurate response matrix is the key to obtain fine results. Otherwise, the deconvolution will fail to succeed, regardless of the chosen algorithm. **R** can be obtained both with experiments and calculations. The former method is definitely the most accurate since it allows to portray the exact behaviour of the detector: it consists in measuring spectra of monochromatic sources at different energies and using them to map **R** in the whole desired energy space by interpolation. However, it is also the less viable one: firstly, it is extremely resource demanding and time consuming since it requires facilities like synchrotrons; secondly, **R** would be characteristic of that specific detector and adapting it to another one may not be trivial, even if they have the same characteristics. For these reasons, synthesized response matrices are usually employed.

Simulations of the spectral response of a detector is a common procedure since when the first lithium-drifted Si and Ge semiconductor detectors appeared on the scene [63, 64, 65, 66]. At that time, the simulations considered only the effects of the interaction of radiation with the crystal. The introduction of high Z compounds like CdTe, which presented worse transport properties in respect to Si or high purity Ge, imposed to include the degradation effects inherent to the collection efficiency of photogenerated charges and to signal processing [67, 68, 69, 70, 71]. Finally, as the photolithographic techniques progressed, the simple planar-planar geometry was abandoned and more complex electrode patterns were realised in order to neglect the contribution of slow carriers (single polarity charge sensing). Consequently, signal induction was necessarily included in the modelling [70, 72].

The purpose of the transfer function of a radiation detector goes beyond spectral deconvolution, even if it is its primary function. Since the processing of CZT crystals still presents several criticalities (crystal cutting and polishing, metal contact deposition and patterning, as explained in Chapter 3.2), the fabrication of device with unusual or complex dimensions and/or electrode geometries can be risky, especially in an industrial context where to limit the failure rate is a priority. Therefore, the design phase and engineering of each aspect which can invalidate the functioning of the device is even more crucial in saving time and costs. Beyond this, improving the energy and spatial resolution and charge collection efficiency is definitely possible through simulations only. In this context, my research group developed in collaboration with Xnext s.r.l. a simulation toolkit able to reproduce the spectral response of these devices by first principles methods [8] which includes each step of the signal generation process:

- interaction of the photon with the semiconductor
- transport and collection of carriers
- signal induction and processing

Since these processes can be treated independently, the simulator is composed of multiple blocks, each having different tasks.

4.2.1 Radiation-matter interaction

The first block is devoted to the simulation of the transport of particles through matter via Monte Carlo calculations, ideal to reproduce the stochastic nature of the physical interaction mechanisms described in Chapter 2, and is based on Geant4 [73], largely used in the field of X- and γ-ray spectroscopy [72, 74, 75, 76, 77]. G4EmStandardPhysics and G4EmLivermorePhysics packages consider all the required electromagnetic interactions in the energy range from few keV to few MeV.: pair production, Compton scattering, Rayleigh scattering and photoelectric effect for photons; elastic and inelastic scattering, Bremmsstrahlung and annihilation for electrons and positrons. The cross sections for each mechanism are calculated via formulas, parametrisations or interpolation of databases. Geant4 allows to define the geometrical configuration of the whole system: crystal dimensions, direction and shape of the photon source, presence of collimators or filter and other possible elements. Geant4 tracks each primary or secondary particle and records the information on each collision: the interaction position and energy released within the sensitive volume are saved into a file. The required number of events generated to simulate each column of $\mathbf{R}$ is typically in the order of 10^6 to obtain high statistical significance.

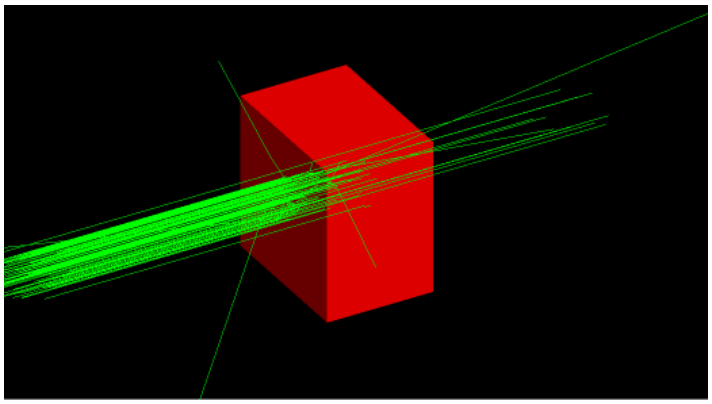

Figure 4.2: Example of Geant4 simulation: the red parallelepiped represents a CZT crystal and green lines represent incident or scattered photons.

4.2.2 Electric and weighting fields

The task of the second block is calculating the electric and weighting fields within the crystal volume by solving the Poisson's equation

$$\nabla^2 \varphi = -\frac{\rho}{\varepsilon} \tag{4.6}$$

where φ is the electric potential, ρ is the charge density and ε is the electric permittivity of CZT. Given the geometry of the system (crystal and electrode dimensions and patterning) and the boundary conditions (applied bias voltage at each electrode), the

electric potential can be calculated by finite elements method. This approach is valid if the photogenerated charges do not significantly perturb the electric field (quasi steady-state condition). Consequently, the Poisson's equation can be decoupled from the continuity equations for electrons and holes. This condition is guaranteed since CZT is less likely to suffer from self-polarisation, which would lead to a charge accumulation, and the consequent formation of a dead layer below one of the contacts.

Similarly, the weighting potential can be calculated by solving the Laplace's equation with boundary conditions in which all electrodes are grounded except the considered one which is set at unitary potential [16, 17]). These operations are performed by the software COMSOL MultiPhysics (electrostatics package) which allows the design of the desired geometry of the system and automatically creates an adaptive mesh in the volume (typical element dimensions span from 50 nm to 100 μm). After the calculation, the potentials are extrapolated and exported on a uniform 3D cubic grid with ≈ 5 μm steps, depending on the detector geometry and dimensions. Two examples are reported in Figure 4.6.

4.2.3 Charge transport and signal induction

Basically, this block has the purpose of solving Equations 3.5, 3.6 and 3.7 to calculate the charge transport and signal induction. Firstly, the trajectories of electrons and holes are calculated by means of Ordinary Differential Equation (ODE) solver which exploits the initial conditions provided by the GEANT4 block and the field profile calculated with COMSOL. Although charge clouds have finite dimensions, in most cases the motion equations of the barycentre can be decoupled from the broadening of the cloud. This simplifies the calculations even if it implies that clouds cannot split and be collected from multiple electrodes (charge sharing effect). The knowledge of trajectories allows us to calculate the induced current via Ramo–Shockley's theorem. The operations carried out by the electronic read-out chain are applied to the current transient to shape the pulse and calculate its height. Finally, the spectrum can be reconstructed by positioning each count in the corresponding energy channel. The effect of noise broadening can be performed in two ways: (a) convolving the pulse height spectrum with a gaussian kernel (or any other suitable kernel); (b) adding the noise directly to the simulated current pulses. The former method is usually preferred because the kernel width is characteristic of the read-out system and it can be easily measured. In the latter case, the noise spectral density must be known. This block has been implemented in MATLAB.

4.3 Genetic algorithm

Genetic Algorithm (GA) is inspired by the darwinian theory of natural selection and is a branch of the evolutionary computation family [78, 79, 80]. It emulates the process of selection performed by a hostile environment on a population of individuals: the ones with the best characteristics are more likely to pass down their gene pool to the offspring whereas unfit individuals die without reproducing ("survival of the fittest"). As a result, the overall fitness of the population will increase through generations. In computer science, the individuals (or solutions) are arrays of bits/integers/real numbers which undergo four basic operations:

- initialization of the first generation
- selection of individuals for mating
- generation of new individuals
- mutation of the genome in new individuals

Several methods to perform these operations have been developed and the choice depends on the specific problem to solve. A proper objective function f represents the fitness: with the passing of generations the population evolves towards better solutions in order to maximize (or minimize) f. GAs are usually employed in optimization and search problems and they have already been applied to unfold neutron spectra [61, 62]. Since the principles are the same, I wrote my own code to deal with γ-spectra. In this context, individuals represent potential incident energy PDF. They consist of vectors of non-negative values with unitary area and their genes s_j, that is the normalized number of counts in each channel, ultimately determine how the measured spectrum would appear through the convolution with the response function $\mathbf{R}$. Thus, the fitness is defined as

$$f = \frac{1}{N} \sum_{i=1}^{N} \left(\sum_{j=1}^{M} R_{ij} \cdot D_j s'_j - S_i \right)^2 \tag{4.7}$$

where s' is a potential solution. Therefore, the best individual is the one that minimizes the normalised residual sum of squares between its convolution with $\mathbf{R}$ and the observed spectrum S. In order to maximize the exploration of the solution space, the initial population is randomly generated and it is composed of N_s individuals. The selection is performed by running "tournaments" in which the fitness values of the contestants, randomly chosen among the population, are compared. The winner is the one with the lowest f and obtain the right of procreating:

$$winner = \arg\min(f(s'), f(s'')) \tag{4.8}$$

where s' and s'' are two randomly drawn individuals. The number of tournaments is given by the $N_s \cdot P_c$ product where P_c is the crossover probability (see Table 4.1). Then, the $N_s \cdot P_c$ selected individuals are combined in pairs to produce an equal number of offspring: given two parents $\vec{P}_1$ and $\vec{P}_2$ (i.e., the winners of two different tournaments), the offspring $\vec{O}_1$ and $\vec{O}_2$ are defined as the weighted average of the parents:

$$\begin{aligned} \vec{O}_1 &= w\vec{P}_1 + (1-w)\vec{P}_2 \\ \vec{O}_2 &= (1-w)\vec{P}_1 + w\vec{P}_2 \end{aligned} \tag{4.9}$$

where $0 < w < 1$ is a constant (see Table 4.1). Each new generated solution is mutated by replacing the values of randomly selected channels with a random value in the interval $[0, m \cdot s_j]$ where s_j is the value of the j-th channel and m is a tuned parameter (see Table 4.1). The number of mutated genes is given by the $P_m \cdot N$ product where P_m is the mutation probability (see Table 4.1). Usually, a smoothing step is required since highly oscillating solutions can still give good results because of the quasi-singularity of $\mathbf{R}$ [81], although this operation would also broaden true peaks. However, in this case smoothing is not required thanks to the choice of the crossover method which allows to attenuate great differences among individuals without smearing out the real characteristic lines. After normalising the area of the mutated offspring, the fitness is evaluated for all the new individuals and the entire population is resized by discarding the worst ones (elitist selection). These operations are repeated until a maximum number of iterations is reached or when f falls below a certain threshold. The values of the parameters used in each step are reported in Table 4.1 and the flow chart of the code is shown in Figure 4.3. A calibration procedure has been performed to tune them to obtain the best overall performances in terms of running time (time required per each generation) and convergence speed (number of generations required to reach the goal). As a matter of fact, increasing the size of the population and the number of offspring would indeed reduce the number of generations required since the solution space is better explored but at the expense of more computations. Analogously, excessive mutations would produce worse individuals than the corresponding parents, thus not producing actual improvements. On the other hand, slight mutations would reduce the convergence speed. Therefore, the pairs $[N_s, P_c]$ and $[P_m, m]$ have been jointly optimised by progressively sampling the values of both parameters in a selected range whereas w has been tuned separately. The values which provided the best results on a reference spectrum have been selected. In reality, all parameters are inter-correlated, to a greater or lesser extent, but it would be arduous to simultaneously tune all of them. The algorithm has been implemented in MATLAB.

It is worth noting that $\mathbf{R}$ is always used directly to fold potential solutions without the need of inverting it. As a matter of fact, the task of GA is neither inverting $\mathbf{R}$ nor finding the mathematical solution to this problem: it searches for an approximate and physically reasonable solution which best matches the measured spectrum. The physical validity of the solution is guaranteed by the fact that the mutation process can only produce non-negative values.

GA parameters		
N_s	Size of the population	50
P_c	Crossover probability	0.8
P_m	Mutation probability	0.01
w	Crossover weight	0.3
m	Mutation upper bound	3

Table 4.1: Description and values of the parameters used in the GA.

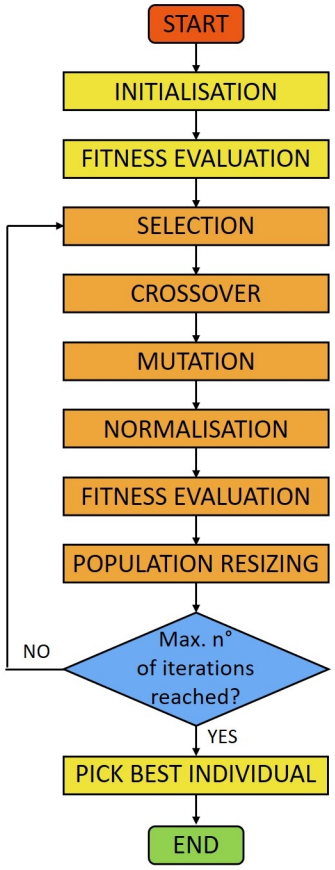

Figure 4.3: Flowchart of the GA used in this work. The preliminary and final steps are highlighted in yellow whereas the operations involved in the loop over the generations are highlighted in orange.

4.4 Experimental validation

The algorithm has been validated on experimental spectra measured with two different CZT-based detector: ^{137}Cs and ^{133}Ba measured with the drift strip detectors; ^{241}Am and ^{57}Co measured with the single pixel detector;.

4.4.1 CZT detectors

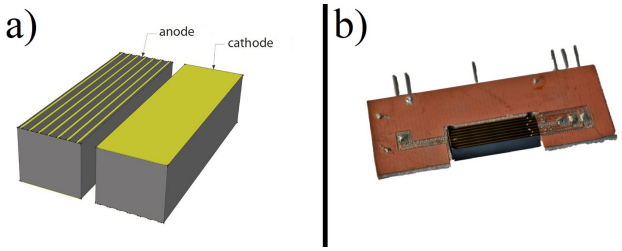

Figure 4.4: a) 3D model of the drift strip detector. **b)** Actual CZT detector bonded to the intermediate electronic board.

The first detector consists of a $20 \times 4.5 \times 6$ mm^3 crystal realized by reprocessing standard spectroscopic grade CZT material purchased from REDLEN Technologies. The crystal presents a strip electrode geometry: the anode is segmented in seven 250 μm strips with an intergap of 550 μm whereas the cathode is full area (Figure 4.4). Contacts have been realized with gold electroless deposition in aqueous solution. Starting from the most external to the central one, during the measurements the strips are polarized at -450 V, -300 V, -150 V and 0 V, respectively, and the cathode at -450 V. This geometry allows the carriers to drift towards the collecting central strip and guarantees a high energy resolution above 100 keV regardless of the irradiation direction. In fact, this detector has been mounted on an unmanned aerial vehicle with the purpose of examining contaminated areas [82, 83]. The analog readout system has been developed by due2Lab s.r.l. The readout channel includes a Cremat CR110 CSP (decay time = 140 μs), a shaper amplifier (shaping time = 2 μs) and a peak detector. The energy resolution is 3.9% FWHM @662 keV.

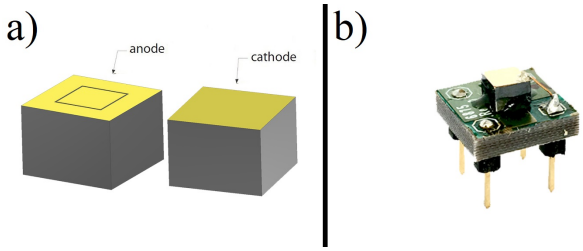

Figure 4.5: a) 3D model of the single pixel detector. **b)** Actual CZT detector bonded to the intermediate electronic board.

The second detector consists of a $4.1 \times 4.1 \times 2.8$ mm^3 detector obtained by reprocessing a standard CZT crystal purchased from REDLEN Technologies (Canada) with a full-area cathode, a 2×2 mm^2 pixel and a guard ring on the anode with a gap of 50 μm (Figure 4.5). Sensor refabrication has been carried out by due2lab s.r.l.; gold contacts were fabricated using the electroless deposition process from alcoholic solution as described in [84, 85]. The detector was biased at -850 V and it was irradiated from the cathode side. The CZT sensor unit (D2L001) and the single-channel digital pulse processor unit (D2L009-1) are part of the Hyperspectral X-ray Spectrometer (HXS) developed by due2lab. The energy resolution is 4.0% FWHM @60 keV.

4.4.2 Response matrices

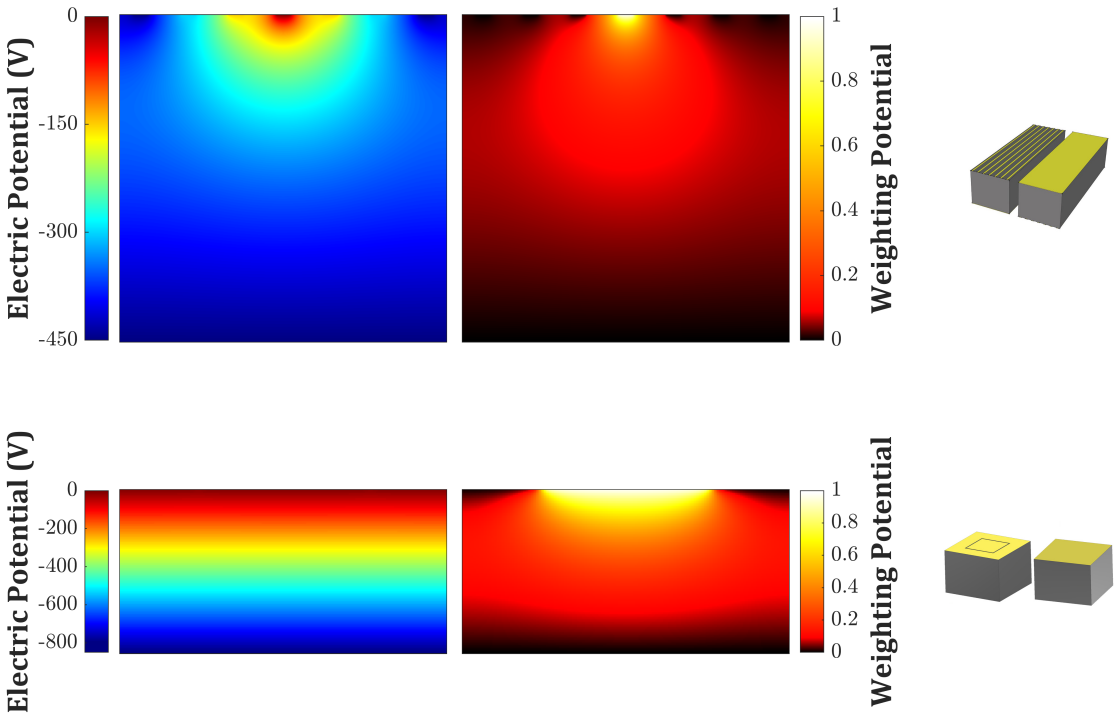

Figure 4.6: Transversal sections of the electric potential (left) and weighting potential (right) for the drift strip (top) and single pixel detectors (bottom). In the case of the drift strips detector, the "small pixel" effect is evident.

The response functions of both detectors have been obtained using the simulation tool described in Section 4.2 in the 0–750 keV and 0–150 keV energy ranges for the drift strips and single pixel detectors, respectively, each divided in 256 channels. In the former case, a isotropic irradiation from the whole solid angle has been considered because this configuration is the most similar to the sensor real operation environment, whereas in the latter only the cathode side has been exposed in which the trajectories of incident

photons are orthogonal in respect to the face of the detector (source at infinity). This is a good approximation of the geometrical configuration of the real measurement. As can be seen in Figure 4.7, Compton scattering quickly becomes the dominant effect for the drift strips detector which flattens the intensity of the photopeak. On the other hand, for the single pixel detector the main distortions are the escape peaks (off-diagonal lines) due to the small volume of the crystal. Additionally, at high energies hole tailing becomes significant because the probability of interaction near the anode increases. Fluorescence peaks (horizontal lines) can also be noted, due to the absorption of CZT X_K-rays in the volume below the pixel which are produced by ionised atoms in the volume below the guard ring. Experimental spectra have been re-binned on the energy vectors of $\mathbf{R}$.

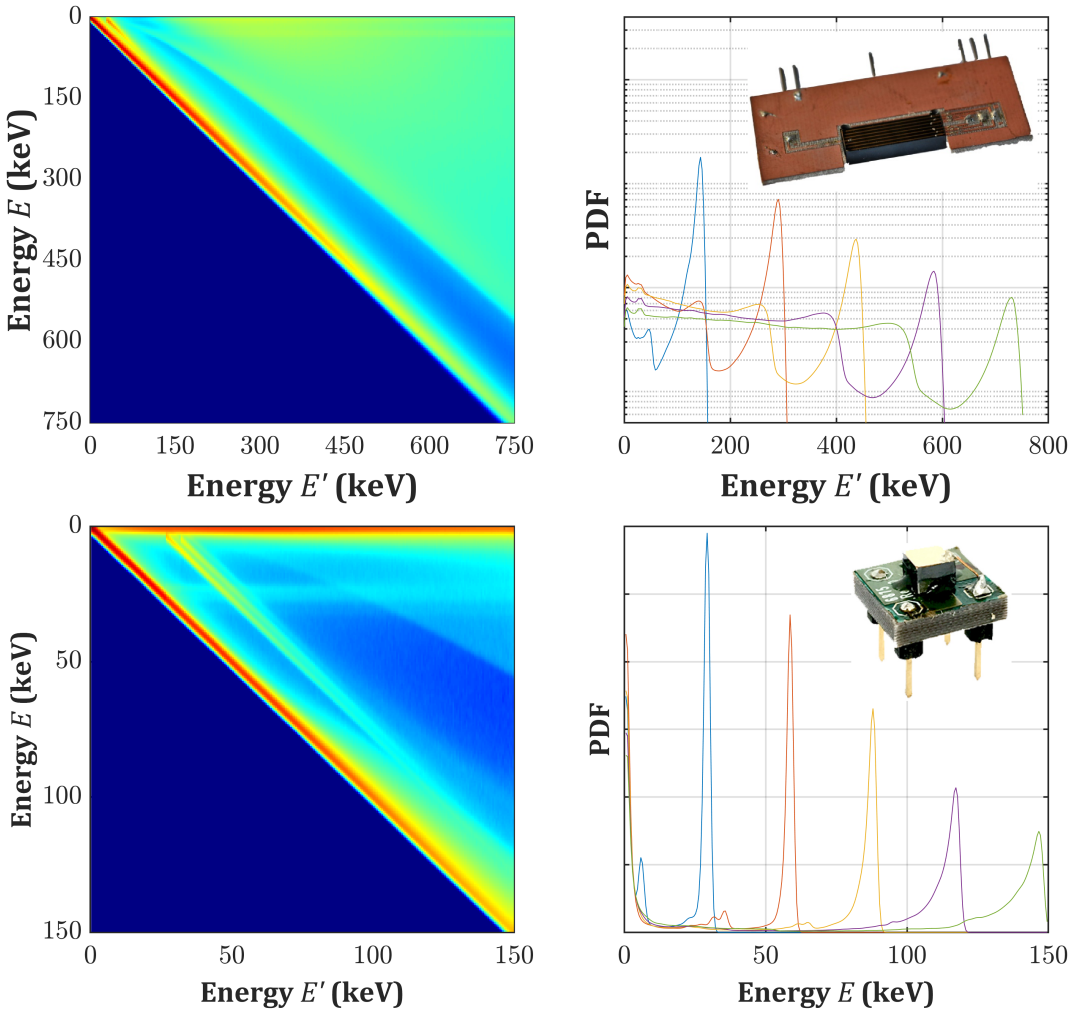

Figure 4.7: Response matrices on a logarithmic false color scale (left) and some of their columns as example (right) for the drift strip (top) and single pixel detectors (bottom).

4.4.3 Unfolding

The unfolding of ^{137}Cs, ^{133}Ba, ^{57}Co and ^{241}Am spectra are reported in Figures 4.8, 4.9, 4.10 and 4.11, respectively. The final solution (referred to as unfolded spectrum) is compared to the tabulated intensities for emission of X- and γ-photons in the case of unshielded radioactive sources [86]. In the case of the ^{241}Am spectrum, the intensities of the X_L-emissions are compared to the ones reported in [87] (self-fluorescence of ^{241}Am and scattered bumps are not considered). Tabulated intensities are normalized with respect to the main photopeak. The convolution of the solution with $\mathbf{R}$ (referred to as folded spectrum) is instead compared to the measured spectrum. All spectra are normalised by area to appreciate the increase of the intensities of photopeaks. The best individual in the population after 10^4 generations is considered as the final solution since a greater number would not improve the fitness. Thus, the reported fitness values (Table 4.2) represent the lower achievable ones. In all cases, the unfolding process based on GA successfully removed escape peaks, Compton edges and noise broadening from the measured γ-spectra and the unfolded spectra essentially consists of δ-like peaks.

Regarding the drift strip detector, the relative intensities of the unfolded peaks are in good agreement with the tabulated ones except in the 0-30 keV energy region, probably because of a partial shielding from the detector case, and the folded spectra remarkably match the measurements. However, spiky residuals are still present on the low energy side of photopeaks in the 500-600 keV and in the 200-250 keV energy ranges in Figures 4.8 and 4.9, respectively. This is due to non-idealities in the $\mathbf{R}$ which partially fails to reproduce the correct spectral shape in the region between the photopeak and the Compton edge. Furthermore, the backscattering peaks are still present after the unfolding in the 190-300 keV energy range in Figure 4.8 and in the 120-190 keV energy range in Figure 4.9. The reason relies on the fact that the response matrix was obtained by simulating the interaction of the radiation with a bare CZT crystal. The absence of components in the physical surroundings of the detector (e.g. metallic case, electronic read out) prevented the formation of this feature in the simulated spectra. Thus, the algorithm interprets the backscattering peak as an actual photon source. The overall shape and intensity of the backscattering peaks are indeed preserved in the unfolded spectra (without the noise broadening) because it is not considered as an artifact introduced by the instrument. This could be fixed by simulating the interaction with the whole detection system in the evaluation of $\mathbf{R}$.

Regarding the single pixel detector, the results are slightly worse. As a matter of fact, the simulation tool does not consider the possibility for charge clouds to be collected by multiple electrodes ("charge sharing effect"). This phenomenon occurs when a photon interacts in the volume below the gap between the pixel and the guard ring contacts and the cloud is shared among these two electrodes. The amount of charge collected by the pixel depends on the distance from the pixel edge. The extent of these losses spans from 0 to the full energy of the photon, hence producing residuals in the whole energy range: this is approximately what can be observed in the unfolded spectra in Figure 4.10 and 4.11.

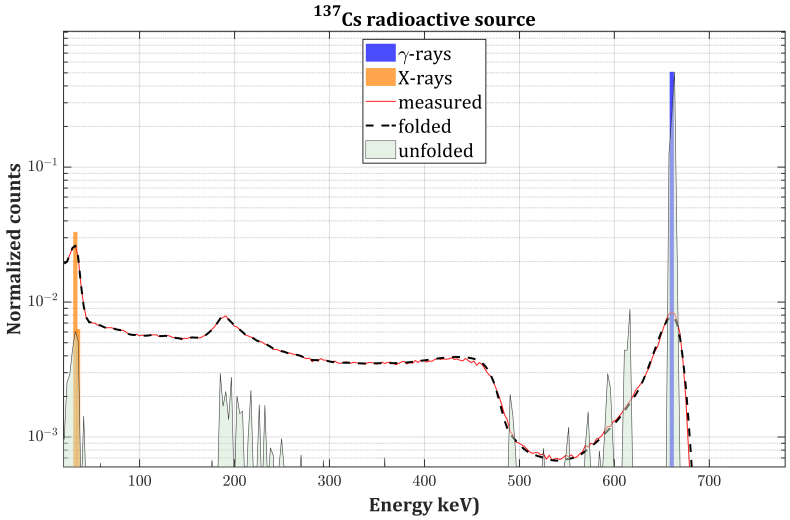

Figure 4.8: ^{137}Cs unfolded spectrum (gray curve) compared to the measured spectrum (red curve), the folded spectrum (black dashed curve) and the tabulated intensities of the γ-emissions (blue bars) and X-emissions (orange bars) of ^{137}Cs on a logarithmic scale.

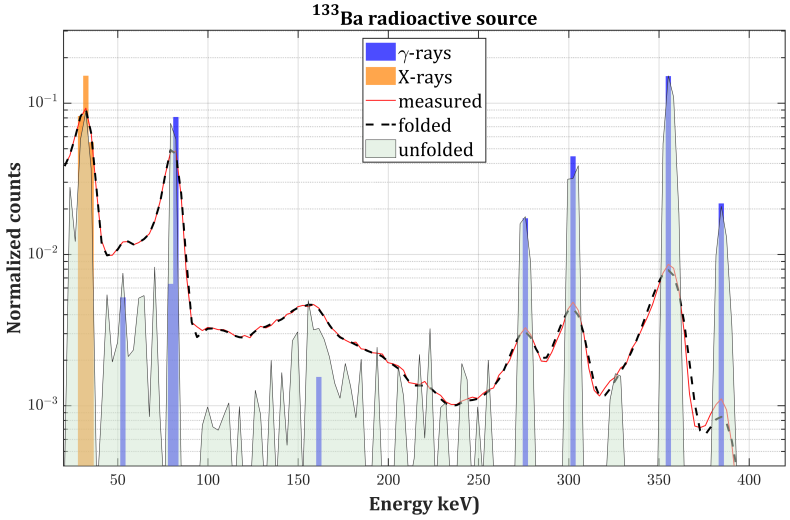

Figure 4.9: ^{133}Ba unfolded spectrum (gray curve) compared to the measured spectrum (red curve), the folded spectrum (black dashed curve) and the tabulated intensities of the γ-emissions (blue bars) and X-emissions (orange bars) of ^{133}Ba on a logarithmic scale.

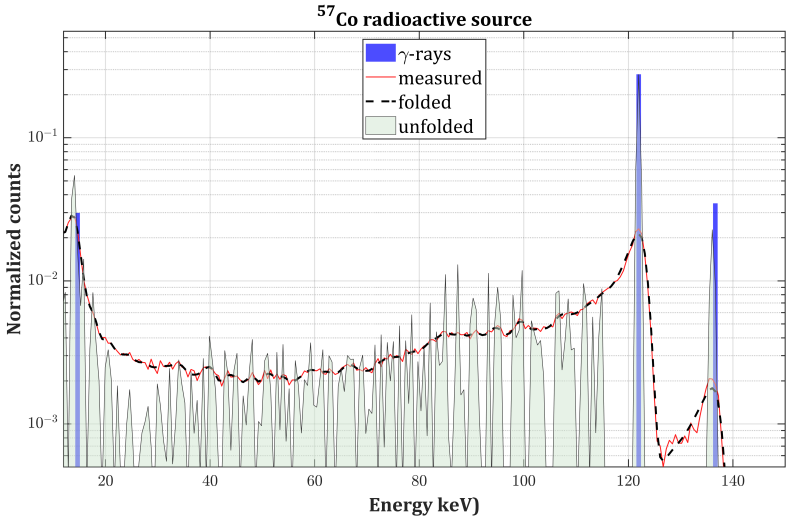

Figure 4.10: ^{57}Co unfolded spectrum (gray curve) compared to the measured spectrum (red curve), the folded spectrum (black dashed curve) and the tabulated intensities of the γ-emissions (blue bars) of ^{57}Co on a logarithmic scale.

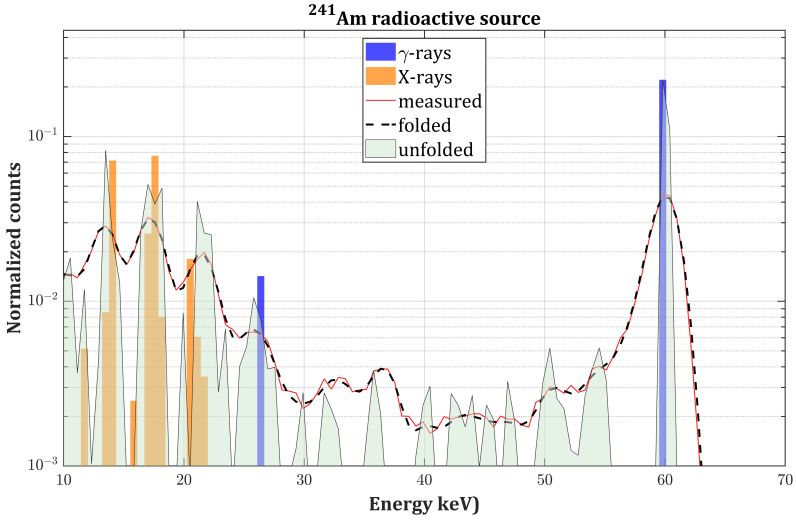

Figure 4.11: ^{241}Am unfolded spectrum (gray curve) compared to the measured spectrum (red curve), the folded spectrum (black dashed curve) and the tabulated intensities of the γ-emissions (blue bars) and X-emissions (orange bars) of ^{241}Am on a logarithmic scale.

Isotope	Detector	fitness
^{137}Cs	Drift strips	1.4×10^{-8}
^{133}Ba	Drift strips	9.1×10^{-8}
^{57}Co	Single pixel	7.6×10^{-8}
^{241}Am	Single pixel	10.0×10^{-8}

Table 4.2: Fitness values for each deconvoluted spectra after 10^4 generations.

Seeding genetic algorithm

These results have been obtained with a random initialisation but the algorithm is able to reproducibly find the best approximate solution provided that a sufficient number of generations has passed, as shown in Figure 4.12. This is indeed a peculiarity of GAs: if the random component (selection, crossover and mutation) is correctly calibrated, local minima do not represent an obstacle.

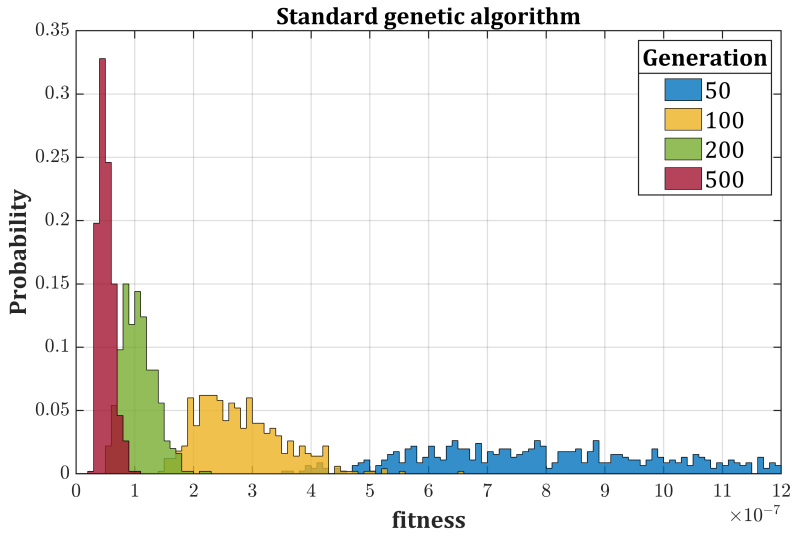

Figure 4.12: PDF of the fitness for the best individual as a function of the number of iterations for the standard GA (^{137}Cs spectrum - 500 runs each).

However, at the beginning the convergence speed is low. The reason relies on the fact that the GA starts from a completely random situation and the first few hundreds of iterations are required just to find good candidate solutions, which are later refined. In the first generations the crossover is less effective since randomly generated individuals are combined, thus obtaining nearly equivalent solutions. An actual improvement can be achieved only when the right genes are mutated (i.e. when peaks start appearing): this indicates that the main leading operation is mutation whose extent, however, is quite limited. Mutating a larger number of genes would indeed stimulate the generation of better candidate solutions but this would be detrimental in the second part

where, on the contrary, it would degrade new individuals. A possible solution consists in using variable mutation parameters P_m and m which decrease as the average fitness improves (adaptive GA) but it would be difficult to finely tune P_m and m in combination with the other parameters to obtain the best overall performances. Instead, a smart initialisation of the population can be performed by exploiting the information contained in the measured spectra. This procedure is referred to as "seeding" and it consists in inserting suitable guesses in the first generation to direct the algorithm on the right path from the beginning. As a matter of fact, the observed spectrum still preserves features of the true incident radiation (e.g., photopeaks) and it would definitely represent a valid guess but a better candidate can actually be obtained by applying the folding iterative method described in [51]:

$$S^{n+1} = (S' \oslash (\mathbf{R} \cdot S^n)) \circ S^n \quad \text{with} \quad S^0 = S' \tag{4.10}$$

where S^n and S^{n+1} are partially unfolded spectra after n and $n+1$ iterations, respectively ($\oslash$ and $\circ$ denote the element-wise division and multiplication, respectively). Figure 4.13 shows that 5 iterations are sufficient to greatly reduce Compton edges and to emphasize peaks. Inserting only one partially unfolded individual in the initial population ($fitness \sim 5 \times 10^{-7}$) is enough because the crossover (Equation 4.9) and the elitist selection facilitate a fast diffusion of the strong genes among the whole population. In this way, the crossover is extremely effective since the beginning and I achieved the goal of guiding the algorithm without excessively restricting the search process (Figure 4.14). The comparison of the performances is summarised in Table 4.3.

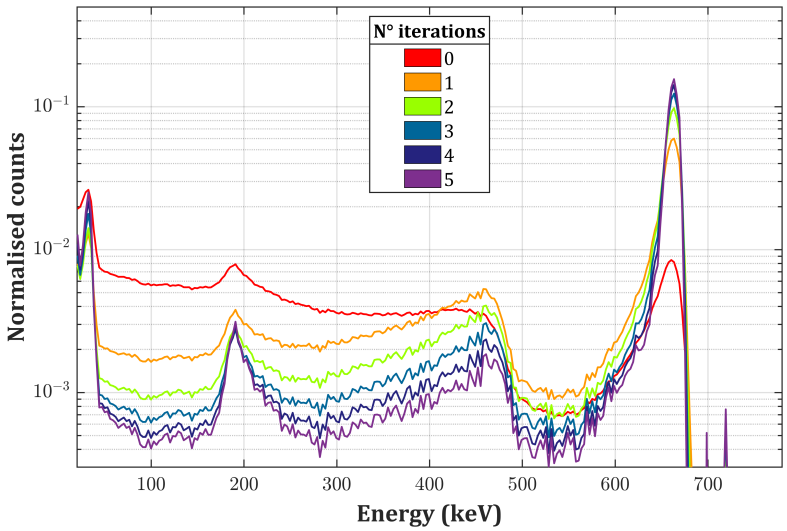

Figure 4.13: Partial unfolded ^{137}Cs spectrum with the folding iterative method as a function of the number of iterations.

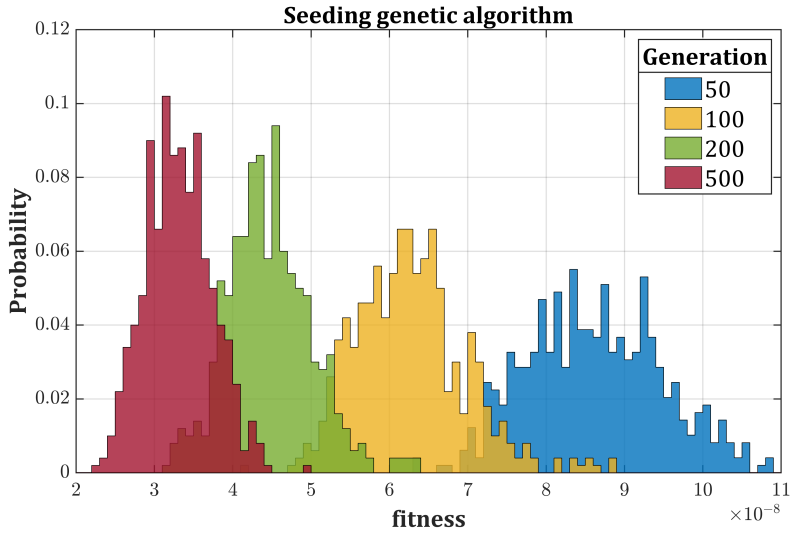

Figure 4.14: PDF of the fitness for the best individual as a function of the number of iterations for the boosted GA (^{137}Cs spectrum - 500 runs each).

STANDARD GA			SEEDING GA		
N° of generations	**fitness**$\times 10^8$	**Av. running time (ms)**	**N° of generations**	**fitness**$\times 10^8$	**Av. running time (ms)**
50	83 ± 25	84	50	8.6 ± 1.0	85
100	27 ± 7	157	100	6.2 ± 0.7	158
200	9.7 ± 2.8	313	200	4.4 ± 0.5	316
500	4.1 ± 1.3	780	500	3.2 ± 0.4	785

Table 4.3: Performances at different iterations (500 runs each) for standard and seeding GA.

Robustness

If statistical fluctuations in each channel are negligible, as is the case of the spectra previously reported, unfolding is a relatively simple task. As a matter of fact, the main criticality is dealing with noise, especially in spectral regions where fluctuations are comparable to the signal. Therefore, the proposed algorithm has been tested on spectra with a lower number of counts in order to prove its robustness: 1.6×10^4 in respect to 1.86×10^6 for the ^{137}Cs source; 2.3×10^4 in respect to 1.6×10^6 for the ^{133}Ba source. As shown in Figures 4.15 and 4.16, GA is still able to find solutions which match the measured spectra but the most important aspect is that those solutions are consistent with the tabulated intensities, although, obviously, with a slightly worse agreement. The final fitness values are 34.3×10^{-8} and 19.3×10^{-8} for ^{137}Cs and ^{133}Ba, respectively.

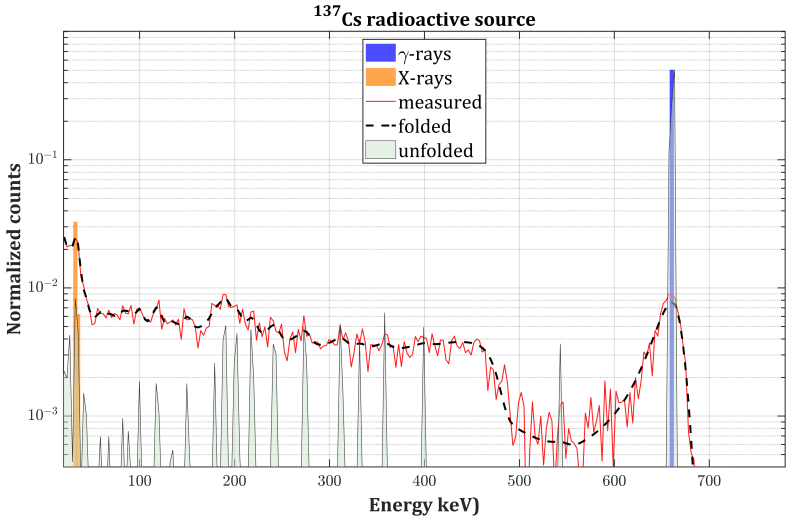

Figure 4.15: ^{137}Cs unfolded spectrum (gray curve) compared to the measured spectrum (red curve), the folded spectrum (black dashed curve) and the tabulated intensities of the γ-emissions (blue bars) and X-emissions (orange bars) of ^{137}Cs on a logarithmic scale.

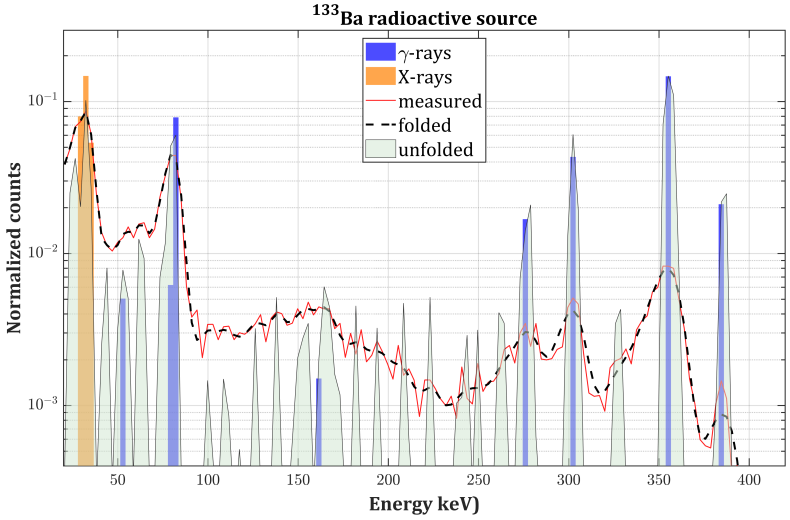

Figure 4.16: ^{133}Ba unfolded spectrum (gray curve) compared to the measured spectrum (red curve), the folded spectrum (black dashed curve) and the tabulated intensities of the γ-emissions (blue bars) and X-emissions (orange bars) of ^{133}Ba on a logarithmic scale.

4.5 Conclusions

In this chapter, a method to unfold γ-spectra based on GA is presented and experimentally validated on spectra of four radionuclides measured with two different CZT-based detectors. This approach effectively takes advantage of all the counts present in the observed spectra to reconstruct and enhance even the weakest photopeaks. Primarily, this is possible thanks to the simulation tool used to produce the spectral response function whose accuracy is confirmed by these results. The simplicity of the GA operations ensures low computation and high speed and allows to quickly find the best approximate solution within the limits of the accuracy of $\mathbf{R}$. The problem of inverting $\mathbf{R}$ is bypassed because it is always used directly to fold new potential solutions, hence avoiding the need of regularisations. The extent of oscillations is limited by the arithmetic recombination performed in the crossover process which average noise and excessive mutations of the parents. The metaheuristic procedure performed by GA allows us to speed up the solution search compared to Monte Carlo approaches. Simultaneously, the random component permits a better exploration of the solution space with respect to other iterative and predetermined methods where, given a certain input, the algorithm always converges to the same output. The strength of GA is indeed combining these two aspects. The stochastic optimization is fast even without prior assumptions but exploiting the physical information contained in the measurements allows to further accelerate the search process. Finally, the algorithm has been successfully applied on spectra with low statistics without the need for a smoothing process.

This method is not dependent on the radiation source and, potentially, it can be applied also on continuous energy distribution (e.g., X-ray spectra). Studies are ongoing to consider the charge sharing effect in the simulation of $\mathbf{R}$ in order to test the algorithm on spectra acquired by pixelated detectors. Finally, this approach can be extended to different classes of radiation devices like scintillation detectors which are widely used in several contexts thanks to lower production costs. However, the energy resolution is usually low in commercial devices ($FWHM \gtrsim 7\%$ @ 662 keV) and the use of a robust analysis algorithm is even more relevant.

Chapter 5

Radioisotope recognition using convolutional neural networks

The identification and, above all, the quantification of the radioisotopes present in a γ-spectrum is a task still heavily affected by errors. The major obstacle is represented by the low energy resolution of devices typically used in fields other than scientific research where detection speed, cost-effectiveness and system portability are of primary concern (industry, environmental monitoring, security and safety). Furthermore, in many practical cases the early identification when statistical fluctuations are dominant is mandatory. This impedes the application of methods based on the spectral shape (peak searching, template matching, regions of interest, spectral unfolding) and usually human intervention is required to obtain reliable results. In a certain sense, humans outclass machines in some tasks: the experience and capacity of abstraction of a trained spectroscopist enable him/her to recognize the relevant information present in a measurement and to guide an algorithm on the right path, hence minimizing identification errors and false positives. This is the reason why algorithms mimicking human mental processes have been introduced in this field, especially in the last decade. In addition, in machine learning approaches the intensive computational workloads is shifted to the training phase in which a predictive model is synthesised, hence allowing fast routine analysis on new data [88, 89].

Firstly, this chapter gives an overview of the main approaches in radioisotope recognition and it describes which role artificial neural networks have in this context. Then, a novel approach based on multi-objective densely connected convolutional neural network is presented. The potentialities of this algorithm are demonstrated on simulated spectra of a CZT-based detector.

5.1 Problems and challenges

I start by explaining the difference between radioisotope identification and quantification. The former consists in identifying the isotopic fingerprints in the measurements (e.g., position of photopeaks) and in determining which isotopes are present and which are absent; this process is referred to as "classification" in data science jargon. The latter consists in estimating the isotopic composition of the measured spectrum (e.g., not only position but also area of photopeaks) and it is a more challenging task, obviously; this process is referred to as "regression" in data science jargon. It is important to clarify these concepts before proceeding further because in one case we obtain a label and in the other case we obtain a numerical value.

Mathematically, a γ-spectrum generated by multiple radioisotopes can be considered as a linear combination of the spectra of each radiation source. Let N denotes the number of channels the measured spectrum is divided into and M the total number of possibly present isotopes, the measured spectrum can be expressed as

$$\vec{c} = \mathbf{R} \cdot \vec{a} \quad \text{or} \quad c_i = \sum_{j=1}^{M} R_{ij} a_j \quad \text{with} \quad i = 1, \ldots, N \tag{5.1}$$

where $\vec{c} = [c_1, \ldots, c_i, \ldots, c_N]^T$ is the vector containing the number of counts in each channel, $\vec{a} = [a_1, \ldots, a_j, \ldots, a_M]^T$ is the isotopic composition vector and $\mathbf{R}$ is the response matrix which is characteristics of the considered detection system. The j-th column of $\mathbf{R}$ represents the ideal measured spectrum of the j-th isotope in which the source-detector geometry is assumed to be always the same and non-linear effects such as pileup are also not considered. Generally, these assumptions hold for CZT-based detectors where the irradiation direction is known and the involved radiation fluxes are low in respect to the dead time of the system. The number of channels in raw spectra is approximately of a few thousands. On the other hand, the complete isotope library has approximately 200 radio-isotopes but this number can be decreased: depending on the specific application (e.g., industrial, medical, security, nuclear energy), the list of possible isotope is usually known which allows to focus the search on a given subspace ($M \approx 20$–30) [90]. The problem is complicated further due to several unknown factors such as the distance and the shielding. As a matter of fact, attenuation is one of the most troublesome aspects because the presence of absorbers modifies the spectral shape. In this case, the response matrix is rewritten as

$$\begin{gathered} \mathbf{R} \longrightarrow \mathbf{R}(\mu) \\ R_{ij} \longrightarrow R_{ij} \cdot \exp\left\{ -\sum_{z} \mu_z(i) t_z \right\} \end{gathered} \tag{5.2}$$

where $\mu_z(i)$ is the attenuation coefficient at the i-th channel for the z-th absorber (e.g., steel, lead). The isotopic weights can be calculated starting from the number of counts in each energy channel by inverting Equation 5.1. However, the inversion of $\mathbf{R}$

is arduous, analogously to the case of spectral unfolding: distortions, fluctuations and uncertainties may lead to erroneous and unphysical results as explained in the previous chapter. Another possible way is not inverting **R** but, instead, fitting its inverse using experimental spectra whose isotopic composition is known (least-squares method).

Various approaches have been proposed to solve either the classification or regression problem and most of them can be gathered in two main categories: peak search and match and template matching [91]. In the former, after a proper smoothing step and the removal of background, the peaks are identified and analysed. This process is not trivial in case of spectra with a low number of events and with low/average energy resolution since statistical fluctuations and broad peaks may prevent distinguishing a small signal from noise. Then, numerical attributes/features are calculated (e.g., peaks area). The quality and the number of features as well as the dimensions of the library are crucial in order to carry out the subsequent classification step since speed and accuracy are competing factors. These features are used to select the correct solution in a library of nuclear data through comparison. Several classification algorithms exist (decision trees, neural networks, Naïve Bayes, Nearest Neighbour, Support vector machines) and the choice of the best one depends on the previous phases. The latter method consists in building a library of isotope spectra in different configurations which must be characteristic of the detection system used for the measurements. An algorithm searches for the best linear combination of solutions present in the library which best matches the measured spectrum. Since this combinatorial problem can be complex, a previous step must reduce the dimensionality of data and remove noise and distortions which could mislead the comparison. Also in this case, many algorithms can be used and they can be divided into heuristic and systematic. Both methods are analogous in the sense that, firstly, the raw measurement is pre-processed to reduce the extent of noise and/or the dimensionality of data, although this passage is also intrinsically accompanied by information losses. Secondly, the extracted features are used to perform the classification or regression (Figure 5.1). Therefore, determining the isotopic composition in a γ-spectrum is generally a multi-step process. The algorithms can be fully automated or can require the intervention of a trained spectroscopist to assist and guide them in the most delicate steps.

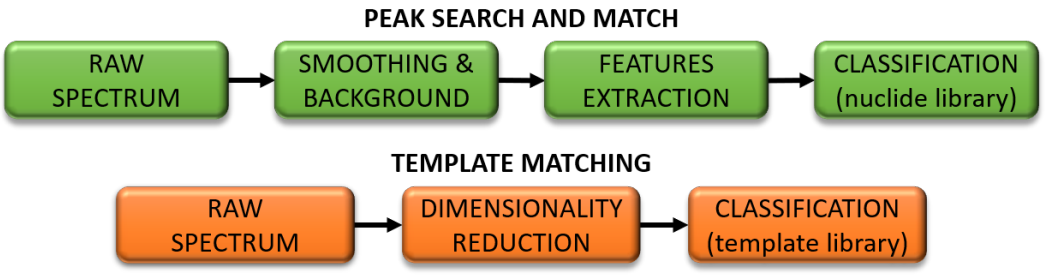

Figure 5.1: Flowchart of the "peak search and match" and "template matching" methods for radioisotope recognition in γ-spectra.

5.2 Role of artificial neural networks

Ideally, the algorithm should satisfy the following requirements:

- it should be fully automated;
- the response should be fast in respect to the time required to acquire the spectrum
- it should process directly the raw spectrum without intermediate steps
- it should be robust in respect to noise and distortions
- the training phase should be simple in term of speed and calculations
- it should search for both local and global patterns to efficiently extract the relevant features

An additional requirement is performing both identification and quantification. The reason why both operations are necessary is the instability of the inverse problem (Equation 5.1): the weights should be estimated only for the radionuclides actually present and not for the absent ones. In summary, the ideal output should consists of a normalised vector of non-negative values (one for each possible isotope). Thus, the ideal algorithm should perform both a multi-label classification (i.e., each isotope could be either present or absent) and a regression of the isotopic fractions. Recently, artificial neural network-based algorithms (ANN) appeared in this context both in scientific articles [89, 92, 93, 94, 95] and in patents [96, 97, 98]. The purpose of ANN is replacing one or all the steps reported in Figure 5.1 and satisfying, partially or entirely, the aforementioned requirements thanks to their peculiarities. Firstly, the comparison with a library is not performed for each new measurement; instead, the computational time is moved to the training phase. After, the process is completely automated and the response is practically immediate. Secondly, it is possible to design the net to directly analyse the raw measurement and to provide the desired results as output. That being said, the generalization ability is definitely the primary strength of ANN. However, raw spectra are usually composed of a few thousands of channels and it could be difficult to train a network with such a large number of input parameters [95]. For example, the architecture proposed by Kamuda *et al.* presents $\approx 10^6$ parameters for spectra with 1024 channels [92, 94]. For this reason, a preliminary step of dimensionality reduction is usually adopted [89, 93]. Moreover, ANN considers the raw spectra as a whole: this leads to a large number of learnable parameters because the network does not exploit the spatial relations among channels. In contrast, Convolutional Neural Networks (CNN), mainly used for image recognition purposes, are characterised by two aspects which allows to overcome these problems: parameter sharing and local connectivity. Regarding the f ormer, CNN applies convolutional kernels or filters, whose weights are adjusted during training, to the input image in each layer. Therefore, the number of parameters does not depend on the image size and it is usually far less than the number

of pixels of the input image. This allows to greatly reduce the number of learnable parameters since the same kernels operate on the whole image. Moreover, with the same number of parameters, it is possible to realize deeper networks, hence obtaining better abstraction reasoning. Regarding the latter, the kernels are connected only to a fraction of the pixels of the input image. Each portion is processed separately resulting in an effective translation-invariant extraction of local patterns. Therefore, in contrast to standard ANN, CNN effectively exploits spatial relations among pixels and extracts the so-called features maps. These are then passed to fully connected layers which instead search for global relations among all the input data. As a matter of fact, CNN belongs to the deep learning family in which the features extraction is automatically optimised by the network itself on the basis of the final classification/regression step. Precisely for these reasons, CNNs are widely used for visual object recognition thanks to the ability to effectively recognize patterns (shapes, contours, colours, etc..) independently from slight distortions, translations or transformations.

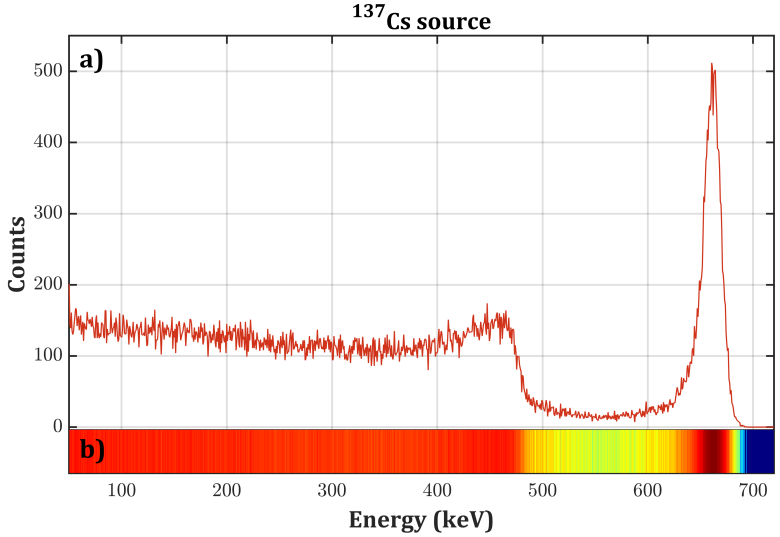

Figure 5.2: Example of a simulated γ-spectrum of a ^{137}Cs source **(a)** and its 1-D representation on a color scale **(b)**.

In this framework, a γ-spectrum can indeed be considered as a one-dimensional image where each channel corresponds to a pixel (Figure 5.2). Photopeaks, Compton edges and Compton continua act as features which univocally determines the radioisotope that has generated it and they can be detected by moving a proper filter along the γ-spectrum, independently on where they are located. In summary, CNN allows a robust features extraction directly on the raw spectrum without information losses using few parameters. Admittedly, CNN mimics the actions performed by other methods, as shown in the flowchart reported in Figure 5.3. This approach has already been proposed by Liang *et al.*, although in that case the network requires a preliminary data preparation (2D mapping) and it was designed to only perform the identification [95].

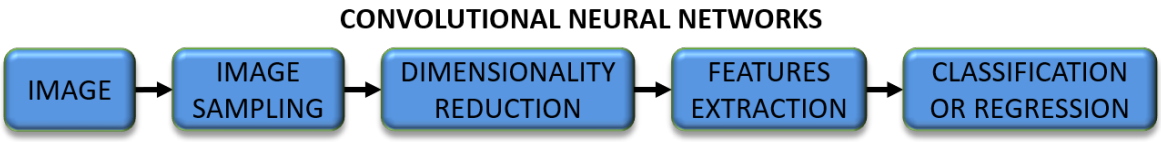

Figure 5.3: Flowchart of a generic convolutional neural network.

Lastly, the remaining unsolved problem is that neural networks can solve either classification or regression problems: independently from the criteria used for features extraction, the last step always consists in two or more fully connected layers both in ANN and CNN. A classic multi-layer architecture can only perform classification because non-linear activation functions prevent the net to conceive the input as a superimposition of spectra of single isotopes [92, 94]. On the other hand, pure linear neural networks can be tentatively used for regression: in this case the network would consist in just an input and an output layer with N and M neurons, respectively, and no activation functions (Figure 5.4). If we use spectra whose isotopic composition is known, we can adjust the weights connecting these two layers in order to produce the desired vector of weights given a certain input spectrum according to

$$a_j = W_{ji} c_i \quad \text{with} \quad i = 1, \ldots, N \quad \text{and} \quad j = 1, \ldots, M \tag{5.3}$$

The network linearly combines the number of counts in each channel to calculate the isotopic weights. However, the lack of non-linearities impedes to satisfy the universal approximation theorem by which the network can approximate any function (the number of learnable parameters is fixed to the $N \times M$ product and additional layers would be redundant in pure linear NN). Additionally, constraints cannot be applied to the output of a linear neural network. As a matter of fact, Equation 5.3 is exactly the inverse of Equation 5.1 and the weights W_{ji} represent the elements of the inverse of $\mathbf{R}$, hence the approach would be equivalent to a least-squares fitting [89].

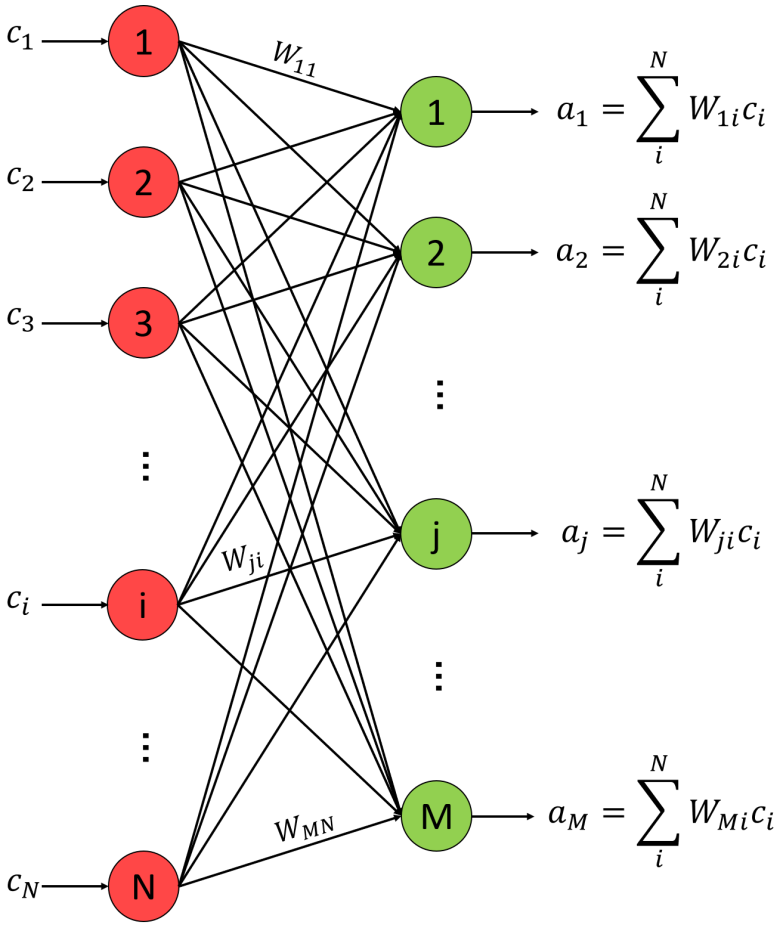

Figure 5.4: Architecture of a linear neural network with N and M neurons in the input and output layers, respectively. The network calculates the isotopic composition by linearly combining the number of counts in the measured spectrum.

5.3 Proposed method

5.3.1 Final architecture

In the previous section, the essential ingredients to perform features extraction, identification and quantification of radioisotopes with neural networks are described. As already mentioned, the problem is twofold. Nevertheless, doing both classification and regression is possible by using multi-objective neural networks where, during training, the same parameters are adjusted to accomplish two different predictions. The network forks after the features extraction and assigning a different task to each branch. The final architecture, obtained after several trials and errors, is here described in detail for a library of eight radioisotopes (the reason for this number is explained later) and it is shown in Figure 5.5.

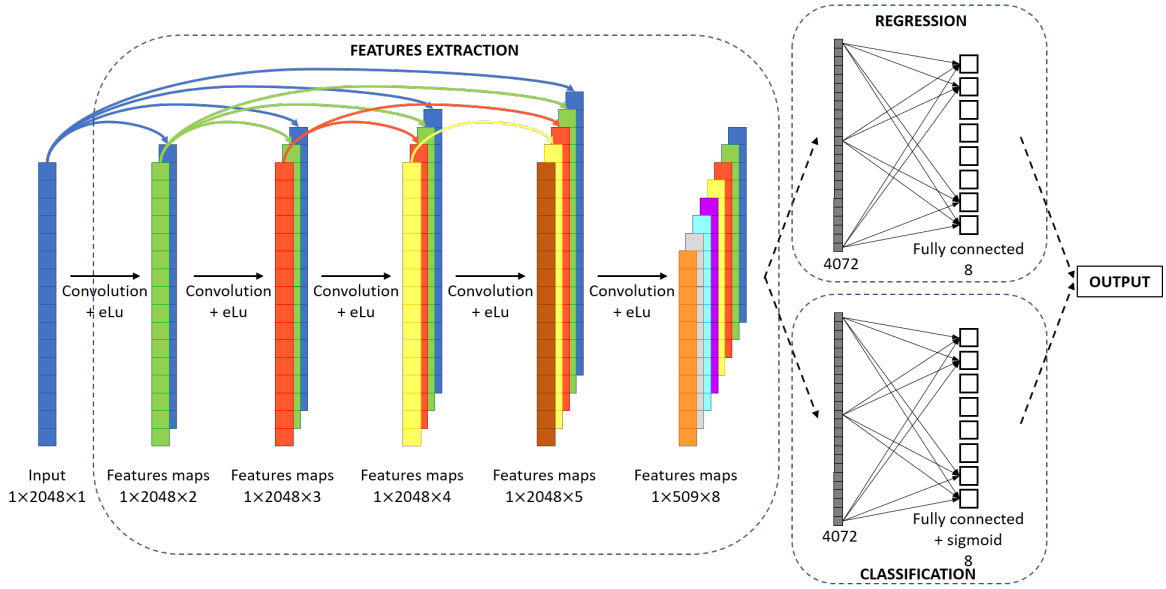

Figure 5.5: Architecture of the multi-objective densely-connected convolutional neural network used for radioisotope identification and quantification. The task of each block is indicated.

The input consists in a vector of 2048 elements which corresponds to the raw spectrum normalised by the total number of counts. The "Features extraction" part presents five convolutional blocks of which the first four are Densely Connected (DC) that is the output of each block is the input of all the subsequent ones [99]. The main limit in deep networks is information flow through the various layers because the weights of the first layers are the last ones to be updated during training (back-propagation). Since the update is based on the partial derivative of the loss function (i.e., the quantity that we want to minimise during training) the presence of several layers leads to the so-called "vanishing gradient problem" which could slow or even stop the network from learning (i.e., the values of weights do not change). In DC-CNN

the gradient flows directly from later layers to the earlier ones. Although the total number of connections increases, DC-CNN requires less parameters and promotes feature propagation since each block has access to the features maps extracted by all the previous ones. This leads to a more short and compact training with less overfitting issues. Coming back to the architecture of this work, the first block applies a 1×24 filter to the raw spectrum, at the end of which 23 zeros are added in such a way to give a vector of the same size after the convolution ("zero padding"). The filter size is related to the spatial extent (in this case, the energetic extent) of the features present in the γ-spectrum and to the noise levels. On one hand, the receptive field of the filter should not be too large to be able to catch details which may be relevant later. On the other hand, high statistical fluctuations must not be mistaken as features and a large filter helps in catching the overall trend in the considered spectral portion. Here, the filter considers 24 channels at a time, which is a relatively high number, because the network is conceived to be applied in γ-spectra with low statistics.

Subsequently, data are re-scaled and re-centred through a batch normalisation process [100]. This technique addresses the "internal covariate shift" and makes the network less sensitive to parameter initialisation. After, the Exponential Linear Unit function (ELU) is applied to each element of the feature map and the output is passed to the next block. Among the various activation functions, ELU demonstrated to produce better results in deep networks [101]. The reasons of the absence of the typical pooling step after the activation function, commonly used in CNN used to reduce the amount of data, are two: firstly, the features maps size must not vary in DC-CNN; secondly, equally good results can be obtained without pooling ("all convolutional neural networks" [102]). The same operations are executed in the subsequent three blocks, except the filter size because each block operates on a different number of stacked features maps ($1 \times 2048 \times 2$, $1 \times 2048 \times 3$, $1 \times 2048 \times 4$ e $1 \times 2048 \times 5$) but the output is always a 1×2048 vector. The last convolutional block condenses the information before the classification/regression step producing 8 features maps with 1×509 elements for a total of 4072. This block also prevents the raw spectrum, not processed and largely affected by noise, to be transferred to the subsequent fully connected layers. As a matter of fact, the extent of distortions is reduced at this stage: an example of the features maps extracted in each step are shown in Figures 5.6 and 5.7 in the case of a ^{137}Cs source. Basically, the network removes noise, enhances photopeaks and other features just as other methods.

At this point, the network forks and the same information are processed by two distinct fully connected layers: one for the regression and one for the classification. The regression branch is necessarily structured according to what described before: the output data of the convolutional part are linearly combined to produce a coefficient for each isotope. This is the only structure which allows to conceive input data as superimposition of separate contributions. The classification branch presents the same structure but, instead, a sigmoidal activation function is applied to the output of the fully connected layer: each neuron produces the probability that a certain isotope is present in the [0,1] range. Practically, the same information is elaborated by two

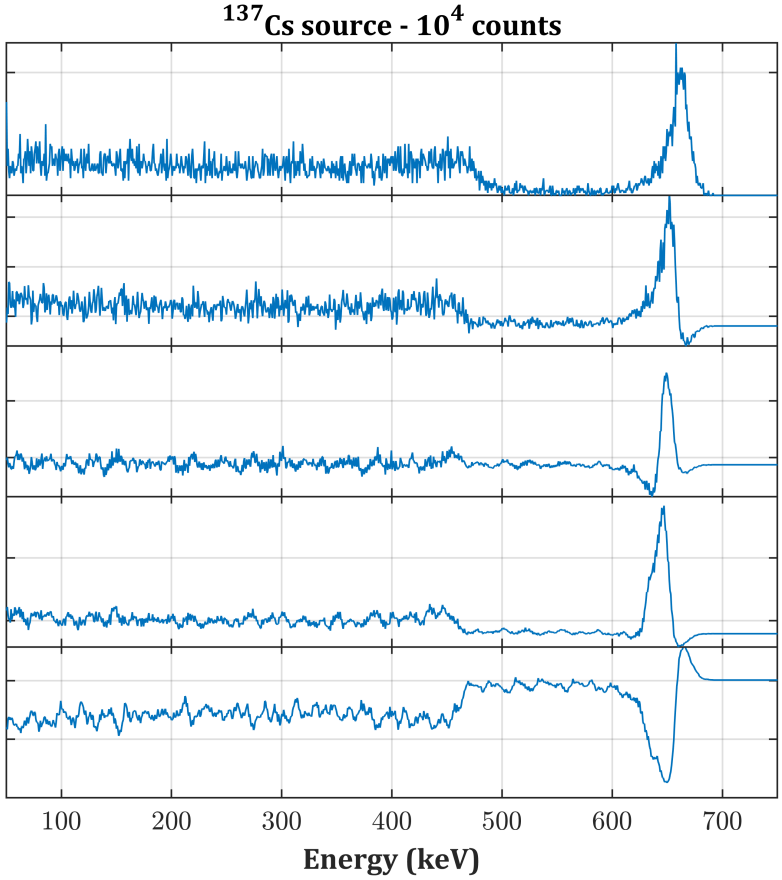

Figure 5.6: Raw spectrum (top) and the corresponding features maps extracted by the first four convolutional blocks of the network in the case of ^{137}Cs source with 10^4 events.

different nets which gives, for each isotope, two values related the probability of its presence and the estimated fraction. The final output is then processed by imposing a threshold above which an isotope is considered to be present; the weights of the absent ones are discarded and the rest is normalised. Therefore, the final output consists of a normalised vector of 8 isotopic weights.

Basically, it is necessary to resort to the architecture of directed acyclic graphs to realise both a DC-CNN and a multi-objective network: each layer can be connected to one or more subsequent layers, preserving a topological ordering. The total number of learnable parameters of this network (66084) is extremely limited if we consider that a simple linear neural network for spectra with 2048 channels and 8 possible isotopes is $2048 \times 8 = 16384$. This leads to several advantages in terms of training speed and the size of the dataset required for training. However, it should be emphasised that this must not be considered as definitive: a different number of convolutional blocks with filters with different sizes can lead to good results anyway. The efficacy of the algorithm lies in the combination of the fundamental building blocks and not in the hyper-parameters (i.e., the parameters related to the architecture, not the ones used

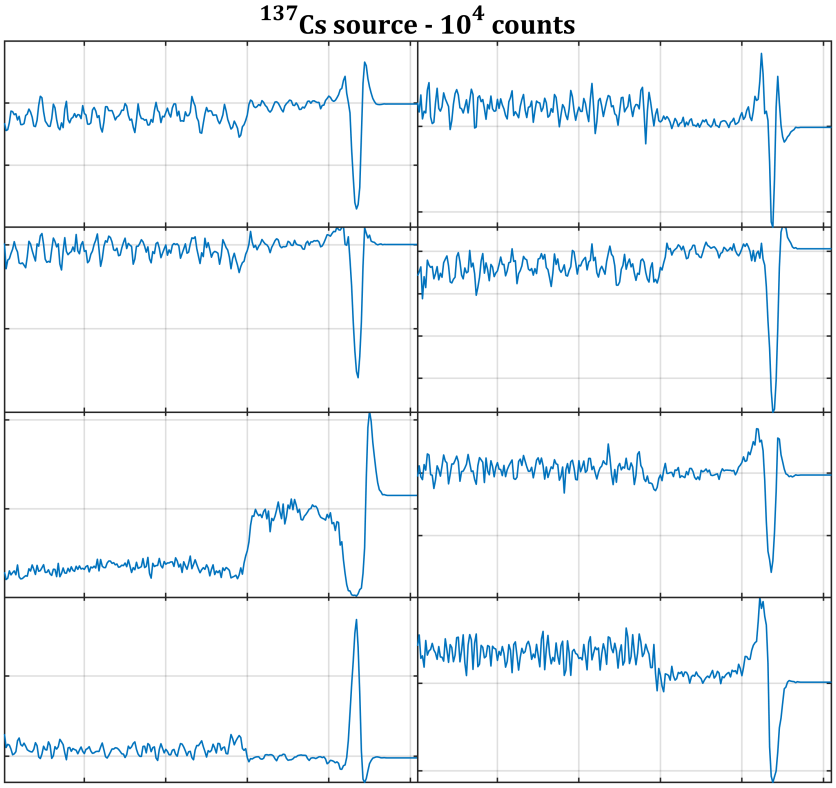

Figure 5.7: Features maps extracted by the final convolutional block of the network in the case of ^{137}Cs source with 10^4 events.

for the prediction). Nevertheless, I obtained the best results with this architecture.

5.3.2 Training

The first validation of this method has been performed with experimental spectra of a $1.0 \times 1.0 \times 0.5$ cm^3 CZT-based quasi-hemispherical detector with an energy resolution of 3% $FWHM$ @662 keV. However, only four radioactive sources were at disposal in my institute (^{241}Am, ^{57}Co, ^{133}Ba and ^{137}Cs) and we moved to synthesised spectra to enlarge the isotope library composed of eight radionuclides commonly used in industrial context: ^{57}Co, ^{60}Co, ^{133}Ba, ^{137}Cs, ^{192}Ir, ^{204}Tl, ^{226}Ra and ^{241}Am. This is the most simple dataset whose γ-emissions span from 60 to 1332 keV. I used the simulation tool described in Chapter 4 to produce the response matrix of the same quasi-hemispherical detector used for the first validation so it will be possible to test the method on a real device in the future. In the simulation, radioactive sources are unshielded and the crystal is irradiated from the cathode. The source has the same dimension of the cathode (1.0×1.0 cm^2) and photons are emitted orthogonally to reproduce a distant source. The spectra for each isotope are reported in Figure 5.8. These were used as generating functions of spectra with an arbitrary number of counts.

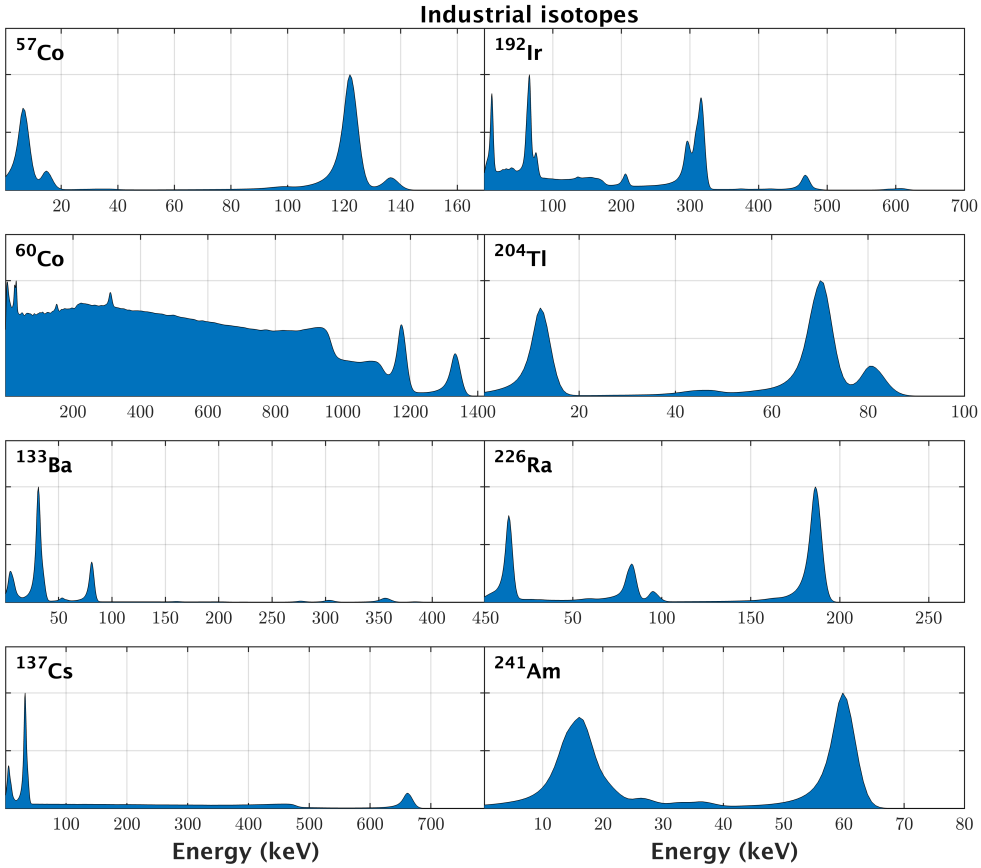

Figure 5.8: Generating functions (normalised spectra) of the industrial radioisotope library used for the validation.

The dataset is composed of the following classes for a total of 19320 spectra:

- single radioisotope with 10^3, 10^4 and 10^5 counts $(8(100 + 100 + 10) = 1680)$;
- two radioisotopes in a 1:1 ratio with 2×10^3, 2×10^4 and 2×10^5 counts $(28(100 + 100 + 10) = 5880)$;
- two radioisotopes in a 3:1 ratio and 4×10^3, 4×10^4 and 4×10^5 counts $(28(100 + 100 + 10) = 5880)$;
- two radioisotopes in a 1:3 ratio and 4×10^3, 4×10^4 and 4×10^5 counts $(28(100 + 100 + 10) = 5880)$;

The diversity of the classes has the goal to make the network less sensitive to statistical noise and isotopic composition. The total loss function, or error, that the networks has the goal to minimise is the sum of the loss function of each branch: cross-entropy for the classification part (Loss_C) and root mean square error for the regression part

(Loss_R). The output of the former branch is compared to a vector of 1 and 0 (i.e., "present" and "absent") and the error is calculated according to

$$\text{Loss}_C = -\sum_{o=1}^{M}\sum_{c=1}^{M} y_{o,c}\log p_{o,c} \tag{5.4}$$

where $M = 8$ is the number of classes, o is the index which runs over all the predicted values, c is the index which runs over all the classes labels, $y_{o,c}$ is the target (0 or 1) and $P_{o,c}$ is the predicted probability observation. The output of the latter branch is compared to a normalised vector containing the isotopic composition and the error is calculated according to

$$\text{Loss}_R = \sum_{o=1}^{M}\sum_{c=1}^{M} (y_{o,c} - p_{o,c})^2 \tag{5.5}$$

A loss function values of 0 means that the predictions are always accurate. The dataset has been divided into training set, validation set and test set in a 80:10:10 ratio. The optimisation algorithm used to update the weights is ADAptive Moment estimation algorithm (ADAM) which combines the properties of Stochastic Gradient Descent (SGD) and adaptive momentum [103]. It is commonly used in deep learning applications because, as in this case, it produces the best results. The training set is divided further in mini-batch of 128 spectra, randomly chosen, and the update of the weights is performed for each mini-batch. When the network iterates over all the mini-batches, defined as "epoch", the network is tested on the validation set: if the performances on this set do not improve for five successive epochs, the training stops even if the loss function is still decreasing. This expedient, referred to as "early stopping",avoids overfitting issues by preventing the network to memorise the examples in the training set and to lose generalisation abilities. Finally, the trained net is tested on the test set and the results are reported in the next section. The training is simple and can be performed on standard laptops in a short time (10 epochs in $\approx$ 20 minutes on a single core Intel Pentium CPU 3825U 1.9 GHz. After the training, an isotope is considered present if its classification value exceeds the 0.5 threshold. The other weights are discarded and the remaining ones are normalised. An example of the raw and processed output is reported in Table 5.1.

Table 5.1: Raw output (CL. and REG.) and processed output (PROC.) of the trained net in the case of a ^{137}Cs source with 10^3 counts.

	^{57}Co	^{60}Co	^{133}Ba	^{137}Cs	^{192}Ir	^{204}Tl	^{226}Ra	^{241}Am
CL.	0.0013	0.0051	0.0036	1.0000	0.0036	0.0011	0.0011	0.0052
REG.	0.0023	0.0028	0.0357	0.9575	0.0127	0.0020	-0.0110	-0.0102
PROC.	0	0	0	1	0	0	0	0

5.4 Results

In this section the performances of the trained network are presented. The results on the test set as well as on more complex datasets not used in the training are reported to prove the robustness of the method.

5.4.1 Test set

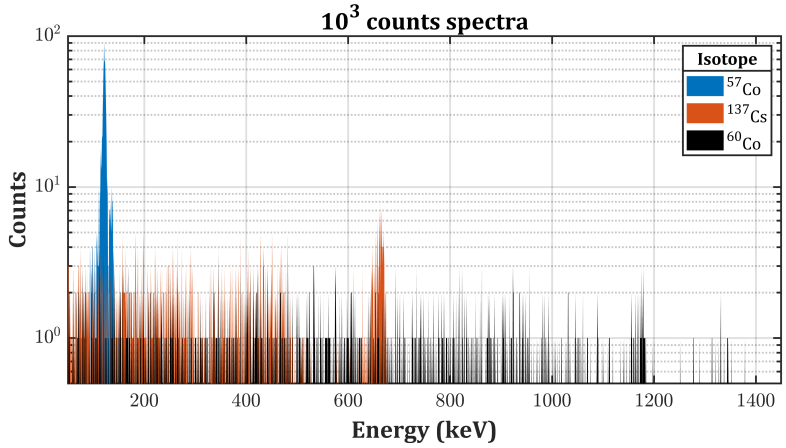

Figure 5.9: Examples of spectra of the test set for ^{57}Co, ^{137}Cs and ^{60}Co sources (10^3 counts).

The confusion matrix of the prediction on the 168 spectra with a single radionuclide (21 each) is reported in Table 5.2: the algorithm demonstrates a 100% accuracy without false positive, despite the low statistics in spectra with 10^3 counts (Figure 5.9). The results for mixed spectra are reported in Tables 5.3, 5.4, and 5.5 for the 1:1, 3:1 and 1:3 ratios, respectively. The network always identifies both radioisotopes with an accurate estimation of the relative fractions.

Table 5.2: Confusion matrix for the spectra of the train set with one isotope.

		ACTUAL CLASS							
PREDICTED CLASS	**Isotope**	**^{57}Co**	**^{60}Co**	**^{133}Ba**	**^{137}Cs**	**^{192}Ir**	**^{204}Tl**	**^{226}Ra**	**^{241}Am**
	^{57}Co	21	0	0	0	0	0	0	0
	^{60}Co	0	21	0	0	0	0	0	0
	^{133}Ba	0	0	21	0	0	0	0	0
	^{137}Cs	0	0	0	21	0	0	0	0
	^{192}Ir	0	0	0	0	21	0	0	0
	^{204}Tl	0	0	0	0	0	21	0	0
	^{226}Ra	0	0	0	0	0	0	21	0
	^{241}Am	0	0	0	0	0	0	0	21

Table 5.3: Predictions (in percentage) on the spectra of the test set with two isotopes in a 1:1 ratio. The results are averaged over all spectra belonging to the same class, regardless of the statistics (2×10^3, 2×10^4 and 2×10^5). Standard deviation is reported in brackets.

Isotopes (1:1)	**^{57}Co**	**^{60}Co**	**^{133}Ba**	**^{137}Cs**	**^{192}Ir**	**^{204}Tl**	**^{226}Ra**	**^{241}Am**
^{57}Co^{+}^{60}Co	50.3(7)	49.7(7)	0	0	0	0	0	0
^{57}Co^{+}^{133}Ba	50.2(7)	0	49.8(7)	0	0	0	0	0
^{57}Co^{+}^{137}Cs	50.5(9)	0	0	49.5(9)	0	0	0	0
^{57}Co^{+}^{192}Ir	50.7(16)	0	0	0	49.3(16)	0	0	0
^{57}Co^{+}^{204}Tl	49.9(7)	0	0	0	0	50.1(7)	0	0
^{57}Co^{+}^{226}Ra	50.1(8)	0	0	0	0	0	49.9(8)	0
^{57}Co^{+}^{241}Am	51.5(9)	0	0	0	0	0	0	48.5(9)
^{60}Co^{+}^{133}Ba	0	49.9(12)	50.1	0	0	0	0	0
^{60}Co^{+}^{137}Cs	0	50.2(9)	0	49.8(9)	0	0	0	0
^{60}Co^{+}^{192}Ir	0	49.9(13)	0	0	50.1(13)	0	0	0
^{60}Co^{+}^{204}Tl	0	50.3(6)	0	0	0	49.7(6)	0	0
^{60}Co^{+}^{226}Ra	0	49.3(7)	0	0	0	0	50.7(7)	0
^{60}Co^{+}^{241}Am	0	51.4(6)	0	0	0	0	0	48.6(6)
^{133}Ba^{+}^{137}Cs	0	0	50.1(19)	49.9(19)	0	0	0	0
^{133}Ba^{+}^{192}Ir	0	0	49.9(17)	0	50.1(17)	0	0	0
^{133}Ba^{+}^{204}Tl	0	0	53.9(9)	0	0	46.1(9)	0	0
^{133}Ba^{+}^{226}Ra	0	0	50.0(12)	0	0	0	50.0(12)	0
^{133}Ba^{+}^{241}Am	0	0	52.3(16)	0	0	0	0	47.7(16)
^{137}Cs^{+}^{192}Ir	0	0	0	49.5(13)	50.5(13)	0	0	0
^{137}Cs^{+}^{204}Tl	0	0	0	50.1(9)	0	49.9(9)	0	0
^{137}Cs^{+}^{226}Ra	0	0	0	49.1(9)	0	0	50.9(9)	0
^{137}Cs^{+}^{241}Am	0	0	0	51.3(8)	0	0	0	48.7(8)
^{192}Ir^{+}^{204}Tl	0	0	0	0	49.9(10)	50.1(10)	0	0
^{192}Ir^{+}^{226}Ra	0	0	0	0	49.0(10)	0	51.0(10)	0
^{192}Ir^{+}^{241}Am	0	0	0	0	49.9(8)	0	0	50.1(8)
^{204}Tl^{+}^{226}Ra	0	0	0	0	0	49.6(9)	50.4(9)	0
^{204}Tl^{+}^{241}Am	0	0	0	0	0	52.4(8)	0	47.6(8)
^{226}Ra^{+}^{241}Am	0	0	0	0	0	0	52.4(9)	47.6(9)

Table 5.4: Predictions (in percentage) on the spectra of the test set with two isotopes in a 3:1 ratio. The results are averaged over all spectra belonging to the same class, regardless of the statistics (4×10^3, 4×10^4 and 4×10^5). Standard deviation is reported in brackets.

Isotopes (3:1)	**^{57}Co**	**^{60}Co**	**^{133}Ba**	**^{137}Cs**	**^{192}Ir**	**^{204}Tl**	**^{226}Ra**	**^{241}Am**
^{57}Co^{+}^{60}Co	74.4(4)	26.6(4)	0	0	0	0	0	0
^{57}Co^{+}^{133}Ba	74.1(12)	0	25.9(12)	0	0	0	0	0
^{57}Co^{+}^{137}Cs	74.6(5)	0	0	25.4(5)	0	0	0	0
^{57}Co^{+}^{192}Ir	75.1(6)	0	0	0	24.9(6)	0	0	0
^{57}Co^{+}^{204}Tl	71.6(6)	0	0	0	0	28.4(6)	0	0
^{57}Co^{+}^{226}Ra	75.8(4)	0	0	0	0	0	24.2(4)	0
^{57}Co^{+}^{241}Am	72.1(5)	0	0	0	0	0	0	27.9(5)
^{60}Co^{+}^{133}Ba	0	73.9(5)	26.1(5)	0	0	0	0	0
^{60}Co^{+}^{137}Cs	0	74.8(5)	0	25.2(5)	0	0	0	0
^{60}Co^{+}^{192}Ir	0	74.1(10)	0	0	25.9(10)	0	0	0
^{60}Co^{+}^{204}Tl	0	72.0(4)	0	0	0	28.0(4)	0	0
^{60}Co^{+}^{226}Ra	0	74.4(5)	0	0	0	0	25.6(5)	0
^{60}Co^{+}^{241}Am	0	73.5(6)	0	0	0	0	0	27.4(6)
^{133}Ba^{+}^{137}Cs	0	0	75.0(6)	25.0(6)	0	0	0	0
^{133}Ba^{+}^{192}Ir	0	0	74.5(9)	0	25.5(9)	0	0	0
^{133}Ba^{+}^{204}Tl	0	0	76.2(9)	0	0	23.8(9)	0	0
^{133}Ba^{+}^{226}Ra	0	0	75.5(7)	0	0	0	24.5(7)	0
^{133}Ba^{+}^{241}Am	0	0	73.5(7)	0	0	0	0	26.5(7)
^{137}Cs^{+}^{192}Ir	0	0	0	73.9(13)	26.1(13)	0	0	0
^{137}Cs^{+}^{204}Tl	0	0	0	72.1(6)	0	27.9(6)	0	0
^{137}Cs^{+}^{226}Ra	0	0	0	73.9(7)	0	0	26.1(7)	0
^{137}Cs^{+}^{241}Am	0	0	0	72.7(7)	0	0	0	27.3(7)
^{192}Ir^{+}^{204}Tl	0	0	0	0	72.6(8)	27.4(8)	0	0
^{192}Ir^{+}^{226}Ra	0	0	0	0	74.9(9)	0	25.1(9)	0
^{192}Ir^{+}^{241}Am	0	0	0	0	70.7(10)	0	0	29.3(10)
^{204}Tl^{+}^{226}Ra	0	0	0	0	0	74.9(6)	25.1(6)	0
^{204}Tl^{+}^{241}Am	0	0	0	0	0	73.1(4)	0	26.9(4)
^{226}Ra^{+}^{241}Am	0	0	0	0	0	0	73.4(7)	26.6(7)

Table 5.5: Predictions (in percentage) on the spectra of the test set with two isotopes in a 1:3 ratio. The results are averaged over all spectra belonging to the same class, regardless of the statistics (4×10^3, 4×10^4 and 4×10^5). Standard deviation is reported in brackets.

Isotopes (1:3)	**^{57}Co**	**^{60}Co**	**^{133}Ba**	**^{137}Cs**	**^{192}Ir**	**^{204}Tl**	**^{226}Ra**	**^{241}Am**
^{57}Co^{+}^{60}Co	24.8(6)	75.2(6)	0	0	0	0	0	0
^{57}Co^{+}^{133}Ba	24.9(7)	0	75.1(7)	0	0	0	0	0
^{57}Co^{+}^{137}Cs	25.9(7)	0	0	74.1(7)	0	0	0	0
^{57}Co^{+}^{192}Ir	26.0(8)	0	0	0	24.0(8)	0	0	0
^{57}Co^{+}^{204}Tl	25.1(5)	0	0	0	0	74.9(5)	0	0
^{57}Co^{+}^{226}Ra	24.5(5)	0	0	0	0	0	75.5(5)	0
^{57}Co^{+}^{241}Am	25.9(6)	0	0	0	0	0	0	74.1(6)
^{60}Co^{+}^{133}Ba	0	25.7(5)	74.3(5)	0	0	0	0	0
^{60}Co^{+}^{137}Cs	0	25.5(6)	0	74.5(6)	0	0	0	0
^{60}Co^{+}^{192}Ir	0	25.4(4)	0	0	74.6(4)	0	0	0
^{60}Co^{+}^{204}Tl	0	26.5(4)	0	0	0	73.5(4)	0	0
^{60}Co^{+}^{226}Ra	0	25.6(4)	0	0	0	0	74.4(4)	0
^{60}Co^{+}^{241}Am	0	27.1(3)	0	0	0	0	0	72.9(3)
^{133}Ba^{+}^{137}Cs	0	0	26.0(13)	74.0(13)	0	0	0	0
^{133}Ba^{+}^{192}Ir	0	0	25.2(15)	0	74.8(15)	0	0	0
^{133}Ba^{+}^{204}Tl	0	0	26.5(8)	0	0	73.5(8)	0	0
^{133}Ba^{+}^{226}Ra	0	0	25.8(9)	0	0	0	74.2(9)	0
^{133}Ba^{+}^{241}Am	0	0	29.0(11)	0	0	0	0	71.0(11)
^{137}Cs^{+}^{192}Ir	0	0	0	25.0(5)	75.0(5)	0	0	0
^{137}Cs^{+}^{204}Tl	0	0	0	26.3(4)	0	73.7(4)	0	0
^{137}Cs^{+}^{226}Ra	0	0	0	25.2(6)	0	0	74.8(6)	0
^{137}Cs^{+}^{241}Am	0	0	0	27.1(6)	0	0	0	72.9(6)
^{192}Ir^{+}^{204}Tl	0	0	0	0	25.7(5)	74.3(5)	0	0
^{192}Ir^{+}^{226}Ra	0	0	0	0	25.0(8)	0	75.0(8)	0
^{192}Ir^{+}^{241}Am	0	0	0	0	26.2(7)	0	0	73.8(7)
^{204}Tl^{+}^{226}Ra	0	0	0	0	0	25.9(7)	74.1(7)	0
^{204}Tl^{+}^{241}Am	0	0	0	0	0	22.7(8)	0	77.3(8)
^{226}Ra^{+}^{241}Am	0	0	0	0	0	0	26.7(4)	73.8(4)

5.4.2 Additional datasets

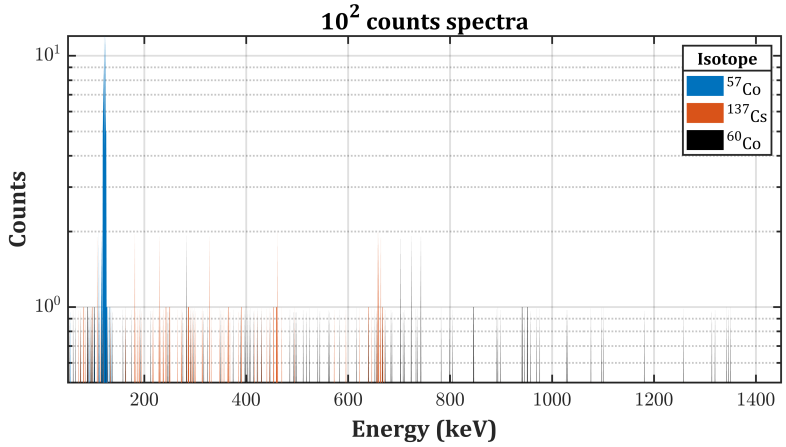

Figure 5.10: Three spectra of the 10^2 counts dataset for ^{57}Co, ^{137}Cs and ^{60}Co sources.

Firstly, I applied the algorithm on a dataset containing spectra with 10^2 counts. This is an order of magnitude less than the ones used for training and the statistical noise is dominant (Figure 5.10). Nevertheless, the network is still able to identify the correct radioisotopes, although in some cases it detects the presence of multiple sources (Table 5.6). Most of the false positives occur in the case of ^{60}Co because counts are distributed in the whole energy range: the statistics is so low that, if some events are more condensed in certain zones, the network detects the presence of another source.

Table 5.6: Confusion matrix for the dataset containing spectra with 100 counts (100 spectra for each isotope). Columns do not sum to 100 because of false multiple identification.

		ACTUAL CLASS							
PREDICTED CLASS	**Isotope**	**^{57}Co**	**^{60}Co**	**^{133}Ba**	**^{137}Cs**	**^{192}Ir**	**^{204}Tl**	**^{226}Ra**	**^{241}Am**
	^{57}Co	100	8	1	1	0	0	0	0
	^{60}Co	0	100	0	0	0	0	0	0
	^{133}Ba	0	18	100	7	1	1	0	0
	^{137}Cs	0	29	18	100	4	0	0	0
	^{192}Ir	0	17	0	0	100	0	0	0
	^{204}Tl	0	0	0	0	0	100	1	0
	^{226}Ra	0	10	0	0	0	0	100	0
	^{241}Am	1	0	2	0	1	11	0	100

Secondly, I tested the network on spectra produced by sources shielded by 5 mm of steel (^{204}Tl and ^{241}Am are not present since their γ-emissions are completely stopped by the absorber). Attenuation is one of the most problematic aspects of radioisotope identification because the spectral shape is modified (Figure 5.11). The results are less

stable because the network struggles to calculate the linear combination which best reconstructs the input spectrum (Table 5.7). Nevertheless, it is still able to identify the correct radioisotopes with few double identifications (Table 5.8).

Table 5.7: Raw output (CL. and REG.) and processed output (PROC.) of the trained net in the case of a spectrum of a ^{133}Ba source attenuated by 5 mm of steel.

	^{57}Co	^{60}Co	^{133}Ba	^{137}Cs	^{192}Ir	^{204}Tl	^{226}Ra	^{241}Am
CL.	0.039	0.012	1.000	0.438	0.225	0.000	0.000	0.014
REG.	0.032	-0.002	1.300	0.053	0.100	-0.188	0.073	-0.222
PROC.	0	0	1	0	0	0	0	0

Table 5.8: Confusion matrix for the shielded dataset (5 mm of steel) containing spectra with 10^4 counts.

		ACTUAL CLASS							
PREDICTED CLASS	**Isotope**	**^{57}Co**	**^{60}Co**	**^{133}Ba**	**^{137}Cs**	**^{192}Ir**	**^{204}Tl**	**^{226}Ra**	**^{241}Am**
	^{57}Co	100	0	0	0	0	0	0	0
	^{60}Co	0	100	0	0	0	0	0	0
	^{133}Ba	0	0	100	0	0	0	0	0
	^{137}Cs	0	0	18	100	0	0	0	0
	^{192}Ir	0	0	0	0	100	0	0	0
	^{204}Tl	0	0	0	0	0	100	0	0
	^{226}Ra	0	10	0	0	0	0	100	0
	^{241}Am	0	0	0	0	0	0	0	100

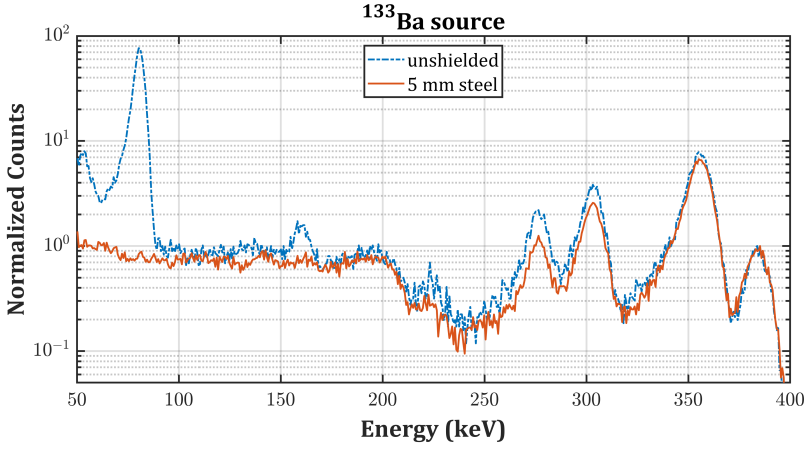

Figure 5.11: Example of the effect of shielding (5 mm of steel) for a ^{133}Ba source.

Finally, I tested the algorithm also on a dataset containing spectra with three isotopes in a 1:1:1 ratio (Table 5.9). Also in this case no classification errors are detected and the network correctly estimates the fractions.

Table 5.9: Predictions (in percentage) on the dataset containing spectra with three isotopes in a 1:1:1 ratio with 3×10^3, 3×10^4 and 3×10^5 counts. The results are averaged over all spectra belonging to the same class. Standard deviation is $\leq 1.5\%$ in all cases.

Isotopes (1:1:1)	^{57}Co	^{60}Co	^{133}Ba	^{137}Cs	^{192}Ir	^{204}Tl	^{226}Ra	^{241}Am
^{57}Co+^{60}+Co^{133}Ba	33.0	33.5	33.5	0	0	0	0	0
^{57}Co+^{60}Co+^{137}Cs	33.7	33.5	0	32.8	0	0	0	0
^{57}Co+^{60}Co+^{192}Ir	33.6	33.5	0	0	32.9	0	0	0
^{57}Co+^{60}Co+^{204}Tl	32.0	33.2	0	0	0	34.8	0	0
^{57}Co+^{60}Co+^{226}Ra	33.1	33.8	0	0	0	0	33.1	0
^{57}Co+^{60}Co+^{241}Am	32.8	33.6	0	0	0	0	0	33.6
^{57}Co+^{133}Ba+^{137}Cs	33.5	0	33.7	32.8	0	0	0	0
^{57}Co+^{133}Ba+^{192}Ir	33.9	0	33.3	0	32.7	0	0	0
^{57}Co+^{133}Ba+^{204}Tl	33.8	0	34.5	0	0	31.7	0	0
^{57}Co+^{133}Ba+^{226}Ra	33.3	0	34.2	0	0	0	32.6	0
^{57}Co+^{133}Ba+^{241}Am	33.4	0	34.6	0	0	0	0	32.0
^{57}Co+^{137}Cs+^{192}Ir	34.1	0	0	32.8	33.0	0	0	0
^{57}Co+^{137}Cs+^{204}Tl	32.4	0	0	32.6	0	35.0	0	0
^{57}Co+^{137}C+^{226}Ra	33.4	0	0	33.1	0	0	33.5	0
^{57}Co+^{137}Cs+^{241}Am	33.0	0	0	33.1	0	0	0	33.9
^{57}Co+^{192}I+^{204}Tl	32.7	0	0	0	32.2	35.1	0	0
^{57}Co+^{192}Ir+^{226}Ra	33.8	0	0	0	32.8	0	33.4	0
^{57}Co+^{192}Ir+^{241}Am	32.7	0	0	0	32.0	0	0	35.3
^{57}Co+^{204}Tl+^{226}Ra	32.1	0	0	0	0	35.8	32.0	0
^{57}Co+^{204}Tl+^{241}Am	34.3	0	0	0	0	35.9	0	29.9
^{57}Co+^{226}Ra+^{241}Am	34.3	0	0	0	0	35.9	0	29.9
^{60}Co+^{133}Ba+^{137}Cs	0	33.5	33.8	32.6	0	0	0	0
^{60}Co+^{133}Ba+^{192}Ir	0	33.9	33.1	0	33.0	0	0	0
^{60}Co+^{133}Ba+^{204}Tl	0	34.6	34.6	0	0	30.9	0	0
^{60}Co+^{133}Ba+^{226}Ra	0	33.7	33.5	0	0	0	32.8	0
^{60}Co+^{133}Ba+^{241}Am	0	34.4	34.6	0	0	0	0	31.0
^{60}Co+^{137}Cs+^{192}Ir	0	33.7	0	32.7	33.6	0	0	0
^{60}Co+^{137}Cs+^{204}Tl	0	33.0	0	32.3	0	34.8	0	0
^{60}Co+^{137}Cs+^{226}Ra	0	33.4	0	32.6	0	0	34.1	0
^{60}Co+^{137}Cs+^{241}Am	0	33.3	0	32.8	0	0	0	33.9
^{60}Co+^{192}Ir+^{204}Tl	0	33.2	0	0	32.6	34.2	0	0
^{60}Co+^{192}Ir+^{226}Ra	0	33.7	0	0	32.8	0	33.5	0
^{60}Co+^{192}Ir+^{241}Am	0	33.0	0	0	32.5	0	0	34.5
^{60}Co+^{204}Tl+^{226}Ra	0	33.4	0	0	0	34.4	32.3	0
^{60}Co+^{204}Tl+^{241}Am	0	35.4	0	0	0	35.6	0	29.0
^{60}Co+^{226}Ra+^{241}Am	0	34.2	0	0	0	0	33.7	32.1
^{133}Ba+^{137}Cs+^{192}Ir	0	0	33.5	33.2	33.3	0	0	0
^{133}Ba+^{137}Cs+^{204}Tl	0	0	34.7	34.1	0	31.1	0	0
^{133}Ba+^{137}Cs+^{226}Ra	0	0	33.6	33.1	0	0	33.3	0
^{133}Ba+^{137}Cs+^{241}Am	0	0	34.6	33.7	0	0	0	31.7
^{133}Ba+^{192}Ir+^{204}Tl	0	0	34.1	0	34.0	31.8	0	0
^{133}Ba+^{192}Ir+^{226}Ra	0	0	33.5	0	33.0	0	33.5	0
^{133}Ba+^{192}Ir+^{241}Am	0	0	33.6	0	33.2	0	0	33.2
^{133}Ba+^{204}Tl+^{226}Ra	0	0	35.0	0	0	30.9	34.2	0
^{133}Ba+^{204}Tl+^{241}Am	0	0	36.5	0	0	33.2	0	30.3
^{133}Ba+^{226}Ra+^{241}Am	0	0	34.3	0	0	0	33.0	32.8
^{137}Cs+^{192}Ir+^{204}Tl	0	0	0	32.6	32.8	34.6	0	0
^{137}Cs+^{192}Ir+^{226}Ra	0	0	0	33.0	32.9	0	34.1	0

Continued on next page

Table 5.9 – continued from previous page

Isotopes (1:1:1)	^{57}Co	^{57}Co	^{133}Ba	^{137}Cs	^{192}Ir	^{204}Tl	^{226}Ra	^{241}Am
^{137}Cs+^{192}Ir+^{241}Am	0	0	0	32.4	32.5	0	0	35.1
^{137}Cs+^{204}Tl+^{226}Ra	0	0	0	32.8	0	34.4	32.8	0
^{137}Cs+^{204}Tl+^{241}Am	0	0	0	35.2	0	35.6	0	29.2
^{137}Cs+^{226}Ra+^{241}Am	0	0	0	33.5	0	0	33.9	32.6
^{192}Ir+^{204}Tl+^{226}Ra	0	0	0	0	32.3	35.1	32.6	0
^{192}Ir+^{204}Tl+^{241}Am	0	0	0	0	35.0	36.5	0	28.5
^{192}Ir+^{226}Ra+^{241}Am	0	0	0	0	32.7	0	33.5	33.8
^{204}Tl+^{226}Ra+^{241}Am	0	0	0	0	0	35.6	34.9	29.5

5.5 Conclusions

This algorithm allows to automatically identify the radioisotopes in γ-spectra in a single step and to estimate the relative fraction of each detected radionuclides. The main strength of this approach is exploiting the identification of the isotopic fingerprints to regularise the quantification step. This allows to overcome the average energy resolution performances of CZT-based γ-detectors and produce accurate predictions on extremely noisy spectra with low statistics, where standard algorithms fail to succeed or cannot even be applied. The algorithm presents optimal performances on all classes of the test set (spectra with one or two radioisotopes at different statistics and ratios). Additionally, it shows remarkable performances on datasets with much more complex spectra not used for the training (low statistics, three radioisotopes and shielded sources). This proves the impressive generalization ability of the proposed architecture because the network makes predictions based on what it learned from the training set. This is extremely important in view of further testing on different libraries. My research group and me submitted a patent application on this algorithm.

This method combines some of the state-of-the-art techniques in data science to produce a reliable tool for the analysis of γ-spectra (densely connected blocks, all convolutional neural networks, batch normalisation and multi-objective neural network). Firstly, the algorithm exploits the capability of CNN of finding and extracting local patterns in images. This intuition represents the key of the effectiveness of the approach because the relation in the energy domain of the channels of a measured spectrum is analogous to the spatial relation among the pixels in an image. Secondly, the quantification of the relative fraction of each isotope is achieved thanks to a double-objective architecture. One branch performs the classification with which is possible to filter the results of the regression branch, occasionally unpredictable or even unphysical. Thirdly, the training of the network is reinforced by various expedients, recently proposed in the literature. The connection of each convolutional block with all subsequent ones (DC-CNN) allows a better propagation of the extracted features maps through the layers, which is usually a limitation of deep networks. Moreover, the number of learnable parameters of the proposed method is low compared to a classic ANN (multilayer perceptron). Therefore, the training is extremely fast even on a standard laptop without the need of cloud computing or graphics processing unit. After that, the only input required is the raw spectrum, without human intervention nor intermediate data processing. The method is ideal for portable or hand-held devices in which the energy consumption and the computational load must be considered. In the case of CZT-based devices, the dataset can be obtained from measurements, simulations or both. Synthetic spectra are usually preferred since the access to certain radioactive sources is limited, allowing great savings in terms of time and costs. However, in this case an accurate modelling of the response function of the whole detection system is required. CNN are sensitive to distortions to a limited extent and a certain fault tolerance between simulations and measurements is admissible. Another important consequence is that the method can be extended to any radiation detectors whose response function

can be simulated.

Regarding future works, the method will be tested on more radioisotopes with the aim of reaching libraries of 20–30 sources. The only modification required is the number of neurons in the two fully connected output layers which must match the number of isotopes (M). This will lead to a larger number of parameters, given by the product $4072 \cdot M$ where 4072 is the output of the convolutional part (see Figure 5.5). Nevertheless, this will not represent a problem since it would be compensated by an equal increase of spectra in the dataset. The fact that some radionuclides present γ-emissions at nearly the same energy is an apparent issue because the network does not only exploit the position of a certain feature but also its relation with the other ones. For example, the $\gamma_{2,0}$-ray of ^{137}Cs and the $\gamma_{17,0}$-ray of have an energy of 661.66 and 662.28 keV, respectively: the corresponding photopeaks cannot be resolved even considering the state-of-the-arts performances of CZT-based RTSD ($FWHM < 1\% \approx$ 6 keV). Nevertheless, the branching ratio is extremely different: in the case of ^{137}Cs, it is basically the only γ-emission (84.99 photons per 100 nuclear disintegrations) whereas in the case of ^{239}U the probability is lower (0.17 photons per 100 nuclear disintegrations) and, moreover, the spectrum is populated by other peaks with approximately the same intensity ($\gamma_{21,0} = 819.26$ and $\gamma_{22,0} = 844.1$ keV with 0.129 and 0.139 photons per 100 nuclear disintegrations, respectively). Since the overall spectral shape is different, the network should be able to distinguish possible superimpositions. In some applications (e.g., decommissioning) measurements are long and the contribution of the natural background, produced by a mixture of naturally occurring radioactive materials, is not negligible. This alters the spectral shape and could mislead the algorithm. However, the natural mixture is usually known and, consequently, the corresponding spectrum. Therefore, it is possible to add an additional class related to this pseudo-radionuclide with the purpose of estimating its activity (procedure already adopted by other works [92, 94]). Finally, the most challenging goal is the estimation in the case of mixture of shielded spectra. The fact that the same isotope could appear in different ways is a limit for the regression branch and the quantification is indeed problematic. A suitable training with the same radioisotopes in various configurations (different types of absorbing material and different thickness) may be an option. Alternatively, the architecture may be modified to determine if the measured spectrum is attenuated and by which material: this would be undoubtedly challenging but still a viable option.

Chapter 6

Projects and other activities

During my Ph.D. I participated in several projects with other research groups and companies which shared the common purpose of developing techniques to correct spectral distortions of CZT-based RTSD, making use of specific experimental measurements and proper models. In particular, in this chapter I will report part of the results of the synchrotron session in which I participated, which was performed in collaboration with the Department of Physics and Chemistry (DiFC) of the University of Palermo (Italy) and the Rutherford Appleton Laboratory (Didcot, UK). I will present afterwards the modelling of flux-dependent distortions which are common in industrial and medical applications, performed in collaboration with Xnext s.r.l., an Italian company specialised in industrial non-destructive inline inspections based on X-rays for quality controls.

6.1 Synchrotron session

In February 2019 I participated in a measurement session at the Diamond Light Source (DLS) located in the Harwell Science and Innovation Campus (Didcot, UK). DLS is one of the facilities of the Rutherford Appleton Laboratory (RAL) operated by the Science and Technology Facilities Council (STFC), which is one of Europe's largest multidisciplinary research organisations.

Figure 6.1: Diamond Light Source (Didcot, UK).

Synchrotron light represents the best radiation source to probe the local response of a radiation detector. B16 beamline, where the concerned experiment was carried out, is specifically dedicated to the testing and the development of new detector technologies for various applications, from metrology to astronomy. The beamline ensures large flexibility in customising the desired experimental setup and it provides both white and monochromatic X-rays in several operational modes. The main advantage of synchrotron light is indeed the possibility to adjust the irradiation conditions. In particular, B16 is characterised by the following specifications (the most relevant ones in the context of this experiment) [104]:

- Photon energy range (4–50 keV);
- beam size (down to 10×10 μm^2);
- beam position (micrometric precision);
- photon fluence (up to $\approx 2 \times 10^9$ photons$\cdot$s$^{-1}\cdot$mm^{-2}).

The aim of the experiment was to study the response of detectors with sub-millimetre pixelization and to develop techniques to correct the main distortion that affects this class of detector: charge sharing. As explained in Chapter 3, charge sharing occurs in pixelated detectors when a photon interacts under the gap between two or more pixels or, more specifically, when the charge cloud reaches a zone where the electric

field lines diverge towards different pixels. The cloud split and the charge is shared among the involved pixels. If this is the case, the process is also characterised by charge losses because electrical properties of CZT surfaces are poor in respect to the bulk and a fraction of the charge is lost because of trapping [13]. Overall, this leads to a spectral degradation performance and the presence of a high background at low energies. Another type of simultaneous collection by multiple pixels occurs when a characteristic X-ray, produced by the electron rearrangement of an atom of the detector ionised by a previous interaction, escapes from the volume below the pixel and interacts in the volume below another pixel. This effect produces escape and fluorescence peaks in those two pixels but, in this case, without charge losses (see Chapter 3 for more details). Either way, these events are in the temporal coincidence because the time required to emit and re-absorb X-rays is negligible in respect to the drift time.

In the digital acquisition approach, the output signal of the Charge Sensing Preamplifier (CSP) is digitised by a fast Analog Digital Converter (ADC). At this stage, several operations are performed on the waveform to calculate, for example, the arrival time, the height of the signal and the shape, with the aim of recognizing distorted events and intervening with appropriate corrective actions to reconstruct the true energy of the primary photon [105, 13]. Therefore, such corrections are performed on the single event, in contrast to the techniques presented in Chapter 4 which operate on the whole spectrum. However, these techniques do not conflict and are not mutually exclusive: a wise use of both can indeed provide excellent results.

6.1.1 Materials and methods

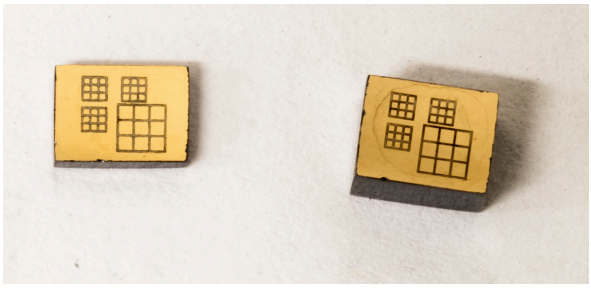

Figure 6.2: PIXIE detectors measured at the DLS synchrotron realised with CZT grown at IMEM-CNR (left) and purchased by Redlen (right).

During the experiment we measured the response of two detectors fabricated at IMEM-CNR. The former consist of a $4.25 \times 3.25 \times 1.00$ mm^3 CZT crystal grown at IMEM-CNR with the boron oxide encapsulated vertical Bridgman technique. The latter consists of a $4.25 \times 3.25 \times 3.00$ mm^3 commercial CZT crystal purchased from Redlen. Both materials presents excellent transport properties ($\mu_e\tau_e$ ranging from 1×10^{-2} to 3×10^{-2} cm^2·V^{-1} for Redlen CZT and from 0.4×10^{-3} to 1.1×10^{-2} cm^2·V^{-1} for the IMEM CZT). On both detectors, electroless gold contacts in aqueous and alcoholic solutions

were deposited on the anode and the cathode, respectively [106, 85]. Anodes consists of four matrices of 3×3 pixel with a pitch (i.e., the distance between the centres of two adjacent pixels) of 500 and 250 μm with an inter-pixel gap of 50 μm whereas cathodes are full-area (Figure 6.2). This geometry is conceived to perform testing of the detector response at different pitches. The pixels of the detectors were DC coupled to analog CSP based on a fast- and low-noise Application Specific Integrated Circuit ("PIXIE" ASIC) developed at RAL [107, 108]. The outputs of all nine pixels of the selected array were read out simultaneously and digitised (16 bit, 100 MS$\cdot$s^{-1}). Finally, the waveforms were processed online by multichannel electronics to perform Digital Pulse Processing (DPP) [109, 110]. This experiment combined the expertise of three research groups specialized in different aspects of CZT-based detectors technology: IMEM-CNR (crystal growth, fabrication), STFC (ASIC, detector characterization) and the Department of Physics and Chemistry of Palermo (DPP, detector characterization) [14, 15].

6.1.2 Experimental results

Figure 6.3 shows the spectroscopic response of one of the small arrays (250 μm pitch) of the 1 mm detectors to mono-energetic synchrotron radiation [14]. Each pixel was irradiated in the centre (on the cathode side) with a collimated X-ray beam (75×75 μm^2) at 20 and 50 keV, that is below and above the K-shell absorption energy of the CZT material, respectively (Table 6.1). The detector shows excellent performances with a $FWHM$ of 3.3% (0.66 keV) and 1.5% (0.75 keV) at 20 keV and 50 keV, respectively (Figure 6.3). At 20 keV the only distortions are the peak broadening and, in some cases, the peak asymmetry (Pixels 1, 8 and 9). The high electric field (9000 V$\cdot$cm^{-1} and the low thickness (1 mm) ensure a full collection efficiency but the presence of inhomogeneities, probably Te inclusions, partially trap the carriers. At 50 keV, the escape peaks are clearly visible in the spectra: the 26.8 keV peak is caused by the escape of the Cd $K\alpha_1$ and $K\alpha_2$ fluorescent line; the second peak (between 23.9 and 22.5 keV) is caused by the escape of the Cd $K\beta_1$ and Te $K\alpha_1$ and $K\alpha_2$ fluorescent lines; the third peak at 19 keV is caused by the escape of the Te $K\beta_1$ fluorescent line (Table 6.1). Additionally, the hole tailing effect appears and it increases the peak asymmetry. At 20 keV the radiation is mostly absorbed near the cathode and contribution of hole is negligible (small pixel effect); at 50 keV, in contrast, the interaction can occur close to the anode, although with a lower probability.

Table 6.1: Binding energies of the K-shells and X_K-ray emissions in keV of Cd and Te. The values for Zn are not reported because its contribution is negligible.

Element	$K\ 1s$	$K\alpha_1$	$K\alpha_2$	$K\beta_1$
Cd	26.71	23.17	22.98	26.10
Te	31.81	27.47	27.20	31.00

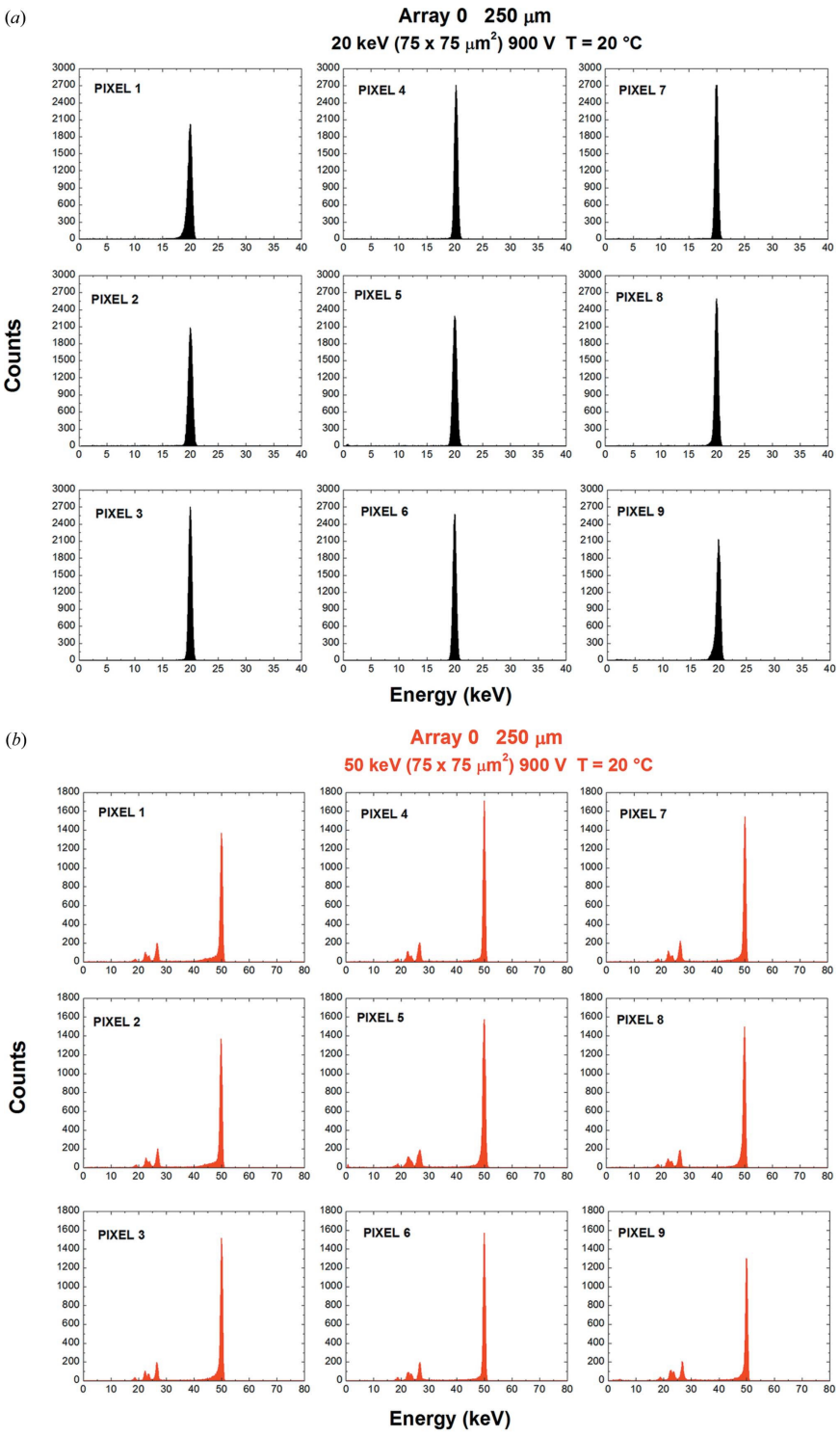

Figure 6.3: The measured energy spectra for mono-energetic synchrotron X-rays collimated at the centre of each pixel (75×75 μm^2) at 20 (a) and 50 (b) keV.

A microbeam linear scanning between the centres of two adjacent pixels of the small array was performed to better understand the effects of charge sharing on a subpixel level. We used a collimated synchrotron beam (10×10 μm) with energies of 25 keV 40 keV with position steps of 12.5 and 10 μm for the thin (1 mm) and thick (3 mm) detectors, respectively. The signals from all nine pixels were read simultaneously at each beam position to detect and record possible coincident events. The resulting spectra were analysed to extract the centroid of the main photopeak and the total number of events considering all pixels. The multiplicity parameter m defines the number of events in temporal coincidence. The results are presented in Figure 6.4 and 6.5 for the 1 mm-thick and 3 mm-thick detectors, respectively [14, 15]. The jump discontinuities at ≈ 6 keV in the centroid curves are caused by the non-zero energy threshold (4 keV).

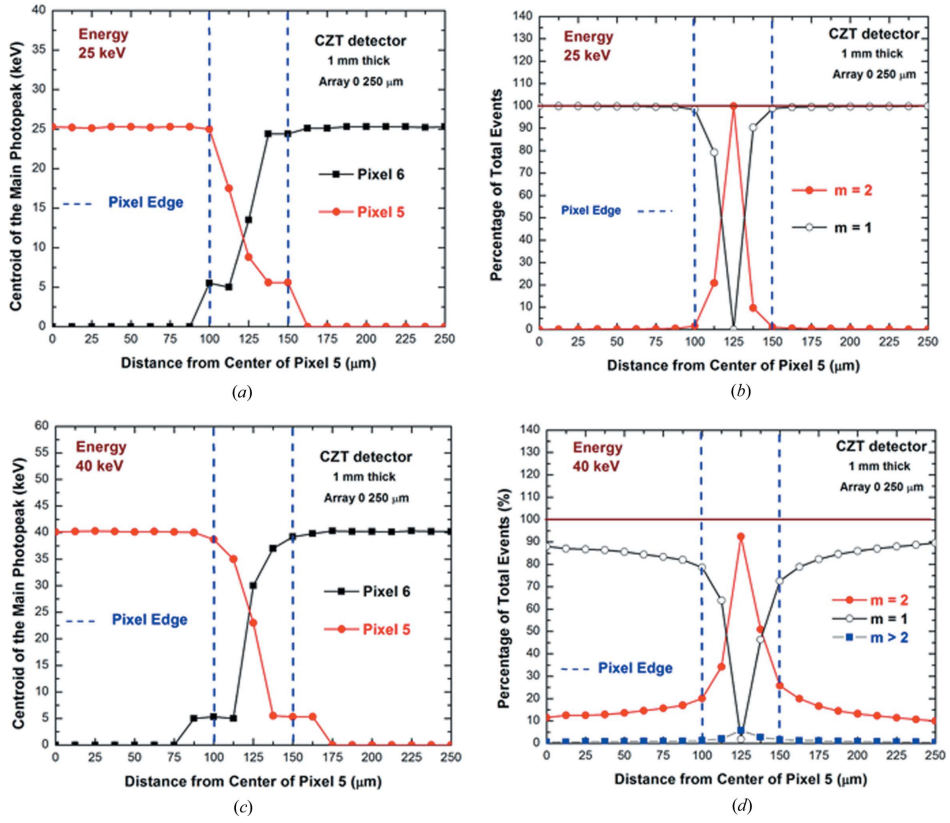

Figure 6.4: Results of the microscale line scanning (position steps of 12.5 μm) between the centres of two adjacent pixels (pixels 5 and 6) at 25 and 40 keV in the 1 mm-thick detector: photopeak centroids, (a) and (c), and multiplicity m, (b) and (d), at various beam positions.

At 25 keV, centroid variations and multiple events ($m > 1$) are observed only in the inter-pixel region of 50 mm in the 1 mm-thick detector. At the centre of the gap, 100% of events were shared. In the 3 mm-thick detector, the extent of charge sharing is visible also inside the pixel up to 50 μm within the border: this is the effect of

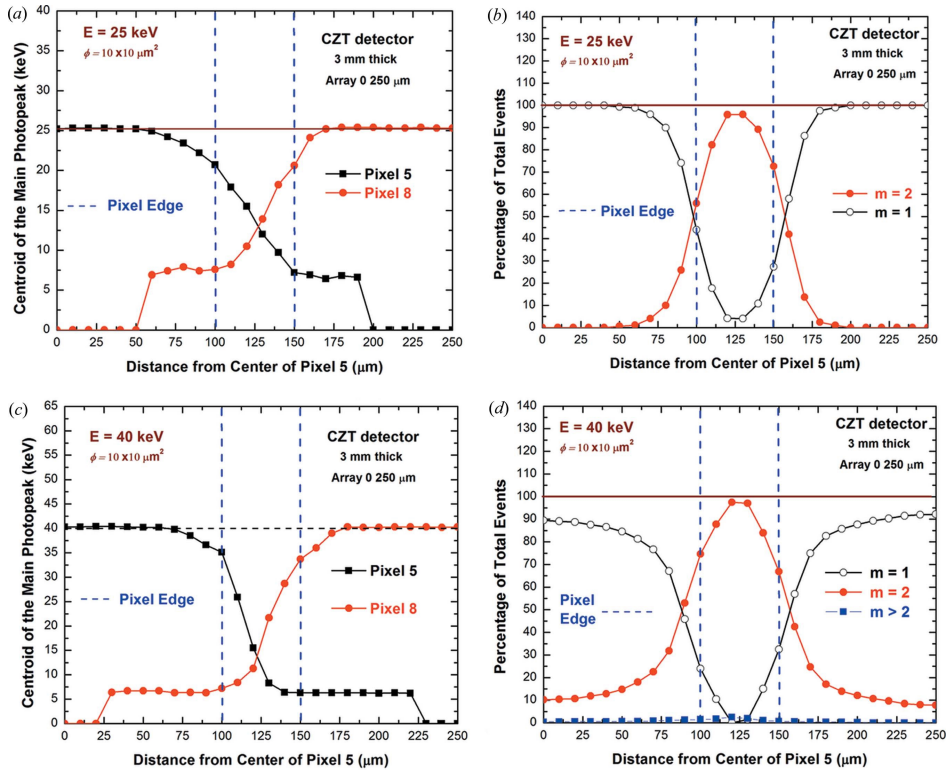

Figure 6.5: Results of the microscale line scanning (position steps of 10 μm) between the centres of two adjacent pixels (pixels 5 and 8) at 25 and 40 keV in the 3 mm-thick detector: photopeak centroids, (a) and (c), and multiplicity m, (b) and (d), at various beam positions.

the cloud broadening caused by the longer drift time. At 40 keV, coincident events were observed in a wider region in both detectors. More specifically, we can observe two contributions in multiplicity curves for $m = 2$. One is related to the effect of the cloud size, present also at 25 keV, although with wider distributions due to the larger initial dimension (see Figure 3.2 in Chapter 3). The other one is related to the absorption of fluorescent photons at a distance exceeding the pixel border. As a matter of fact, in CZT several hundreds of μm are required to completely stop the X_K-rays (see Figure 2.7 in Chapter 2). At the centre of the inter-pixel gap, 93% of the events are shared between two pixels ($m = 2$) whereas 6% are shared with an additional pixel ($m > 2$). Simply adding the energy of two coincident events, referred to as Charge Sharing Addition (CSA), do not restore the correct spectral shape due to the aforementioned charge losses (Figure 6.6b). However, a correlation between the energy after CSA and the charge sharing ratio R, which is related to the interaction position between the inter-pixel gap, can be observed (Figure 6.6a). The curvature can be fitted with the following model:

$$E_{CSA}(R) = E - E_{CSA}(0)(1 - R^2) \tag{6.1}$$

where E is the true photon energy, $E_{CSA}(0) = c_1 E + c_2$ is the measured energy after

CSA at the centre of the inter-pixel gap ($R = 0$), and c_1 and c_2 are calibrated constants. This allows to calculate the charge deficit and recover the correct energy:

$$E = \frac{E_{CSA}(R) + c_2(1 - R^2)}{1 - c_1(1 - R^2)} \tag{6.2}$$

This procedure does not depend on the energy of the photon and, thus, it can be applied for uncollimated sources [111]. Charge Sharing Correction (CSC) is valid for both the small and large array (Figure 6.6c and 6.6d) even in beam position where almost all events are affected by sharing. This is extremely important for two reasons: firstly, coincident events, which are usually rejected, can be recovered; secondly, the parameter R can be used to extract information on the interaction position within the gap and, possibly, to achieve X-ray imaging with a sub-pixel spatial resolution [112].

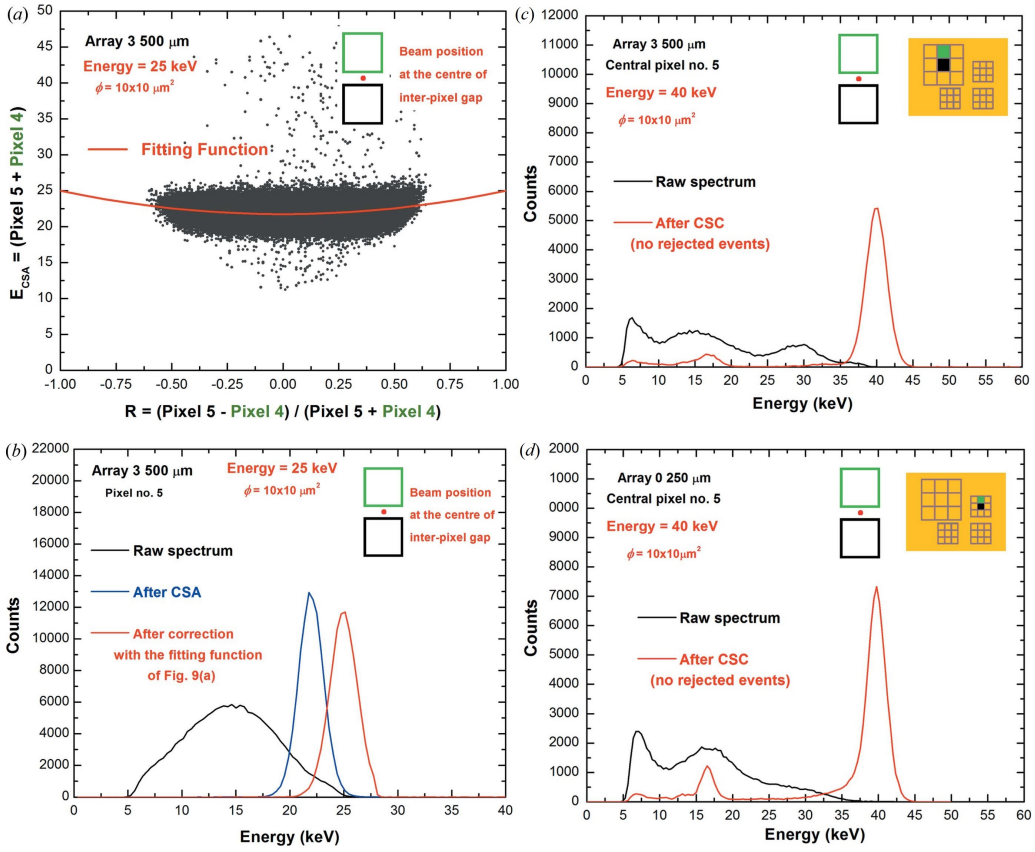

Figure 6.6: (a) 2D scatter plot of the energy after CSA of coincident events ($m = 2$) for a collimated beam position at the centre of the inter-pixel gap of the large array of the 3 mm detector plotted versus the charge sharing ratio. The red line represents the best fitting function used to correct charge losses. (b) Raw spectrum of the central pixel (black line), after CSA (blue line) and after CSC corrections (red line). (c) and (d) Raw (black lines) and corrected spectra (red lines) of the central pixel for the photon interaction at the centre of the inter-pixel gap for the large (top) and the small arrays (bottom) of the 3 mm detector.

6.2 Simulation of peak pileup distortion

The ability to predict the behaviour of the device under certain conditions indeed unlocks several possibilities and in Chapters 4 and 5 I showed two methods to exploit the knowledge of the detector response function. However, the approach describes only flux-independent distortions (Equation 4.5), which is not the case of room temperature spectroscopic X-ray inspections (e.g., medical computed tomography, industrial inline analysis). In these application fields, reducing acquisition times is increasingly demanded and high photon fluxes allow higher statistics with the same interval of time, although they inevitably introduce spectral distortions. The limits of the electronic read-out chain in terms of sampling frequency, finite pulse width and, especially, deadtime result in coincident or partially overlapped events whose pulse height does not reflect anymore the energy of the primary photon (pileup effect). Such spectral degradation impedes reliable quantitative analysis and a preliminary correction step is necessary. If DPP is employed, piled up events can be identified by specific features (e.g., anomalous rise time or pulse width) and subsequently rejected [113, 110]. This allows to preserve nice spectroscopic performances even at high fluxes, although a considerable fraction of events does not contribute to the final spectra, hence reducing the benefit of using high fluxes to decrease the acquisition time. Implementing corrections is not possible in DPP due to the intrinsic non-invertibility of the phenomenon. On the other hand, statistical approaches exploit the information contained in the whole spectrum to redistribute counts in the correct channels. Through suitable approximations, analytic models have been proposed in literature and 1^{st} order pileup distortions (i.e., two overlapped events) have already been successfully corrected [114, 115, 116, 117, 118]. Nevertheless, typical high-flux conditions (up to 10^6–10^7 photons/s/channel) are affected by higher pileup orders. A possible solution consists in predicting the response of the read-out system at given flux rate and exploiting this information to tentatively correct the spectrum. If successful, spectral unfolding can be applied to remove flux-independent distortions, following a cascade model [119] (Figure 6.7). The present work was developed in this framework in collaboration with Xnext s.r.l. (www.x-next.com).

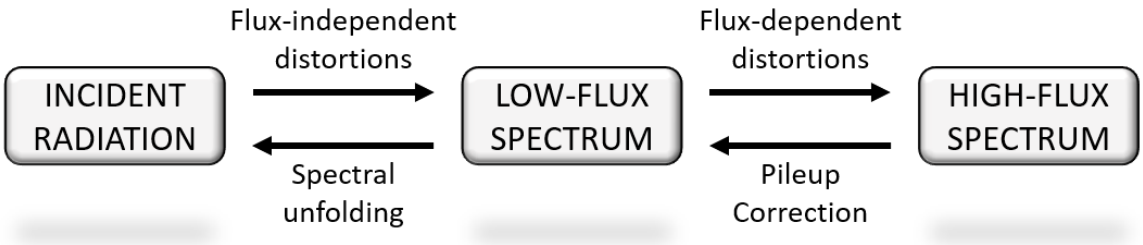

Figure 6.7: Cascade model to simulate the response function of a RTSD and to correct spectral distortions.

6.2.1 Pileup modelling

The output signal of the CSP consists of pulses with a fast rise time ($\sim$ tens of ns) and long decay time ($\sim$ tens of μs). A shaping step is mandatory to drastically reduce pulse overlapping while preserving the correct amplitude of each event [3]. The operation can be performed either analogically by a linear amplifier or digitally but the basic principles are the same. The temporal width of shaped pulses should be optimised to be as short as possible to minimize pulse overlapping but long enough to avoid ballistic deficit. The modelling of pileup starts at the first stage of the chain which does not respond linearly to the output of the block that precedes it. Assuming linearity in photo-current generation and pulse shaping, RTSD can be considered as time invariant linear systems whose response S to simultaneous events is equal to the sum of the response of the separate events [114, 120]:

$$S(As(t) + Bs(t - t')) = S(As(t)) + S(Bs(t)) \tag{6.3}$$

where s is the input signal of unitary height, A and B are amplitude constants, S is the response of the system and $t - t'$ is the temporal separation between the events. This assumption holds if the signal of each event does not exceed the dynamic range of the system and in absence of crystal polarisation which, instead, would produce time dependent response. In the case of CZT-based detectors these assumptions are usually true. At this stage, different effects arise depending on how events pile up. Let E_0 and E_1 be the heights of two consecutive pulses, t_1 the time interval between them and τ the instrumental deadtime. If $t_1 < \tau$, the two events are considered as one. Depending on the pulse shape and heights, the second event may alter the reading of the first one and the electronics reads a value ranging from E_0 and $E_0 + E_1$ (peak pileup). By increasing t_1, the two pulses return to be considered as separate events but, if the signal of the first one is not completely decayed, it alters the reading of the signal of the second one ("tail pileup"). The deadtime can be paralyzable or non-paralyzable: in the former case, each new event which arrives within the deadtime of the previous one extends the time interval in which the electronics is "dead" whereas in the latter case τ is constant. Here, I will briefly report the method I used to model the effects of pileup which is explained in detail by *Taguchi et al.* [121], although the fundamental concepts are similar to other works [45, 120, 119]. The measured spectrum with pileup $S_P(E)$ can be expressed as

$$S_P(E) = r\Delta t \cdot P(rec|r\tau) \sum_{m=0}^{\infty} P(m|rec) \cdot P(E|m) \tag{6.4}$$

where r is the incident count rate, Δt is the acquisition time, $P(rec|r\tau)$ is the probability of events being recorded, m is the pileup order, $P(m|rec)$ is the probability that the recorded events is due to a pileup event of order m and, finally, $P(E|m)$ is the probability that an event of pileup order m is measured with an energy E. The factor $r\Delta t \cdot P(rec|r\tau)$ simply represents the number of counts in the measured spectrum.

Since the time interval between events follows the Poisson distribution, $P(rec|r\tau)$ can be expressed as following:

$$P(rec|r\tau) = \begin{cases} 1/(1+r\tau) & \text{non-paralyzable} \\ \exp(-r\tau) & \text{paralyzable} \end{cases} \tag{6.5}$$

where the $r\tau$ product defines the average number of events in a time interval τ. Also $P(m|rec)$ assumes a different expression depending on the type of deadtime:

$$P(m|rec) = \begin{cases} (r\tau)^m \exp(-r\tau)/m! & \text{non-paralyzable} \\ [1-\exp(-r\tau)]^m \exp(-r\tau) & \text{paralyzable} \end{cases} \tag{6.6}$$

In the case of non-paralyzable detector, $P(m|rec)$ represents the probability that $m+1$ events occurs in a time interval τ whereas, in the other case, it is the product of the probability of having $m+1$ events separated by time intervals shorter than τ and the probability of having an additional event separated by a time interval greater than τ. It should be noted that real systems do not fall exclusively into one of these two categories, but rather they show a hybrid behaviour where one aspect prevails. Nonetheless, Equation 6.6 can be used to determine at which flux pileup effects are not negligible (Figure 6.8).

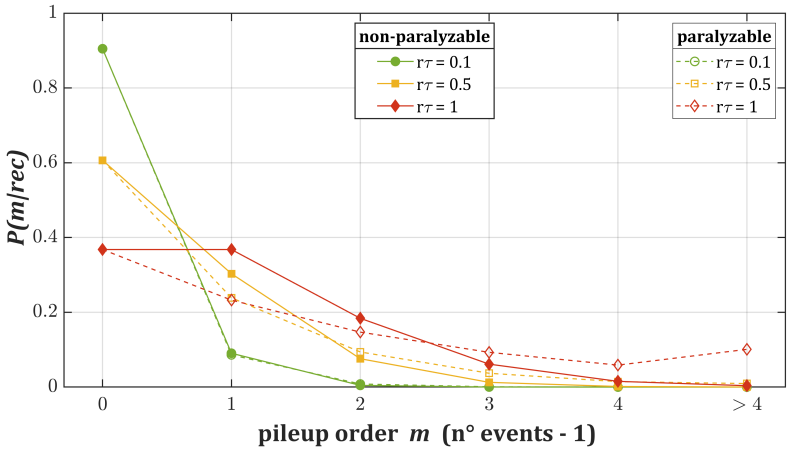

Figure 6.8: Probability of a pileup event of order m at different values of $r\tau$ for paralyzable and non-paralyzable detectors. The extendable deadtime of paralyzable detectors quickly leads to impracticable measurement conditions. A count rate of 10^6 events/s/channel and a deadtime of 0.5 μs give a $r\tau = 0.5$, to name but one example.

The last term, $P(E|m)$, describes the actual spectral shape for each pileup order. While peak pileup can be modelled straightforwardly, the effects of tail pileup cannot be derived easily. The solution proposed by *Taguchi et al.* assumes strong approximations and holds only for bipolar pulses [121]. This model cannot be applied here because, as explained later, I adopted a unipolar pulse shaping technique which generally provides

better signal-to-noise-ratio and less tail pileup but also lower performances at high fluxes. Therefore, I used only the peak pileup model and I neglected the effects of tail pileup; any discrepancies in the final results will be evaluated in the light of this approximation. A previous step is necessary to obtain $P(E|m)$ which is the calculation of the measured energy E as a function of the piled up events for each pileup order: $E^{(m)}(t_1, \ldots, t_m; E_0, E_1, \ldots, E_m)$. Basically, this consists in calculating the response of the electronics for each possible combination of pulse amplitudes and time intervals. For approximated pulse shapes (e.g., triangular, trapezoidal), $E^{(1)}$ has an analytical form but it must be derived numerically for arbitrary pulse shape and higher orders [114, 120]. For $m > 1$ this is computationally unfeasible and E^m is calculated by combining two events E_{m-1} and E_m. Another required information is the probability density function of time intervals for each pileup order:

$$P(t_1|m) = \frac{m}{\tau^m}(\tau - t_1)^m \tag{6.7}$$

Basically, $P(t_1|m)dt_1$ describes the probability to have a second event E_1 after a time between t_1 and $t_1 + dt_1$ from the first event E_0 at various m. Combining $E^{(m)}$ and $P(t_1|m)$, the pileup matrix can be calculated as

$$PU^{(m)}(E, E_{m-1}, E_1) = \int P(t_1|m)|_{E^{(m)}(t_1;E_{m-1},E_1)} dt_1 \tag{6.8}$$

For the sake of clarity, $PU^{(1)}(E, E_0, E_1)$ represents the probability that two pulses with energy E_0 and E_1, occurring within a time interval τ, are measured as a single event of energy E. Therefore, the integral considers all possible t_1 which would lead to this result. It is important to note that $PU^{(m)}$ do not depend on r and $S(E_0)$: they are characteristic of the considered electronics and can be calculated only once. Finally, the pileup spectra are calculated recursively as

$$\begin{aligned} P(E|m=1) &= \iint_{E.S.} PU^{(1)}(E, E_0, E_1) S(E_0) S(E_1) dE_0 dE_1 \\ P(E|m>1) &= \iint_{E.S.} PU^{(m)}(E, E_{m-1}, E_0) S(E_0) P(E_{m-1}|m-1) dE_0 dE_{m-1} \end{aligned} \tag{6.9}$$

where $E.S.$ is the whole energy space ($[0, \infty]$ for all variables of integration) and S is the energy distribution of the events (i.e., the spectrum at low flux). For $m > 1$ spectra are calculated by combining two pulses, the first of which is the results of all the previous pileup orders. This recursive approach allows to greatly simplify the calculations, although giving an approximated picture of the reality. Finally, the weighted sum of all $P(E|m)$ gives the pileup spectrum (Equation 6.4).

6.2.2 Measurements and simulations

The pileup model described previously was applied on measurements acquired during the synchrotron session (see the previous Section 6.1). The centre of the central pixel of the large array (500 μm pitch) of the 1 mm-thick detector was irradiated with a collimated beam at 20 keV. This allowed to avoid distortions caused both by charge sharing and fluorescence emissions and to focus the attention on flux-dependent distortions. Photon fluxes varied from 10 kcps up to $\approx$ 500 kcps. The output waveforms of the "PIXIE" ASIC were saved to files to be processed offline. Figure 6.9 shows examples of pre-amplified signals at different fluxes.

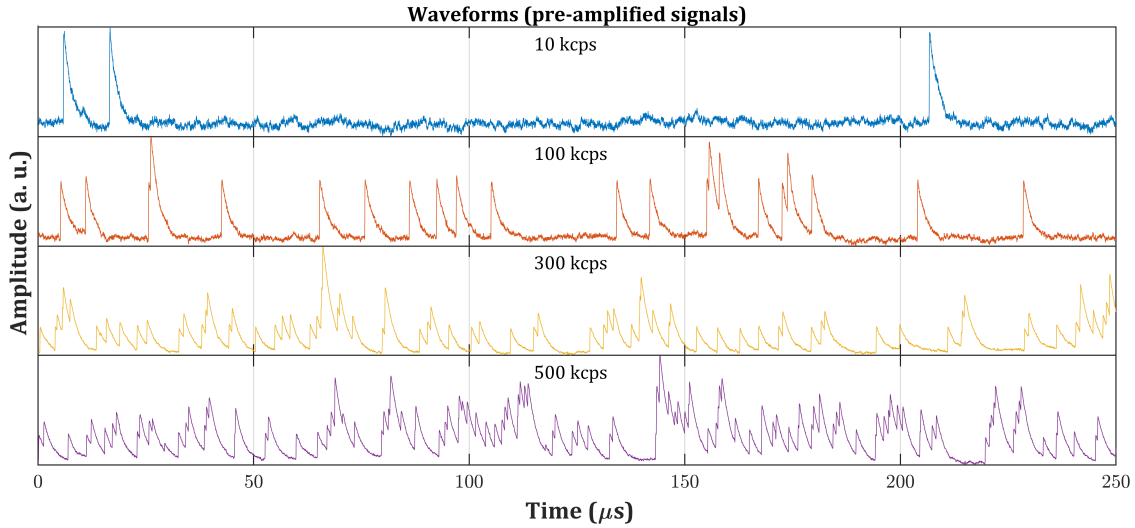

Figure 6.9: Waveforms (signals pre-amplified by the CSP) at various photon fluxes (indicated in kilocounts per second or kcps) for a collimated beam at 20 keV irradiating the centre of a pixel of the 500 μm pitch array of the 1 mm-thick PIXIE detector.

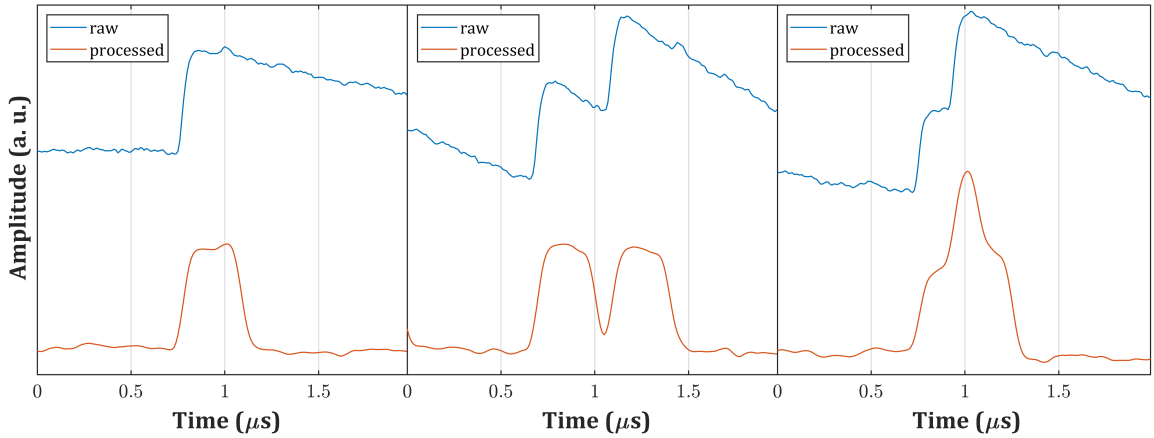

Figure 6.10: Examples of the Single Delay Line shaping with a trapezoidal filter performed on separated and partially overlapped pulses.

Pulse shaping was performed using the Single Delay Line (SDL) technique which consists in subtracting the attenuated and delayed signal to the original one [3, 122]. The attenuation is required in order to avoid undershoot and obtain a pole zero cancellation. The signal is then filtered with a trapezoidal kernel to limit the extent of noise (Figure 6.10). It is important to mention that the pulse width ($\approx$ 50 ns), given by the shaping delay and the rising and decreasing edges of the trapezoid, was not optimised for high flux conditions and it was chosen deliberately long to enhance spectral distortions caused by pileup (Figure 6.11).

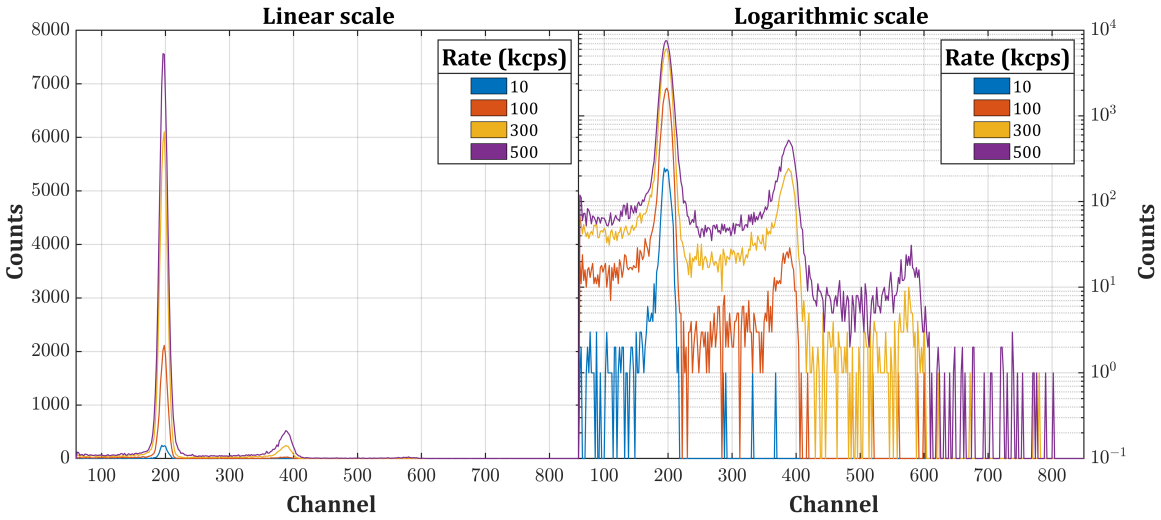

Figure 6.11: Measured spectra for mono-energetic synchrotron light at 20 keV at different photon fluxes on linear (left) and logarithmic scale (right). By increasing the count rate, various pileup orders appear (up to 3^{rd} order).

Generally, the deadtime can be obtained by measuring the number of observed counts versus the number of expected counts varying the photon flux. The resulting curve can be fitted with a proper model (Equation 6.5) and the corresponding value can be extracted. SDL processing has a paralyzable deadtime of 279 ns in the present case (Figure 6.12). However, this procedure provides an average deadtime whereas, actually, it changes depending on the amplitudes, the superimposition and the number of involved pulses [123]. As a matter of fact, in the case of SDL the deadtime for $m = 1$ should correspond to the width of shaped pulses: the electronics is able to distinguish two consecutive events if the time interval is greater than their width. Therefore, using the value extracted with Equation 6.5 in Equation 6.7 would lead to a miscalculation of the shape of $E^{(1)}(t_1; E_0, E_1)$. For this reason, unlike other works [121, 120, 119], I defined two different deadtimes, $\tau_L = 279$ ns and $\tau_P = 50$ ns, related to count losses (Equation 6.5 and 6.6) and pulse discrimination (Equation 6.7), respectively. Since higher pileup orders are obtained recursively, the same value of τ_P was used for every m.

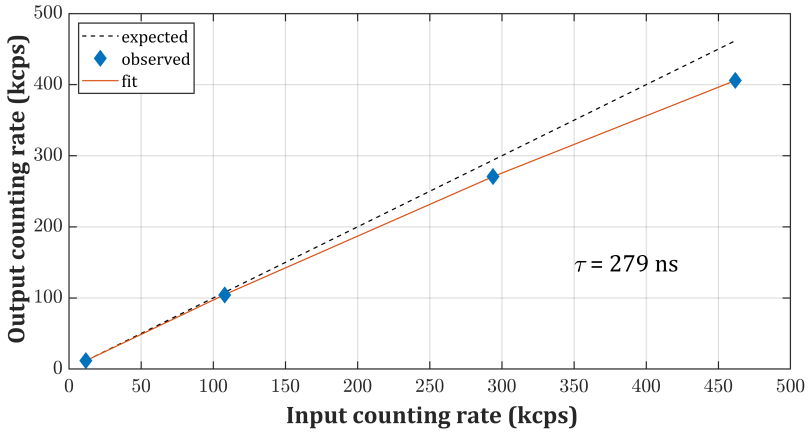

Figure 6.12: Input and output counting rate at various photon fluxes.

The ideal pulse shape with unitary height to be used in the model was obtained by averaging the signals of completely separated pulses from the measurements at 10 kcps. The simulated pileup spectra were obtained by using the low flux spectrum as $S(E_0)$ (Figure 6.13). Thanks to the use of the true pulse shape, obtained from pre-amplified waveforms at low fluxes, the overall spectral shape is well reproduced for all pileup orders. Approximated pulse shapes, although allowing analytical expressions of $E^{(m)}$, do not predict correctly the pileup spectrum [117]. Moreover, the distortions caused by tail pileup are not noticeable, as expected, and the peak pileup model is sufficient in the case of SDL shaping. However, the weights $P(m|rec)$ underestimate pileup distortions at low fluxes. The discrepancies change by varying the count rate and pileup spectra are underestimated at high fluxes. There are two possible explanations. Firstly, the recursive model (Equation 6.9) assumes that the superimposition of two pulses produces a new pulse with the same shape and an amplitude ranging from the amplitude of the former and the sum of the amplitudes of both pulses, which is then combined with another one. Since $PU^{(m)}(E, E_0, \ldots, E_m)$ can be calculated just once, it can be considered to rigorously obtain them combining the true number of pulses. Secondly, the value for τ_P should be adjusted depending on the combination of the involved pulses. That being so, the model is promising but its accuracy is not good enough to attempt some corrective approach. Analogously to spectral unfolding (Chapter 4), similar algorithms can indeed be applied if the forward step (prediction of flux-dependent distortions) is reliable.

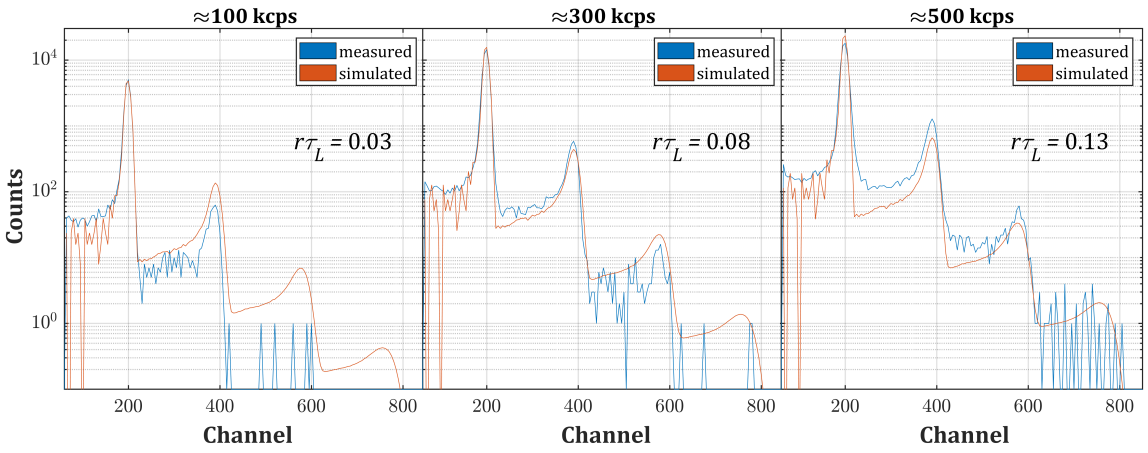

Figure 6.13: Measured and simulated spectra at various photon fluxes.

Chapter 7

Conclusions

During my Ph.D. I participated in various activities thanks to the several projects and collaborations of my research group. Being involved in each phase of the realization of a radiation detector, from crystal processing to bonding it to the dedicated electronics, and in the experimental investigation of its properties and performances was incredibly formative. It helped me in developing an overall view of the topic and the ability to correctly interpret the measurements deriving from this class of devices. This enabled the development of techniques to correct spectral distortions and to fully exploit the information contained in measured spectra.

Spectral unfolding

The quality and homogeneity of CZT crystals is still improving thanks to the progress in material technology. Despite the impressive signal-to-noise ratio achieved by state-of-the-art devices, the interaction of radiation with the semiconductor compound will always limit the full-energy absorption efficiency. The partial energy deposition, mainly caused by Compton scattering and pair production, cannot be overcome except by using absurdly large crystals, which is still unfeasible. Spectral unfolding can definitely help in taking a further step in the direction of realizing a detector devoid of instrumental artifacts, especially in the case of standard commercial devices, whose performances are poorer. In this thesis I presented a relatively simple yet effective method based on a genetic algorithm to perform this task on spectra with average energy resolution. The validation on experimental spectra obtained with different detectors is promising for future investigations.

Radioisotope identification

At this historic moment machine learning is appearing, overwhelmingly and relentlessly, in every scientific field where data analysis is still affected by high failure rates. Radioisotope identification falls into this category due to the extreme complexity and variability of certain real scenarios. Therefore, the use of machine learning-based approach is the natural consequence, as witnessed by the scientific works published on

the topic in the last few years. The large amount of experimental data required to train this class of algorithm is usually the main limitation. Their success in the last decade is due, not surprisingly, by the increasing availability of consistent datasets. In the field of γ-spectroscopy, this has not happened yet, mostly because of the dependence of the response function on the specific detection system. Nonetheless, the development of reliable simulation toolkits, which can provide an arbitrary amount of synthetic data, can enable the use of these approaches also in this field. The algorithm proposed in this thesis exploits some of the most recent data science techniques to create a reliable tool for the analysis of γ-spectra. However, the method is still at the embryonic stage. Several testing and evaluation in various conditions must be performed for the complete validation. Nevertheless, the potential is huge and there are certainly wide margins of improvement.

Measurement session at Diamond Light Source

The participation at the measurement session at DLS was a remarkable educational experience. I had the opportunity to partly fill my knowledge gap between material science and data analysis by seeing first-hand how signal acquisition and processing is performed. Digital pulse processing is a powerful tool to reject or correct distortions which would irreversibly degrade the measured spectra. As a matter of fact, predicting the *a priori* effects of charge sharing is arduous. The lack of knowledge about the transport properties in the proximity of the surfaces of CZT impedes the development of a model that takes into account different methods of crystal processing (lapping, polishing, etching, contact deposition, passivation). Therefore, intervening at the single pulse level represents the only viable option, at least for now. Similarly, the identification and rejection of overlapped signals represents the best solution to clean the spectrum from flux-dependent distortions. The models in literature allow us to predict the spectral shape varying the photon fluence to some extent. However, using such models to extract the true pulse height distribution (e.g., the spectrum at low flux) is not trivial. Great efforts are required to advance further in this direction.

List of publications

[I] S. Zanettini, F. Pattini, N. Sarzi Amadè, M. Sidoli, N. Zambelli, G. Benassi, M. Bettelli, S. Rampino, E. Gilioli, N. Protti, S. Fatemi, A. Zappettini, "Al_2O_3 Coating as Passivation Layer for CZT-based Detectors", *2018 IEEE Nuclear Science Symposium and Medical Imaging Conference Proceedings (NSS/MIC)*, Sydney, Australia, p. 1, 2018.

[II] E. Caroli, S. Zanettini, L. Abbene, N. Auricchio, G. Benassi, A. Buttacavoli, N. Sarzi Amadè, S. Del Sordo, F. Principato, N. Protti, G. Sottile, J. B. Stephen, N. Zambelli, A. Zappettini, "Development of a 3D CZT Spectrometer System with Digital Readout for Hard X/Gamma-Ray Astronomy", *2019 IEEE Nuclear Science Symposium and Medical Imaging Conference (NSS/MIC)*, Manchester, United Kingdom, p. 1, 2019.

[III] L. Abbene, F. Principato, G. Gerardi, A. Buttacavoli, D. Cascio, M. Bettelli, N. Sarzi Amadè, P. Seller, M. C. Veale, O. Fox, K. Sawhney, S. Zanettini, E. Tomarchio, A. Zappettini, "Room-temperature X-ray response of cadmium–zinc-telluride pixel detectors grown by the vertical Bridgman technique", *Journal of Synchrotron Radiation*, vol. 27, p. 319, 2020.

[IV] M. Bettelli, N. Sarzi Amadè, D. Calestani, B. Garavelli, P. Pozzi, D. Macera, L. Zanotti, C. A. Gonano, M. C. Veale, and A. Zappettini, "A first principle method to simulate the spectral response of cdznte-based x- and gamma-ray detectors," *Nuclear Instruments and Methods in Physics Research Section A: Accelerators, Spectrometers, Detectors and Associated Equipment*, vol. 960, p. 163663, 2020.

[V] M. Bettelli, N. Sarzi Amadè, S. Zanettini, L. Nasi, M. Villani, L. Abbene, F. Principato, A. Santi, M. Pavesi, A. Zappettini, "Improved electroless platinum contacts on CdZnTe X-and γ-rays detectors", *Scientific reports*, vol. 10, p. 1, 2020.

[VI] A. Buttacavoli, F. Principato, G. Gerardi, M. Bettelli, N. Sarzi Amadè, A. Zappettini, P. Seller, M. C. Veale, O. Fox, K. Sawhney, L. Abbene, "Room-temperature performance of 3 mm-thick cadmium–zinc–telluride pixel detectors with sub-millimetre pixelization", *Journal of Synchrotron Radiation*, vol. 27, p. 1180, 2020.

[VII] L. Abbene, G. Gerardi, F. Principato, A. Buttacavoli, S. Altieri, N. Protti, E. Tomarchio, S. Del Sordo, N. Auricchio, M. Bettelli, N. Sarzi Amadè, S. Zanettini, A. Zappettini, E. Caroli, "Recent advances in the development of high-resolution 3D cadmium–zinc–telluride drift strip detectors", *Journal of Synchrotron Radiation*, vol. 27, 1564, 2020.

[VIII] N. Sarzi Amadè, M. Bettelli, N. Zambelli, S. Zanettini, G. Benassi, A. Zappettini, "Gamma-ray spectral unfolding of CdZnTe-based detectors using genetic algorithm", *Sensors*, vol. 20, 7316, 2020.

[IX] N. Sarzi Amadè *et al.*, "Metodo per l'identificazione e quantificazione automatica di radioisotopi in spettri gamma", (patent pending).

Bibliography

[1] R. Evans and A. Noyau, *The Atomic Nucleus*. @Internat. S.in P. & A. Physics, McGraw-Hill, 1955.

[2] K. Siegbahn, *Beta- and Gamma-ray Spectroscopy*. North-Holland Publishing Company, 1955.

[3] G. Knoll, *Radiation Detection and Measurement*. John Wiley, 2010.

[4] A. Kahoul, A. Abassi, B. Deghfel, and M. Nekkab, "K-shell fluorescence yields for elements with $6 \leq Z \leq 99$," *Radiation Physics and Chemistry*, vol. 80, no. 3, pp. 369 – 377, 2011.

[5] S. Puri, D. Mehta, B. Chand, N. Singh, and P. N. Trehan, "L shell fluorescence yields and coster-kronig transition probabilities for the elements with $25 \leq Z \leq 96$," *X-Ray Spectrometry*, vol. 22, no. 5, pp. 358–361, 1993.

[6] C. A. Klein, "Bandgap Dependence and Related Features of Radiation Ionization Energies in Semiconductors," *Journal of Applied Physics*, vol. 39, pp. 2029–2038, mar 1968.

[7] R. C. Alig and S. Bloom, "Electron-Hole-Pair Creation Energies in Semiconductors," *Physical Review Letters*, vol. 35, pp. 1522–1525, dec 1975.

[8] M. Bettelli, N. S. Amadè, D. Calestani, B. Garavelli, P. Pozzi, D. Macera, L. Zanotti, C. A. Gonano, M. C. Veale, and A. Zappettini, "A first principle method to simulate the spectral response of cdznte-based x- and gamma-ray detectors," *Nuclear Instruments and Methods in Physics Research Section A: Accelerators, Spectrometers, Detectors and Associated Equipment*, vol. 960, p. 163663, 2020.

[9] P. Siffert, "Cadmium telluride and related materials as x-ray and gamma-ray detectors: a review of recent progress," in *Gamma-Ray Detector Physics and Applications* (E. Aprile, ed.), vol. 2305, pp. 98 – 109, International Society for Optics and Photonics, SPIE, 1994.

[10] P. J. Sellin, "Recent advances in compound semiconductor radiation detectors," *Nuclear Instruments and Methods in Physics Research Section A: Accelerators,*

Spectrometers, Detectors and Associated Equipment, vol. 513, no. 1, pp. 332 – 339, 2003. Proceedings of the 6th International Conference on Position-Sensitive Detectors.

[11] S. Del Sordo, L. Abbene, E. Caroli, A. M. Mancini, A. Zappettini, and P. Ubertini, "Progress in the development of cdte and cdznte semiconductor radiation detectors for astrophysical and medical applications," *Sensors*, vol. 9, p. 3491–3526, May 2009.

[12] G. Ottaviani, "Charge carriers transport properties in CdTe measured with time of flight technique," *Revue de Physique Appliquee*, vol. 12, no. 2, pp. 249–254, 1977.

[13] L. Abbene, F. Principato, G. Gerardi, G. Benassi, N. Zambelli, A. Zappettini, M. Bettelli, P. Seller, B. Thomas, and M. C. Veale, "Microscale x-ray mapping of czt arrays: spatial dependence of amplitude, shape and multiplicity of detector pulses," in *2017 IEEE Nuclear Science Symposium and Medical Imaging Conference (NSS/MIC)*, pp. 1–8, 2017.

[14] L. Abbene, F. Principato, G. Gerardi, A. Buttacavoli, D. Cascio, M. Bettelli, N. S. Amadè, P. Seller, M. C. Veale, O. Fox, K. Sawhney, S. Zanettini, E. Tomarchio, and A. Zappettini, "Room-temperature X-ray response of cadmium–zinc–telluride pixel detectors grown by the vertical Bridgman technique," *Journal of Synchrotron Radiation*, vol. 27, pp. 319–328, Mar 2020.

[15] A. Buttacavoli, F. Principato, G. Gerardi, M. Bettelli, N. Sarzi Amadè, A. Zappettini, P. Seller, M. C. Veale, O. Fox, K. Sawhney, and L. Abbene, "Room-temperature performance of 3 mm-thick cadmium–zinc–telluride pixel detectors with sub-millimetre pixelization," *Journal of Synchrotron Radiation*, vol. 27, pp. 1180–1189, Sep 2020.

[16] S. Ramo, "Currents induced by electron motion," *Proceedings of the IRE*, vol. 27, no. 9, pp. 584–585, 1939.

[17] W. Shockley, "Currents to conductors induced by a moving point charge," *Journal of Applied Physics*, vol. 9, no. 10, pp. 635–636, 1938.

[18] A. E. Bolotnikov, G. S. Camarda, G. A. Carini, G. W. Wright, D. S. McGregor, W. McNeil, and R. B. James, "New results from performance studies of Frisch-grid CdZnTe detectors," in *Hard X-Ray and Gamma-Ray Detector Physics VI* (A. Burger, R. B. James, and L. A. Franks, eds.), vol. 5540, pp. 33 – 45, International Society for Optics and Photonics, SPIE, 2004.

[19] A. E. Bolotnikov, N. M. Abdul-Jabbar, S. Babalola, G. S. Camarda, Y. Cui, A. Hossain, E. Jackson, H. Jackson, J. R. James, A. L. Luryi, and R. B. James, "Optimization of virtual Frisch-grid CdZnTe detector designs for imaging and

spectroscopy of gamma rays," in *Hard X-Ray and Gamma-Ray Detector Physics IX* (R. B. James, A. Burger, and L. A. Franks, eds.), vol. 6706, pp. 27 – 40, International Society for Optics and Photonics, SPIE, 2007.

[20] P. N. Luke, "Single-polarity charge sensing in ionization detectors using coplanar electrodes," *Applied Physics Letters*, vol. 65, no. 22, pp. 2884–2886, 1994.

[21] P. N. Luke, "Unipolar charge sensing with coplanar electrodes-application to semiconductor detectors," *IEEE Transactions on Nuclear Science*, vol. 42, no. 4, pp. 207–213, 1995.

[22] J. M. Ryan, J. R. Macri, M. L. McConnell, B. K. Dann, M. L. Cherry, T. G. Guzik, F. P. Doty, B. A. Apotovsky, and J. F. Butler, "Large-area submillimeter resolution CdZnTe strip detector for astronomy," in *EUV, X-Ray, and Gamma-Ray Instrumentation for Astronomy VI* (O. H. W. Siegmund and J. V. Vallerga, eds.), vol. 2518, pp. 292 – 301, International Society for Optics and Photonics, SPIE, 1995.

[23] C. M. Stahle, A. M. Parsons, L. M. Bartlett, P. Kurczynski, J. F. Krizmanic, L. M. Barbier, S. D. Barthelmy, F. B. Birsa, N. A. Gehrels, J. L. Odom, D. M. Palmer, C. Sappington, P. K. Shu, B. J. Teegarden, and J. Tueller, "CdZnTe strip detector for arcsecond imaging and spectroscopy," in *Hard X-Ray/Gamma-Ray and Neutron Optics, Sensors, and Applications* (R. B. Hoover and F. P. Doty, eds.), vol. 2859, pp. 74 – 84, International Society for Optics and Photonics, SPIE, 1996.

[24] T. Prettyman, "Theoretical framework for mapping pulse shapes in semiconductor radiation detectors," *Nuclear Instruments and Methods in Physics Research Section A: Accelerators, Spectrometers, Detectors and Associated Equipment*, vol. 428, no. 1, pp. 72 – 80, 1999.

[25] F. S. Goulding and D. A. Landis, "Ballistic deficit correction in semiconductor detector spectrometers," *IEEE Transactions on Nuclear Science*, vol. 35, no. 1, pp. 119–124, 1988.

[26] C. Kittel, *Introduction to solid state physics*. John Wiley and Sons, 2005.

[27] C. Wu, "Interfacial layer-thermionic-diffusion theory for the schottky barrier diode," *Journal of Applied Physics*, vol. 53, no. 8, pp. 5947–5950, 1982.

[28] G. Benassi, *Development of semiconductor compound materials & devices for radiation detection applications*. PhD thesis, Università degli Studi di Parma, mar 2014.

[29] S. Stolyarova, F. Edelman, A. Chack, A. Berner, P. Werner, N. Zakharov, M. Vytrykhivsky, R. Beserman, R. Weil, and Y. Nemirovsky, "Structure of

CdZnTe films on glass," *Journal of Physics D: Applied Physics*, vol. 41, p. 065402, feb 2008.

[30] A. E. Bolotnikov, G. S. Camarda, E. Chen, S. Cheng, Y. Cui, R. Gul, R. Gallagher, V. Dedic, G. De Geronimo, L. Ocampo Giraldo, J. Fried, A. Hossain, J. M. MacKenzie, P. Sellin, S. Taherion, E. Vernon, G. Yang, U. El-hanany, and R. B. James, "Cdznte position-sensitive drift detectors with thicknesses up to 5·cm," *Applied Physics Letters*, vol. 108, no. 9, p. 093504, 2016.

[31] A. Zappettini, M. Zha, M. Pavesi, and L. Zanotti, "Boron oxide fully encapsulated cdznte crystals grown by the vertical bridgman technique," *Journal of Crystal Growth*, vol. 307, no. 2, pp. 283 – 288, 2007.

[32] A. Zappettini, L. Marchini, M. Zha, G. Benassi, N. Zambelli, D. Calestani, L. Zanotti, E. Gombia, R. Mosca, M. Zanichelli, M. Pavesi, N. Auricchio, and E. Caroli, "Growth and characterization of czt crystals by the vertical bridgman method for x-ray detector applications," *IEEE Transactions on Nuclear Science*, vol. 58, no. 5, pp. 2352–2356, 2011.

[33] P. Rudolph, A. Engel, I. Schentke, and A. Grochocki, "Distribution and genesis of inclusions in cdte and (cd,zn)te single crystals grown by the bridgman method and by the travelling heater method," *Journal of Crystal Growth*, vol. 147, no. 3, pp. 297 – 304, 1995.

[34] G. A. Carini, A. E. Bolotnikov, G. S. Camarda, G. W. Wright, R. B. James, and L. Li, "Effect of te precipitates on the performance of cdznte detectors," *Applied Physics Letters*, vol. 88, no. 14, p. 143515, 2006.

[35] L. Marchini, A. Zappettini, M. Zha, N. Zambelli, A. Bolotnikov, G. Camarda, and R. B. James, "Crystal defects and charge collection in czt x-ray and gamma detectors," in *IEEE Nuclear Science Symposuim Medical Imaging Conference*, pp. 3674–3677, 2010.

[36] C. J. Sullivan, A. Burger, M. Groza, and T. H. Prettyman, "Bulk uniformity of cadmium zinc telluride (czt) crystals for large volume coplanar gamma spectrometers," in *2007 IEEE Nuclear Science Symposium Conference Record*, vol. 3, pp. 1805–1808, 2007.

[37] M. R. Squillante, J. F. Christian, and G. Entine, *Solid State Radiation Detectors*, pp. 1–18. American Cancer Society, 2016.

[38] Z. Q. Shi, C. M. Stahle, and P. Shu, "Chemical etching and post-annealing for high performance cdznte strip detectors," *MRS Proceedings*, vol. 487, p. 159, 1997.

[39] S. Park, H. Kim, J. Lee, J. Ha, and Y. Kim, "Influence of surface treatments on the performance of czt radiation detector," *Journal of the Korean Physical Society*, vol. 53, pp. 538–543, Aug. 2008.

[40] Q. Zheng, F. Dierre, V. Corregidor, J. Crocco, H. Bensalah, J. Plaza, E. Alves, and E. Dieguez, "Electroless deposition of au, pt, or ru metallic layers on cdznte," *Thin Solid Films*, vol. 525, pp. 56 – 63, 2012.

[41] S. Bell, M. Baker, D. Duarte, A. Schneider, P. Seller, P. Sellin, M. Veale, and M. Wilson, "Performance comparison of small-pixel CdZnTe radiation detectors with gold contacts formed by sputter and electroless deposition," *Journal of Instrumentation*, vol. 12, pp. P06015–P06015, jun 2017.

[42] W. Sang, J. Wei, Z. Qi, L. Wanwan, M. Jiahua, T. Jianyong, and Q. Yongbiao, "Primary study on the contact degradation mechanism of cdznte detectors," *Nuclear Instruments and Methods in Physics Research Section A: Accelerators, Spectrometers, Detectors and Associated Equipment*, vol. 527, no. 3, pp. 487 – 492, 2004.

[43] K. E. NELSON, M. MONTERIAL, and U. N. N. S. Administration, "Benchmark algorithm for radionuclide identification v1.0, version 1," 12 2019.

[44] L. Bouchet, "A comparative study of deconvolution methods for gamma-ray spectra.," *Astronomy and Astrophysics Supplement*, vol. 113, pp. 167–183, Oct. 1995.

[45] E. Roessl, H. Daerr, K. J. Engel, A. Thran, C. Schirra, and R. Proksa, "Combined effects of pulse pile-up and energy response in energy-resolved, photon-counting computed tomography," in *2011 IEEE Nuclear Science Symposium Conference Record*, pp. 2309–2313, 2011.

[46] F. G. Perey, "Least-squares dosimetry unfolding: the program stay'sl," Tech. Rep. 9374132, Oak Ridge National Lab., Tenn. (USA), 1977.

[47] J. T. Routti and J. V. Sandberg, "General purpose unfolding program louhi78 with linear and nonlinear regularizations," *Computer Physics Communications*, vol. 21, no. 1, pp. 119 – 144, 1980.

[48] R. Sanna and K. O'Brien, "Monte-carlo unfolding of neutron spectra," *Nuclear Instruments and Methods*, vol. 91, no. 4, pp. 573 – 576, 1971.

[49] K. O'Brien and R. Sanna, "Neutron spectral unfolding using the monte carlo method," *Nuclear Instruments and Methods in Physics Research*, vol. 185, no. 1, pp. 277 – 286, 1981.

[50] Y. Su, "Study of scintillation spectrometry: Unfolding methods," *Nuclear Instruments and Methods*, vol. 54, no. 1, pp. 109 – 115, 1967.

[51] M. Guttormsen, T. S. Tveter, L. Bergholt, F. Ingebretsen, and J. Rekstad, "The unfolding of continuum γ-ray spectra," *Nuclear Instruments and Methods in Physics Research A*, vol. 374, pp. 371–376, Feb. 1996.

[52] P. Bandžuch, M. Morháč, and J. Krištiak, "Study of the van cittert and gold iterative methods of deconvolution and their application in the deconvolution of experimental spectra of positron annihilation," *Nuclear Instruments and Methods in Physics Research Section A: Accelerators, Spectrometers, Detectors and Associated Equipment*, vol. 384, no. 2, pp. 506 – 515, 1997.

[53] S. Beach and L. DeWerd, "Deconvolution and reconstruction techniques of closely spaced low-energy spectra from high-purity germanium spectrometry," *Nuclear Instruments and Methods in Physics Research Section A: Accelerators, Spectrometers, Detectors and Associated Equipment*, vol. 572, no. 2, pp. 794 – 803, 2007.

[54] M. Morháč and V. Matoušek, "High-resolution boosted deconvolution of spectroscopic data," *Journal of Computational and Applied Mathematics*, vol. 235, no. 6, pp. 1629 – 1640, 2011.

[55] M. Tichy, "Bayesian approach to neutron spectrum adjustment," *Nuclear Instruments and Methods in Physics Research Section A: Accelerators, Spectrometers, Detectors and Associated Equipment*, vol. 267, no. 2, pp. 502 – 508, 1988.

[56] M. Reginatto, P. Goldhagen, and S. Neumann, "Spectrum unfolding, sensitivity analysis and propagation of uncertainties with the maximum entropy deconvolution code maxed," *Nuclear Instruments and Methods in Physics Research Section A: Accelerators, Spectrometers, Detectors and Associated Equipment*, vol. 476, no. 1, pp. 242 – 246, 2002. Int. Workshop on Neutron Field Spectrometry in Science, Technolog y and Radiation Protection.

[57] G. Medkour Ishak-Boushaki and M. Allab, "Comparison between standard unfolding and bayesian methods in bonner spheres neutron spectrometry," *Nuclear Instruments and Methods in Physics Research Section A: Accelerators, Spectrometers, Detectors and Associated Equipment*, vol. 689, pp. 35 – 39, 2012.

[58] R. Koohi-Fayegh, S. Green, N. Crout, G. Taylor, and M. Scott, "Neural network unfolding of photon and neutron spectra using an ne-213 scintillation detector," *Nuclear Instruments and Methods in Physics Research Section A: Accelerators, Spectrometers, Detectors and Associated Equipment*, vol. 329, no. 1, pp. 269 – 276, 1993.

[59] M. R. Kardan, S. Setayeshi, R. Koohi-Fayegh, and M. Ghiassi-Nejad, "Neutron spectra unfolding in Bonner spheres spectrometry using neural networks," *Radiation Protection Dosimetry*, vol. 104, pp. 27–30, 04 2003.

[60] S. Avdic, S. A. Pozzi, and V. Protopopescu, "Detector response unfolding using artificial neural networks," *Nuclear Instruments and Methods in Physics Research Section A: Accelerators, Spectrometers, Detectors and Associated Equipment*, vol. 565, no. 2, pp. 742 – 752, 2006.

[61] B. Mukherjee, "Bondi-97: A novel neutron energy spectrum unfolding tool using a genetic algorithm," *Nuclear Instruments and Methods in Physics Research Section A: Accelerators, Spectrometers, Detectors and Associated Equipment*, vol. 432, no. 2, pp. 305 – 312, 1999.

[62] V. Suman and P. Sarkar, "Neutron spectrum unfolding using genetic algorithm in a monte carlo simulation," *Nuclear Instruments and Methods in Physics Research Section A: Accelerators, Spectrometers, Detectors and Associated Equipment*, vol. 737, pp. 76 – 86, 2014.

[63] H. Israel, D. Lier, and E. Storm, "Comparison of detectors used in measurement of 10 to 300 kev x-ray spectra," *Nuclear Instruments and Methods*, vol. 91, no. 2, pp. 141 – 157, 1971.

[64] B. Grosswendt and E. Waibel, "Determination of detector efficiencies for gamma ray energies up to 12 mev ii. monte carlo calculation," *Nuclear Instruments and Methods*, vol. 131, no. 1, pp. 143 – 156, 1975.

[65] W. W. Seelentag and W. Panzer, "Stripping of x-ray bremsstrahlung spectra up to 300 kVp on a desk type computer," *Physics in Medicine and Biology*, vol. 24, pp. 767–780, jul 1979.

[66] C. S. Chen, K. Doi, C. Vyborny, H.-P. Chan, and G. Holje, "Monte carlo simulation studies of detectors used in the measurement of diagnostic x-ray spectra," *Medical Physics*, vol. 7, no. 6, pp. 627–635, 1980.

[67] E. D. Castro, R. Pani, R. Pellegrini, and C. Bacci, "The use of cadmium telluride detectors for the qualitative analysis of diagnostic x-ray spectra," *Physics in Medicine and Biology*, vol. 29, pp. 1117–1131, sep 1984.

[68] F. Olschner, J. C. Lund, and I. Stern, "Monte carlo simulation of gamma ray spectra from semiconductor detectors," *IEEE Transactions on Nuclear Science*, vol. 36, no. 1, pp. 1176–1179, 1989.

[69] M. Scannavini, P. Chirco, G. Baldazzi, G. Guidi, E. Querzola, P. Partemi, M. Rossi, M. Zanarini, F. Casali, and E. Caroli, "Computer simulation of charge trapping and ballistic deficit effects on gamma-ray spectra from cdte semiconductor detectors," *Nuclear Instruments and Methods in Physics Research Section A: Accelerators, Spectrometers, Detectors and Associated Equipment*, vol. 353, no. 1, pp. 80 – 84, 1994.

[70] T. Prettyman, "Method for mapping charge pulses in semiconductor radiation detectors," *Nuclear Instruments and Methods in Physics Research Section A: Accelerators, Spectrometers, Detectors and Associated Equipment*, vol. 422, no. 1, pp. 232 – 237, 1999.

[71] M. Jung, J. Morel, P. Fougères, M. Hage-Ali, and P. Siffert, "A new method for evaluation of transport properties in cdte and czt detectors," *Nuclear Instruments and Methods in Physics Research Section A: Accelerators, Spectrometers, Detectors and Associated Equipment*, vol. 428, no. 1, pp. 45 – 57, 1999.

[72] B. P. F. Dirks, O. Limousin, P. R. Ferrando, and R. Chipaux, "3D modeling of Cd(Zn)Te detectors for the Simbol-X space mission," in *High-Energy Detectors in Astronomy* (A. D. Holland, ed.), vol. 5501, pp. 412 – 422, International Society for Optics and Photonics, SPIE, 2004.

[73] S. Agostinelli, J. Allison, K. Amako, J. Apostolakis, H. Araujo, P. Arce, M. Asai, D. Axen, S. Banerjee, G. Barrand, F. Behner, L. Bellagamba, J. Boudreau, L. Broglia, A. Brunengo, H. Burkhardt, S. Chauvie, J. Chuma, R. Chytracek, G. Cooperman, G. Cosmo, P. Degtyarenko, A. Dell'Acqua, G. Depaola, D. Dietrich, R. Enami, A. Feliciello, C. Ferguson, H. Fesefeldt, G. Folger, F. Foppiano, A. Forti, S. Garelli, S. Giani, R. Giannitrapani, D. Gibin, J. Gómez Cadenas, I. González, G. Gracia Abril, G. Greeniaus, W. Greiner, V. Grichine, A. Grossheim, S. Guatelli, P. Gumplinger, R. Hamatsu, K. Hashimoto, H. Hasui, A. Heikkinen, A. Howard, V. Ivanchenko, A. Johnson, F. Jones, J. Kallenbach, N. Kanaya, M. Kawabata, Y. Kawabata, M. Kawaguti, S. Kelner, P. Kent, A. Kimura, T. Kodama, R. Kokoulin, M. Kossov, H. Kurashige, E. Lamanna, T. Lampén, V. Lara, V. Lefebure, F. Lei, M. Liendl, W. Lockman, F. Longo, S. Magni, M. Maire, E. Medernach, K. Minamimoto, P. Mora de Freitas, Y. Morita, K. Murakami, M. Nagamatu, R. Nartallo, P. Nieminen, T. Nishimura, K. Ohtsubo, M. Okamura, S. O'Neale, Y. Oohata, K. Paech, J. Perl, A. Pfeiffer, M. Pia, F. Ranjard, A. Rybin, S. Sadilov, E. Di Salvo, G. Santin, T. Sasaki, N. Savvas, Y. Sawada, S. Scherer, S. Sei, V. Sirotenko, D. Smith, N. Starkov, H. Stoecker, J. Sulkimo, M. Takahata, S. Tanaka, E. Tcherniaev, E. Safai Tehrani, M. Tropeano, P. Truscott, H. Uno, L. Urban, P. Urban, M. Verderi, A. Walkden, W. Wander, H. Weber, J. Wellisch, T. Wenaus, D. Williams, D. Wright, T. Yamada, H. Yoshida, and D. Zschiesche, "Geant4—a simulation toolkit," *Nuclear Instruments and Methods in Physics Research Section A: Accelerators, Spectrometers, Detectors and Associated Equipment*, vol. 506, no. 3, pp. 250 – 303, 2003.

[74] M. Moralles, D. Bonifácio, M. Bottaro, and M. Pereira, "Monte carlo and least-squares methods applied in unfolding of x-ray spectra measured with cadmium telluride detectors," *Nuclear Instruments and Methods in Physics Research Section A: Accelerators, Spectrometers, Detectors and Associated Equipment*,

vol. 580, no. 1, pp. 270 – 273, 2007. Proceedings of the 10 th International Symposium on Radiation Physics.

[75] M. Gerlach, M. Krumrey, L. Cibik, P. Müller, and G. Ulm, "Comparison of scattering experiments using synchrotron radiation with monte carlo simulations using geant4," *Nuclear Instruments and Methods in Physics Research Section A: Accelerators, Spectrometers, Detectors and Associated Equipment*, vol. 608, no. 2, pp. 339 – 343, 2009.

[76] J. Barylak, P. Podgórski, T. Mrozek, A. Barylak, M. Stęślicki, J. Sylwester, and D. Ścisłowski, "Geant4 simulations of detector response matrix for Caliste-SO," in *Photonics Applications in Astronomy, Communications, Industry, and High-Energy Physics Experiments 2014* (R. S. Romaniuk, ed.), vol. 9290, pp. 958 – 966, International Society for Optics and Photonics, SPIE, 2014.

[77] D. Wu, X. Xu, L. Zhang, and S. Wang, "A hybrid monte carlo model for the energy response functions of x-ray photon counting detectors," *Nuclear Instruments and Methods in Physics Research Section A: Accelerators, Spectrometers, Detectors and Associated Equipment*, vol. 830, pp. 397 – 406, 2016.

[78] J. Holland, P. Holland, and S. Holland, *Adaptation in Natural and Artificial Systems: An Introductory Analysis with Applications to Biology, Control, and Artificial Intelligence.* A Bradford book, M.I.T.P., 1992.

[79] D. Goldberg, G. David Edward, D. Goldberg, and V. Goldberg, *Genetic Algorithms in Search, Optimization, and Machine Learning.* Artificial Intelligence, Addison-Wesley Publishing Company, 1989.

[80] W. Langdon, *Genetic Programming and Data Structures: Genetic Programming + Data Structures = Automatic Programming!* Genetic Programming, Springer US, 2012.

[81] V. Suman and P. K. Sarkar, "Neutron spectrum unfolding using genetic algorithm in a Monte Carlo simulation," *Nuclear Inst. and Methods in Physics Research, A*, vol. 737, pp. 76–86, 2014.

[82] J. Aleotti, G. Micconi, S. Caselli, G. Benassi, N. Zambelli, D. Calestani, M. Zanichelli, M. Bettelli, and A. Zappettini, "Unmanned aerial vehicle equipped with spectroscopic cdznte detector for detection and identification of radiological and nuclear material," in *2015 IEEE Nuclear Science Symposium and Medical Imaging Conference (NSS/MIC)*, pp. 1–5, 2015.

[83] J. Aleotti, G. Micconi, S. Caselli, G. Benassi, N. Zambelli, M. Bettelli, and A. Zappettini, "Detection of nuclear sources by uav teleoperation using a visuo-haptic augmented reality interface," *Sensors*, vol. 17, p. 2234, Sep 2017.

[84] M. Bettelli, G. Benassi, L. Nasi, N. Zambelli, A. Zappettini, E. Gombia, L. Abbene, F. Principato, and D. Calestani, "Mechanically stable metal layers for ohmic and blocking contacts on cdznte detectors by electroless deposition," in *2015 IEEE Nuclear Science Symposium and Medical Imaging Conference (NSS/MIC)*, pp. 1–3, 2015.

[85] G. Benassi, L. Nasi, M. Bettelli, N. Zambelli, D. Calestani, and A. Zappettini, "Strong mechanical adhesion of gold electroless contacts on CdZnTe deposited by alcoholic solutions," *Journal of Instrumentation*, vol. 12, pp. P02018–P02018, feb 2017.

[86] M.-M. Bé, V. Chisté, C. Dulieu, M. Kellett, X. Mougeot, A. Arinc, V. Chechev, N. Kuzmenko, T. Kibédi, A. Luca, and A. Nichols, *Table of Radionuclides*, vol. 8 of *Monographie BIPM-5*. Pavillon de Breteuil, F-92310 Sèvres, France: Bureau International des Poids et Mesures, 2016.

[87] M. Lépy, J. Plagnard, and L. Ferreux, "Measurement of 241am l x-ray emission probabilities," *Applied Radiation and Isotopes*, vol. 66, no. 6, pp. 715 – 721, 2008. Proceedings of the 16th International Conference on Radionuclide Metrology and its Applications.

[88] R. Abdel-Aal and M. Al-Haddad, "Determination of radioisotopes in gamma-ray spectroscopy using abductive machine learning," *Nuclear Instruments and Methods in Physics Research Section A: Accelerators, Spectrometers, Detectors and Associated Equipment*, vol. 391, no. 2, pp. 275 – 288, 1997.

[89] L. Chen and Y.-X. Wei, "Nuclide identification algorithm based on k–l transform and neural networks," *Nuclear Instruments and Methods in Physics Research Section A: Accelerators, Spectrometers, Detectors and Associated Equipment*, vol. 598, no. 2, pp. 450 – 453, 2009.

[90] T. Burr and M. Hamada, "Radio-isotope identification algorithms for nai γ spectra," *Algorithms*, vol. 2, p. 339–360, Mar 2009.

[91] M. Monterial, K. E. Nelson, S. E. Labov, and S. Sangiorgio, "Benchmarking algorithm for radio nuclide identification (barni) literature review," technical report, Lawrence Livermore National Lab. (LLNL), Livermore, CA (United States), 2 2019. doi:10.2172/1544518.

[92] M. Kamuda, J. Stinnett, and C. J. Sullivan, "Automated isotope identification algorithm using artificial neural networks," *IEEE Transactions on Nuclear Science*, vol. 64, no. 7, pp. 1858–1864, 2017.

[93] J. He, X. Tang, P. Gong, P. Wang, L. Wen, X. Huang, Z. Han, W. Yan, and L. Gao, "Rapid radionuclide identification algorithm based on the discrete cosine

transform and bp neural network," *Annals of Nuclear Energy*, vol. 112, pp. 1 – 8, 2018.

[94] M. Kamuda and C. J. Sullivan, "An automated isotope identification and quantification algorithm for isotope mixtures in low-resolution gamma-ray spectra," *Radiation Physics and Chemistry*, vol. 155, pp. 281 – 286, 2019. IRRMA-10.

[95] D. Liang, P. Gong, X. Tang, P. Wang, L. Gao, Z. Wang, and R. Zhang, "Rapid nuclide identification algorithm based on convolutional neural network," *Annals of Nuclear Energy*, vol. 133, pp. 483 – 490, 2019.

[96] C. A. Gentile, J. Perry, S. W. Langish, K. Silber, W. M. Davis, and D. Mastrovito, "System and method for resolving gamma-ray spectra," 01 2011. US 7877340 B2, Granted Patent, United States.

[97] J. J. Ghawaly, "System and method for making nuclear radiation detection decisions and/or radionuclide identification classifications," 01 2019. US 2019/0034786 A1, Patent Application, United States.

[98] H. S. Kim, C.-s. Park, C.-i. Choi, C. H. Min, W.-g. Shin, H.-c. Lee, J. W. Kwon, H. Yu, A. R. Kim, H.-j. Choi, and H. Lee, "Method and apparatus for distinguishing radionuclide by using plastic scintillator," 05 2019. US 10281595 B2, Granted Patent, United States.

[99] G. Huang, Z. Liu, L. van der Maaten, and K. Q. Weinberger, "Densely connected convolutional networks," in *Proceedings of the IEEE Conference on Computer Vision and Pattern Recognition (CVPR)*, July 2017.

[100] S. Ioffe and C. Szegedy, "Batch normalization: Accelerating deep network training by reducing internal covariate shift," in *Proceedings of the 32nd International Conference on Machine Learning* (F. Bach and D. Blei, eds.), vol. 37 of *Proceedings of Machine Learning Research*, (Lille, France), pp. 448–456, PMLR, 07–09 Jul 2015.

[101] D.-A. Clevert, T. Unterthiner, and S. Hochreiter, "Fast and accurate deep network learning by exponential linear units (elus)." https://arxiv.org/abs/1511.07289, 2016.

[102] J. T. Springenberg, A. Dosovitskiy, T. Brox, and M. Riedmiller, "Striving for simplicity: The all convolutional net." https://arxiv.org/abs/1412.6806v1, 2015.

[103] D. P. Kingma and J. Ba, "Adam: A method for stochastic optimization." https://arxiv.org/abs/1412.6980v7, 2017.

[104] I. P. Dolbnya, K. J. S. Sawhney, S. M. Scott, A. J. Dent, G. Cibin, G. M. Preece, U. K. Pedersen, J. Kelly, and P. Murray, "A water-cooled monochromator for the

B16 Test beamline at the Diamond Light Source: capabilities and performance characterization," *Journal of Synchrotron Radiation*, vol. 26, pp. 253–262, Jan 2019.

[105] L. Abbene, G. Gerardi, and F. Principato, "Digital performance improvements of a cdte pixel detector for high flux energy-resolved x-ray imaging," *Nuclear Instruments and Methods in Physics Research Section A: Accelerators, Spectrometers, Detectors and Associated Equipment*, vol. 777, pp. 54 – 62, 2015.

[106] L. Marchini, A. Zappettini, E. Gombia, R. Mosca, M. Lanata, and M. Pavesi, "Study of surface treatment effects on the metal-cdznte interface," *IEEE Transactions on Nuclear Science*, vol. 56, no. 4, pp. 1823–1826, 2009.

[107] M. C. Veale, S. J. Bell, L. L. Jones, P. Seller, M. D. Wilson, C. Allwork, D. Kitou, P. J. Sellin, P. Veeramani, and R. C. Cernik, "An asic for the study of charge sharing effects in small pixel cdznte x-ray detectors," *IEEE Transactions on Nuclear Science*, vol. 58, no. 5, pp. 2357–2362, 2011.

[108] C. Allwork, D. Kitou, S. Chaudhuri, P. J. Sellin, P. Seller, M. C. Veale, N. Tartoni, and P. Veeramani, "X-ray beam studies of charge sharing in small pixel, spectroscopic, cdznte detectors," *IEEE Transactions on Nuclear Science*, vol. 59, no. 4, pp. 1563–1568, 2012.

[109] G. Gerardi and L. Abbene, "A digital approach for real time high-rate high-resolution radiation measurements," *Nuclear Instruments and Methods in Physics Research Section A: Accelerators, Spectrometers, Detectors and Associated Equipment*, vol. 768, pp. 46 – 54, 2014.

[110] L. Abbene and G. Gerardi, "High-rate dead-time corrections in a general purpose digital pulse processing system," *Journal of Synchrotron Radiation*, vol. 22, pp. 1190–1201, Sep 2015.

[111] L. Abbene, G. Gerardi, F. Principato, M. Bettelli, P. Seller, M. C. Veale, O. Fox, K. Sawhney, N. Zambelli, G. Benassi, and A. Zappettini, "Dual-polarity pulse processing and analysis for charge-loss correction in cadmium–zinc–telluride pixel detectors," *Journal of Synchrotron Radiation*, vol. 25, pp. 1078–1092, Jul 2018.

[112] M. Bettelli, *Development of Contacts for CZT-based X and Gamma Ray Detectors*. PhD thesis, Università degli Studi di Parma, mar 2018.

[113] L. Abbene, G. Gerardi, F. Principato, S. Del Sordo, R. Ienzi, and G. Raso, "High-rate x-ray spectroscopy in mammography with a cdte detector: A digital pulse processing approach," *Medical Physics*, vol. 37, no. 12, pp. 6147–6156, 2010.

[114] L. Wielopolski and R. P. Gardner, "Prediction of the pulse-height spectral distortion caused by the peak pile-up effect," *Nuclear Instruments and Methods*, vol. 133, no. 2, pp. 303 – 309, 1976.

[115] R. P. Gardner and L. Wielopolski, "A generalized method for correcting pulse-height spectra for the peak pile-up effect due to double sum pulses: Part i. predicting spectral distortion for arbitrary pulse shapes," *Nuclear Instruments and Methods*, vol. 140, no. 2, pp. 289 – 296, 1977.

[116] P. C. Johns and M. J. Yaffe, "Correction of pulse-height spectra for peak pileup effects using periodic and random pulse generators," *Nuclear Instruments and Methods in Physics Research Section A: Accelerators, Spectrometers, Detectors and Associated Equipment*, vol. 255, no. 3, pp. 559 – 581, 1987.

[117] D. Cano-Ott, J. Tain, A. Gadea, B. Rubio, L. Batist, M. Karny, and E. Roeckl, "Pulse pileup correction of large nai(tl) total absorption spectra using the true pulse shape," *Nuclear Instruments and Methods in Physics Research Section A: Accelerators, Spectrometers, Detectors and Associated Equipment*, vol. 430, no. 2, pp. 488 – 497, 1999.

[118] J. Plagnard, "Comparison of measured and calculated spectra emitted by the x-ray tube used at the gustave roussy radiobiological service," *X-Ray Spectrometry*, vol. 43, no. 5, pp. 298–304, 2014.

[119] J. Cammin, J. Xu, W. C. Barber, J. S. Iwanczyk, N. E. Hartsough, and K. Taguchi, "A cascaded model of spectral distortions due to spectral response effects and pulse pileup effects in a photon-counting x-ray detector for ct," *Medical Physics*, vol. 41, no. 4, p. 041905, 2014.

[120] V. Chaplin, N. Bhat, M. S. Briggs, and V. Connaughton, "Analytical modeling of pulse-pileup distortion using the true pulse shape; applications to fermi-gbm," *Nuclear Instruments and Methods in Physics Research Section A: Accelerators, Spectrometers, Detectors and Associated Equipment*, vol. 717, pp. 21 – 36, 2013.

[121] K. Taguchi, E. C. Frey, X. Wang, J. S. Iwanczyk, and W. C. Barber, "An analytical model of the effects of pulse pileup on the energy spectrum recorded by energy resolved photon counting x-ray detectors," *Medical Physics*, vol. 37, no. 8, pp. 3957–3969, 2010.

[122] L. Abbene and G. Gerardi, "Performance enhancements of compound semiconductor radiation detectors using digital pulse processing techniques," *Nuclear Instruments and Methods in Physics Research Section A: Accelerators, Spectrometers, Detectors and Associated Equipment*, vol. 654, no. 1, pp. 340 – 348, 2011.

[123] A. Brambilla, P. Ouvrier-Buffet, G. Gonon, J. Rinkel, V. Moulin, C. Boudou, and L. Verger, "Fast cdte and cdznte semiconductor detector arrays for spectroscopic x-ray imaging," *IEEE Transactions on Nuclear Science*, vol. 60, no. 1, pp. 408–415, 2013.